Rydberg Radio-Frequency Electrometry with High-Angular-Momentum States

Gianluca Allinson

Rydberg Radio-Frequency Electrometry with High-Angular-Momentum States

Gianluca Allinson

A thesis presented for the degree of

Doctor of Philosophy

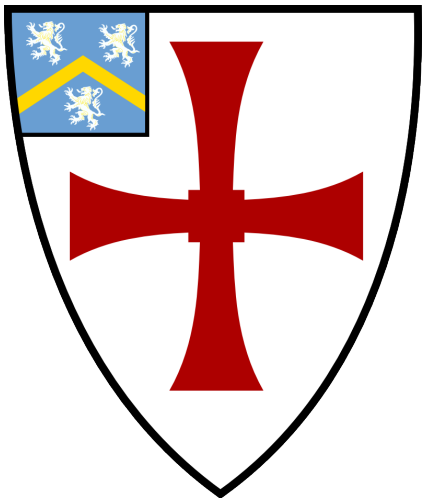

Quantum Light & Matter

The University of Durham

United Kingdom

2025

Rydberg Radio-Frequency Electrometry with High-Angular-Momentum States

Gianluca Allinson

Abstract

This thesis details a two-photon method for coupling high–orbital-angular-momentum Rydberg (highly-excited) states in a thermal caesium vapour, allowing broadband radio frequency (rf) sensing and precision spectroscopy. Using a sequence of rf driven transitions, whose energy spacings decrease significantly with increasing angular momentum, we demonstrate a Rydberg atom receiver capable of simultaneous detection of fields ranging from 128 MHz to 0.61 THz. The optical response to multiple simultaneous rf fields is reproduced theoretically, and we show experimentally that amplitude-modulated signals across these widely separated carrier frequencies can be demodulated concurrently. The same scheme enables rf and terahertz (THz) spectroscopy of states with $15 \leq n \leq 22$ and $2 \leq \ell \leq 8$. Through a global fit to measured transition frequencies, we extract a complete, independent set of quantum defects in ^{133}Cs and determine the ionic-core dipole and quadrupole polarisabilities of Cs^+, finding $\alpha_d = 15.729(18)\ a_0^3$ and $\alpha_q = 76.3(1.9)\ a_0^5$ respectively. These results allow prediction of all Cs Rydberg energy levels with uncertainties of 1 MHz or less. Finally, we analyse the fundamental and technical noise limits of EIT-based Rydberg-atom sensors, separating the contributions of photon shot noise, laser technical noise, and others. This establishes the dominant factors currently limiting sensitivity in warm-vapour Rydberg receivers and provides guidance for future direction. Together, these results further develop and demonstrate the strengths of Rydberg atoms as electric field sensors while simultaneously improving the spectroscopic data required for accurate modelling of many atomic physics experiments.

Supervisors: Professor Kevin J. Weatherill and Professor C. Stuart Adams

Acknowledgements

Foremost, I would like to thank my supervisors for their unwavering support. Kevin for his *constant* guidance and depth of knowledge, and Stuart for his genuine interest and truly unmatched enthusiasm for science.

The first year in the lab was especially defining, and I owe my thanks to Matt J. for being an early mentor in all things lasers, optics and always being up for a good laugh in Ph36. Although I worked on my own little projects (Team GHz™?), the rest of ~~Team THz™~~ *The Quantum Sensors Group* were always there to back me up. In particular, I thank Lucy, Andrew, and Shuying for their kindness and wisdom throughout my PhD. It was also a pleasure to keep the group meetings lively alongside Tepi and James, despite our widely differing work.

Outside the lab, I thank the 2021 cohort and the wider members of QLM for making the department such a unique and welcoming place, especially through FatMol, FootMol, Mol-opoly, and Friday seminars at The Vic (other pubs are encouraged...).

Special mention goes to Mark B. for introducing me to the wonderful world of CONTRACTS and DELIVERABLES and, most importantly, being a genuine pleasure to work with on the ESA project.

It has taken me 26 years to get here, and I am deeply grateful to everyone who has been part of that journey, especially the friends who fill me with laughter and the teachers who inspired me along the way. Finally, thank you to Mum, Dad, and James (and Poppy!) for your constant love and encouragement.

Above all, none of this would have been remotely possible without my wife Sarah, whose love and support I could always come home to, rain or shine, after a long day in the lab.

Contents

Declaration

The work in this thesis is based on research carried out in the group of Quantum Light and Matter at the Department of Physics, University of Durham, United Kingdom. No part of this thesis has been submitted elsewhere for any other degree or qualification, and it is the sole work of the author unless referenced to the contrary in the text.

Some of the work presented in this thesis has been published in journals and conference proceedings - the relevant publications are listed below.

Publications arising from this work

G. Allinson, L. Downes, M. J. Jamieson, A. R. Mackellar, C. S. Adams, K. J. Weatherill, "Simultaneous multi-band radio-frequency detection using high-orbital-angular-momentum states in a Rydberg-atom Receiver," Phys. Rev. Research **6**, 023317 (2024) [1].

G. Allinson, L. Downes, C. S. Adams, K. J. Weatherill, "Determination of quantum defects and core polarizability of atomic cesium via terahertz and radio-frequency spectroscopy in thermal vapor," Phys. Rev. A **111**, 062802 (2025) [2].

Other related publications

G. Allinson *et al.* 'Rydberg Receivers for Space Applications' arXiv:2601.20631

List of Figures

List of Tables

Chapter 1

Introduction

Over the past two decades, quantum technologies have expanded rapidly, driven by advances in manipulating quantum systems [3, 4]. These technologies are often grouped into four categories: quantum communication, quantum computation, quantum simulation, and quantum sensing/metrology. Broadly speaking, quantum sensing, the work that concerns this thesis, refers to the use of quantum states of matter, such as superposition, entanglement, or long-lived coherence, to measure physical quantities with precision or capabilities beyond those of traditional sensors [5, 6]. Here we use traditional to mean sensors that do not deliberately exploit quantum coherence or entanglement, even though they may still be grounded in quantum physics (as is the case for semiconductors, lasers, or even atomic clocks). The term quantum sensing is therefore used somewhat variably: in a stricter sense it is reserved for sensors enhanced by non-classical correlations (e.g. entanglement), while in a broader sense it encompasses devices that rely on the manipulation of quantum objects, such as discrete energy levels. In this thesis we adopt the latter convention, placing Rydberg-atom sensors, those explored in this thesis, alongside

other quantum devices that exploit coherence and other properties of atomic states rather than strictly entanglement.

Among the many possible platforms, atom-based quantum sensors are particularly notable. Atoms provide intrinsically identical, stable, and reproducible references defined by fundamental constants, which enable absolute measurements without need for some external calibration. Atom interferometers have been demonstrated for gravimetry [7, 8] and inertial navigation [9], optical lattice clocks [10] which achieve incredible precision [11, 12] for use in position, navigation and timing [13], and atomic magnetometers [14] are used in fields ranging from biomedicine [15] to geophysics [16]. These examples illustrate how atoms themselves can serve as precise and universal probes of external fields, and provide the foundation for more specialised approaches such as Rydberg-atom electrometry, which will be the focus of this thesis.

1.1 Rydberg Atom Sensors

Rydberg atoms, in which one or more valence electrons are highly excited, exhibit exaggerated properties that scale strongly with principal quantum number, n [17]. Intuitively, this arises from the large spatial extent of the Rydberg electron's wavefunction, approaching the micron scale compared to sub-nanometre scale when the electron is in the ground-state. This leads to strong interactions with light, static electric fields, and long-range interactions between other atoms. These properties have made Rydberg atoms valuable tools across quantum technologies, from quantum information processing and quantum simulation, where strong, controllable interactions enable quantum entanglement and quantum gates, to precision spectroscopy and sensing [18, 19].

In this thesis, we focus on their sensitivity to electromagnetic radiation — light! Because Rydberg transitions couple strongly to radiofrequency (rf) and microwave fields, they can be used as atomic probes of electromagnetic radiation, providing

a fundamentally different way of sensing compared to traditional antennas and electronic receivers.

Historically, Rydberg atoms have been explored intermittently as probes of ac and dc electric fields through many different methods [20, 21, 22, 23, 24, 25]. However, it was not until the demonstration of a non-destructive measurement by an optical readout using electromagnetically induced transparency (EIT) [26] that their potential as practical sensors could be fully realised. This development enabled advances in Rydberg-based electric-field detection [27, 28], culminating in the first demonstrations of microwave electrometry using these methods [29]. Concurrent work established that Rydberg-atom receivers can be directly tied to fundamental constants, providing a route toward SI-traceable standards for radio-frequency (rf) electric-field strength and power [30, 31]. At the core of all Rydberg microwave electrometry, whether for sensing, spectroscopy etc., is a single relationship that links what we detect optically to the rf electric field we want to measure. This entire thesis can be viewed as different manifestations of the same underlying quantity, the Rabi frequency:

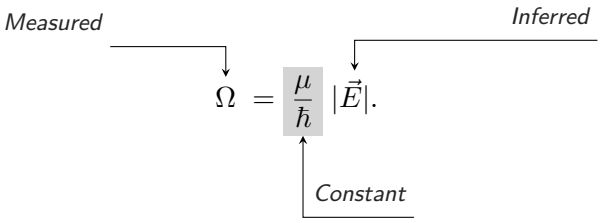

(1.1)

Here, Ω is the Rabi frequency which governs the interaction between two atomic states, μ is the transition dipole moment (a measure of intrinsic transition strength) for that specific transition, and $|\vec{E}|$ is the amplitude of the applied electric field. In Rydberg-atom experiments, we measure Ω indirectly through an optical power measurement ('Measured'). Because μ and $\hbar$ are fixed constants ('Constant'), the measured value of Ω can be used to determine the external electric field ('Inferred'). This simple equation appears in many aspects of Rydberg electrometry. Every technique developed in this thesis can be understood as different ways of measuring or manipulating this fundamental interaction strength.

The work presented in this thesis explores several open challenges associated with Rydberg atom sensors based on EIT in a caesium atomic vapour. Specifically, we address three themes: (i) the use of Rydberg-EIT as a route to broadband and lower-frequency receivers, a capability often emphasised in the literature [32] but not yet fully explored; (ii) improving the accuracy of caesium atomic data available in open-source databases such as `arc` [33], broadly relevant for quantum technologies, including Rydberg atom-based sensors; and (iii) understanding the theoretical sensitivity limits of Rydberg-EIT sensors in describing the role of different noise sources.

1.2 Thesis Structure

In this chapter we have provided the scientific context for the work and an introduction to Rydberg-atom rf electrometry. Chapter 2 develops the theoretical tools used throughout the thesis, including models of atom–light interactions and atomic structure that underpin the experimental and computational methods. Chapter 3 describes the experimental approaches, including optical layouts, beam geometries, instrumentation, a home-built laser system, and data acquisition methods, which form the background of the results presented in later chapters.

In Chapter 4, we introduce and explore multi-level ladder schemes in EIT, where multiple Rydberg states are coupled onto a single optical probe. These schemes are investigated both as a method for rf and microwave sensing and as a route toward broadband Rydberg receivers. Chapter 5 applies these methods to precise spectroscopy of caesium Rydberg levels, yielding a new, complete and independent set of quantum defects to refine atomic data resources such as `arc` [33]. Chapter 6 extends this work to high-angular-momentum Rydberg states, providing the first measurement of the true ionic core (Cs^+) polarisabilities. Finally, Chapter 7 presents a systematic study of noise in Rydberg rf sensors, identifying the dominant processes that set the ultimate sensitivity limits of the techniques demonstrated in this thesis.

Chapter 2

Atom-Light Theory

2.1 Quantum Description of Alkali Metal Atoms

Rydberg atoms are most naturally described using the single-electron quantum mechanics of hydrogen-like systems. Alkali metals, including caesium, possess a single valence electron outside a closed-shell ionic core, and at the large orbital radii associated with Rydberg excitation the electron experiences an almost pure Coulomb potential [17]. This makes the hydrogenic model an excellent starting point for understanding their structure and interactions. The purpose of this section is not to re-derive the full formalism of quantum mechanics, but to summarise the notation and physical processes required later to better understand the content used in this thesis.

The stationary states of the valence electron is described by the time-independent Schrödinger equation [34]

$$\hat{H}|\psi\rangle = E|\psi\rangle, \tag{2.1}$$

through its energy, E, with a Hamiltonian

$$\hat{H} = -\frac{\hbar^2}{2m_r}\nabla^2 - \frac{Ze^2}{4\pi\epsilon_0 r}, \tag{2.2}$$

where $\hbar$ is the reduced Planck constant, ∇ the Laplacian operator, Z the nuclear charge, e the elementary charge, ϵ_0 the vacuum permittivity*, and r the electron–core separation. The latter term is the potential energy of the system as described by the Coulomb potential, the potential energy of the electron with charge, $-e$, arising from a nucleus of charge Z.

Because the potential is spherically symmetric, the solutions, named wavefunctions $\psi(\mathbf{r})$, separate in spherical coordinates into radial and angular components [35],

$$\psi(\mathbf{r}) = R_{n\ell}(r)Y_{\ell,m}(\theta,\phi), \tag{2.3}$$

labelled by the principal, orbital, and magnetic quantum numbers (n, ℓ, m). The $Y_{\ell,m}$ encode the orbital angular momentum of the electron through the quantum numbers, ℓ (magnitude) and m (projection along the chosen axis), while the radial part, $R_{n\ell}(r)$, depends on the principal quantum number, n, and determines the electron probability amplitude as a function of distance from the nucleus giving both the size of the electronic orbit and the energy of the state.

Historically, the the discrete nature of the energies occupied by the electron was first observed empirically through absorption and emission lines in atomic spectra [36, 37, 38]. For a purely Coulombic potential, the bound-state energies depend only on the principal quantum number n and are given by [39]

$$E_n = -\frac{hcR_\infty}{n^2}, \tag{2.4}$$

so states with different orbital angular momentum ℓ are degenerate meaning they share the same energy despite being distinct physical states. In real atoms such as caesium, however, the potential deviates from the ideal Coulomb form due to a number of effects which we explore later. These effects break the ℓ-degeneracy

*$c = 1/\sqrt{\epsilon_0\mu_0}$, where c is the speed of in vacuum and μ_0 the vacuum magnetic permeability.

and produce a characteristic large energy shift for low-ℓ states. For high-ℓ Rydberg states the electron spends most of its time far from the core and the potential becomes increasingly hydrogenic, restoring an approximate degeneracy [17].

Several key scaling relations that we use throughout this thesis arise directly from this nearly hydrogenic structure [18]:

$$\langle r \rangle \propto n^2, \quad \Delta E \propto n^{-3} \quad \text{and} \quad |\mu| \propto n^2 \tag{2.5}$$

where $\langle r \rangle$ is the expectation value of the radial wavefunction, ΔE denotes the energy spacings between states of adjacent n and $|\mu|$ here specifically denotes the dipole moment between adjacent states. These scalings capture the behaviour of strong electric-dipole coupling of Rydberg atoms to rf and terahertz fields, their energy separations and underlie the sensitivity of Rydberg-EIT electrometry.

2.2 Atomic Structure of Caesium

The hydrogenic model outlined in the previous section provides the leading description of highly excited Rydberg states. Real alkali atoms, however, exhibit several important deviations from a pure Coulomb potential, especially at short range due to the differing ionic core. These deviations lift the large degeneracies of the hydrogen spectrum and give rise to the fine structure, hyperfine structure, and quantum defects that define the detailed level structure of caesium. This section summarises the elements of atomic structure required to understand the energies of caesium, Rydberg transitions between their states, and the spectroscopic measurements presented in later chapters.

2.2.1 Fine-Structure

The electron possesses intrinsic spin $s = 1/2$, which couples to its orbital motion through the spin–orbit interaction [39]. This coupling produces states of total electronic angular momentum

$$\mathbf{J} = \mathbf{L} + \mathbf{S}, \quad J = \ell \pm \frac{1}{2} \tag{2.6}$$

and lifts the degeneracy between the resulting j-manifolds. The splitting is small compared with the separation between different n-manifolds, but sufficiently large to be spectroscopically resolved in the Rydberg states used throughout this work.

The resulting states are labelled by the standard spectroscopic notation $n\ell_j$ (e.g. $50p_{3/2}, 17i_{15/2}$). The orbital quantum number ℓ is denoted by spectroscopic letters $s, p, d, f, g, \ldots = 0, 1, 2, 3, 4, \ldots$. This labelling is used throughout the thesis when identifying the optical and rf-driven transitions*.

Accounting for relativistic effects leads to an additional energy shift which is only dependent on ℓ. This arises from when the electron experiences relativistic velocities close to the nucleus. The form of this energy shift is given in a later chapter in the context of measurements of energy levels. A second additional shift arises again from a relativistic effect leading to the term, which only affects states with $\ell = 0$ [39].

Later, we address transitions between the many different ℓ_j states using external fields for electrometry and sensing applications.

2.2.2 Hyperfine Structure

Beyond fine structure, even smaller energy splittings arise from the interaction of the electron with the nuclear spin, known as the *hyperfine structure*. Just as the electron possesses an intrinsic spin $s = 1/2$, the nucleus is characterised by a nuclear spin, I. Caesium has a relatively large nuclear spin, $\mathbf{I} = 7/2$, leading to a magnetic-dipole hyperfine interaction that splits each fine-structure level into states of total angular momentum [39]

$$\mathbf{F} = \mathbf{I} + \mathbf{J}. \tag{2.7}$$

*The letters then follow alphabetically from g for higher ℓ states, but omitting j for $\ell = 7$.

In this thesis, hyperfine structure plays only a supporting role. It is observable and important at low principal quantum numbers, where we use it address specific hyperfine states to stabilise our lasers, but becomes vanishingly small for the highly excited Rydberg states that form the focus of this work. For these states, the splitting is far below our experimental resolution and is therefore omitted unless explicitly stated.

2.2.3 Alkali Metal Atoms

In modern atomic physics, alkali metals such as rubidium and caesium are widely employed due to the relative simplicity of their electronic structure, their high vapour pressure at room temperature and the availability of lasers at relevant wavelengths. Their single valence electron outside a closed shell makes them amenable to the single-electron treatment introduced in Section 2.1. However, unlike the idealised hydrogen atom, the Coulomb potential experienced by the valence electron is modified by the presence of other 'core' electrons. The finite extent and screening of the nuclear charge by the core electrons introduce an additional phase shift relative to the hydrogenic radial wavefunction, which is parametrised by the quantum defect, $\delta_{\ell,j}$ [17]. This leads to deviations from the exact hydrogenic wavefunctions and energy levels.

The bound-state energies, being assigned quantum numbers $n\ell j$, in an alkali atom can be expressed as

$$E_{n\ell j} = -hc\,\frac{R_\infty}{\left(n-\delta_{\ell j}(n)\right)^2}, \tag{2.8}$$

where R_∞ is the Rydberg constant and $\delta_{\ell,j}(n)$ is (usually) an empirically determined parameter characteristic of each ℓ, j series [34]. The size of the quantum defect depends strongly on orbital angular momentum. Low-ℓ states (s, p and d) have significant probability density within the core region, where inner-shell electrons partially shield the nuclear charge therefore acquiring large quantum defects [17] depressing their energies. In contrast, high-ℓ states (f, g...) are almost purely

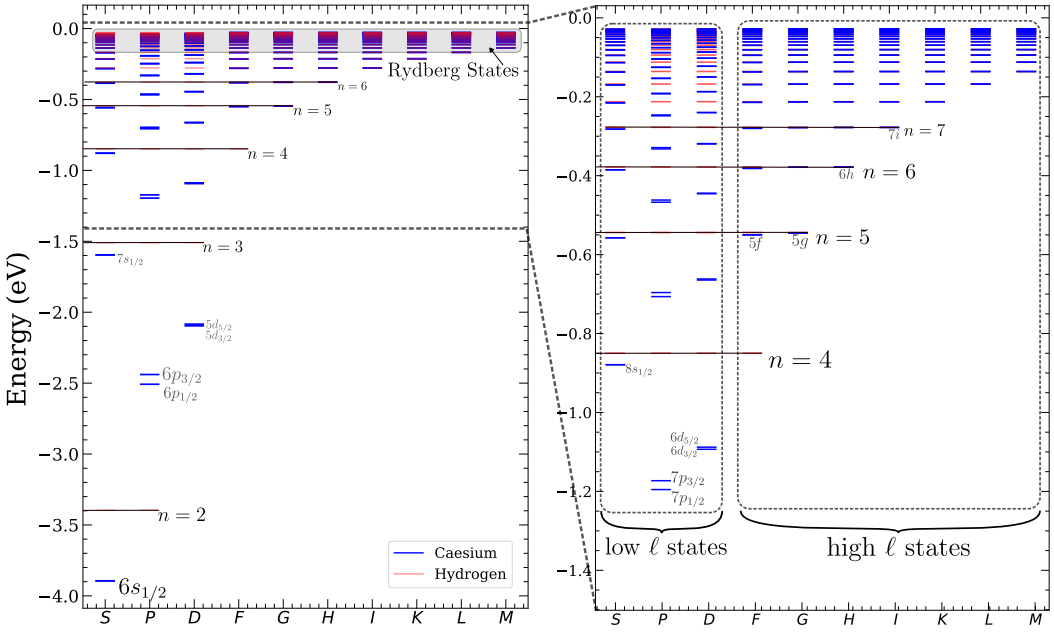

Figure 2.1: An energy level diagram showing the difference in the caesium spectrum and the spectrum of the hydrogen atom. *Left:* An overview of the energy scales between caesium and the hydrogen atom showing the degenerate states of hydrogen (red) in comparison to the highly ℓ dependent states of caesium (blue). Each hydrogen n manifold is labelled along with some low lying states of caesium. *Right:* A zoom of the higher n states of both spectrums showing the convergence of the caesium spectrum at the high angular momentum states ($\ell \geq 3$)*. At low ℓ states the quantum defects are large and show little resemblance to the hydrogen atom spectrum, e.g. the $7p$ states are almost 1 eV depressed in energy from the $n = 7$ hydrogen manifold.

hydrogenic, with $\delta_{\ell,j} \approx 0$. Their energies follow the hydrogenic formula to good approximation. The difference between the energy spectrum of a hydrogen atom and a caesium atom is highlighted in Fig. 2.1.

This dependence on ℓ plays a central role in the experimental work presented later in this thesis. Low-ℓ Rydberg states serve as the optically accessible levels in the EIT scheme and are measured with high precision to refine the corresponding quantum defects. In contrast, the dense and nearly hydrogenic manifold of high-ℓ states provides a ladder of closely spaced rf transitions that enables broadband sensing (Chapter 4) and allows us to determine specific quantum defects and related atomic constants (Chapters 5 and 6). For these high-ℓ states, the dominant deviation from

*Note that $\ell <$ n.

ideal hydrogenic behaviour arises from the polarisabilities of the Cs^+ core, which introduces a small additional energy shift that scales approximately as $1/n^3\ell^5$ [40]. The energy spacings between states of adjacent ℓ become directly measurable in our spectroscopy. We exploit this in Chapter 6 to extract both dipole and quadrupole polarisabilities of Cs^+.

2.2.4 Effective Potentials for Alkali Rydberg States

In modern approaches, the wavefunction of the valence electron in alkali-metal atoms is treated by writing a more complete description of the total potential. Namely, these include polarisation of the ionic core due to the electron, a modified central potential representing the screened nuclear charge and a spin orbit interaction representing some potential

$$V(r) = V_{\text{eff}} + V_{\text{SO}}, \tag{2.9}$$

to replace the potential in equation 2.2. A widely used form that includes these effects is from [41] with, in atomic units*,

$$V_{\text{eff}}(r) = \frac{1}{r}\left(1 + (Z-1)e^{-ra_{1,\ell}} - r(a_{3,\ell} + ra_{4,\ell})e^{-ra_{2,\ell}}\right) - \frac{\alpha_d}{2r^4}(1 - e^{-(\frac{r}{r_c})^6}) \tag{2.10}$$

where α_d (often denoted α_c for the ionic *core* polarisability) is the static dipole polarsability of the ionic core, Cs^+. The various constants, r_c, the cut-off radius defining where to truncate the polarisation potential near the origin, and $a_{m,\ell}$ are fit parameters listed in [41] for different ℓ and alkali-metal species. The spin orbit potential takes the form

$$V_{\text{SO}} = \frac{\mathbf{L}\cdot\mathbf{S}}{2m_r c^2}\frac{1}{r}\frac{\mathrm{d}V_{\text{eff}}(r)}{\mathrm{d}r}\left(1 - \frac{V_{\text{eff}}(r)}{2m_r^2 c^2}\right)^{-2} \tag{2.11}$$

where the latter factor ensures that the wavefunction is well defined near the origin as $r \to 0$ [42].

*where the constants $\hbar$, m_e, $4\pi\epsilon_0$, and e all correspond to the value 1.

Radial wavefunctions for alkali Rydberg states can be obtained by numerically integrating the radial Schrödinger equation in the presence of the effective single-electron potential, for example using the Numerov method. This approach is implemented in widely used open-source packages such as `arc` [33], which is employed throughout this thesis to compute accurate dipole matrix elements and transition strengths. Presenting the full effective potential here is also intended to emphasise the central role of the Cs^+ dipole polarisability, α_d, which governs the dominant deviation from hydrogenic behaviour for high-ℓ states and directly determines many of the measurable quantities in this work. The influence of the ionic core is interestingly also evident in the fine structure itself: in caesium, exchange effects modify the spin–orbit interaction to such an extent that the usual hydrogenic ordering of the $f_{5/2}$ and $f_{7/2}$ levels is inverted [43].

2.3 Atom-Light Interaction

Having established the structure and energy-level organisation of alkali atoms, we now consider how these states couple to electromagnetic radiation. Understanding this interaction is essential for the spectroscopic and sensing techniques employed throughout this thesis. We follow the a semi-classical approach in which the atom is treated quantum mechanically and the electromagnetic field classically, an approximation that is well suited to our thermal vapour experiments [44, 34].

2.3.1 Electric Dipole Transitions

The interaction of a bound electron with an applied field follows from the minimal-coupling Hamiltonian, the dynamics of a single electron in an external field are written as [44]

$$\hat{H} = \frac{1}{2m_r}\big(-i\hbar\boldsymbol{\nabla} + e\mathbf{A}\big)^2 + V(r), \tag{2.12}$$

where $\mathbf{A}$ is the vector potential of the applied electromagnetic field, defined via $\mathbf{E} = -\partial\mathbf{A}/\partial t - \nabla\phi$. Expanding this and simplifying, the atom–field coupling

reduces to the electric–dipole interaction [44],

$$\hat{H}_{\text{int}} = -\boldsymbol{\mu} \cdot \mathbf{E}(t), \tag{2.13}$$

where $\boldsymbol{\mu} = -e\mathbf{r}$ is the electric dipole operator. Two features justify this derivation. First, the optical field varies negligibly over the extent of the atom ($kr \ll 1$, where $k = 2\pi/\lambda$ is the wave vector or light, and r is the position of the electron relative to the atomic nucleus — the wavelength of the light is much larger than the spatial extent of the atom.) allowing the field to be treated as spatially uniform. Second, we assume a slowly varying temporal envelope for the driving field so that it may be represented as a single-frequency carrier with fixed polarisation. Within these approximations, light couples a ground state $|g\rangle$ and an excited state $|e\rangle$, through the matrix element

$$\langle e|\hat{H}_{\text{int}}|g\rangle = -\langle e|\boldsymbol{\mu}|g\rangle \cdot \mathbf{E}(t), \tag{2.14}$$

the central quantity governing optical transitions. The magnitude and structure of this coupling depends both on the atomic wavefunctions and on the polarisation of the light as we shortly see.

2.3.2 Dipole Matrix Elements and Selection Rules

The dipole matrix element factorises naturally into radial and angular contributions. Writing the dipole operator in its spherical-tensor form, the transition strength becomes [44]

$$\langle e|\hat{\mathbf{r}}|g\rangle = \mathcal{R}_{e,g}\mathcal{A}_{e.g}, \tag{2.15}$$

where

$$\mathcal{R}_{e,g} = \int_0^\infty R_e(r) r R_g(r) \mathrm{d}r, \tag{2.16}$$

and, for some nlm gross structure state,

$$\mathcal{A}_{e.g} = (-1)^{m'+\max(\ell,\ell')}\sqrt{\max(\ell,\ell')}\begin{pmatrix} \ell' & 1 & \ell \\ -m' & m-m' & m \end{pmatrix}\delta_{\ell',\ell+1}, \tag{2.17}$$

where δ denotes the Kronecker delta and the () denotes the Wigner-3j coefficient [44]* The radial integral, equation (2.16), determines the overall strength of the transition (and is what is computed in atomic-structure codes such as `arc` [33]), thus influenced by the effective potential discussed in Section 2.2.4. It is this component that varies significantly between Rydberg states and determines the large transition dipoles characteristic of high-n states. The angular part, equation (2.17), follows solely from symmetry and the Wigner–Eckart theorem. It therefore fixes the electric–dipole selection rules [45] which specify the only combinations of quantum numbers for which the dipole matrix element is non-zero and thus the only optical transitions that the atom is permitted to make:

$$\Delta\ell = \pm 1, \tag{2.18}$$

$$\Delta m = 0, \pm 1, \tag{2.19}$$

where the total spin s is unchanged. Physically, this reflects angular momentum conservation between the photon (which carries spin angular momentum $\hbar$) and the atom.

The Δm selection rules can be directly related to the polarisation of the driving light. Linearly polarised light drives $\Delta m = 0$ or 'π' transitions, while circularly polarised light drives $\Delta m = \pm 1$ or '$\sigma^{\pm}$' transitions. Thus, the polarisation state of the light controls which magnetic sublevels are coupled. When fine or hyperfine structure is included, these rules generalise to $\Delta j = 0, \pm 1$, and $\Delta F = 0, \pm 1$ (excluding $0 \leftrightarrow 0$) [39], but the physical origin remains the conservation of angular momentum between the photon and the atom.

*Similar expressions can be constructed for dipole matrix elements when concerning fine- and hyperfine structure states.

2.3.3 Rabi Frequency

For a simple two-level system represented by a ground state, $|g\rangle$, and an excited state, $|e\rangle$, the interaction Hamiltonian may be expressed in matrix form as [45]

$$H_{\text{int}} = \begin{pmatrix} 0 & -\boldsymbol{\mu}_{eg} \cdot \mathbf{E}(t) \\ -\boldsymbol{\mu}_{ge} \cdot \mathbf{E}(t) & 0 \end{pmatrix}, \tag{2.20}$$

where $\boldsymbol{\mu}_{ge} = \boldsymbol{\mu}_{eg}^*$ by Hermiticity. This matrix formulation underlies the description of Rabi oscillations and, more generally, the optical Bloch equations introduced later in this chapter.

The strength of the atom–field coupling is encapsulated in the *Rabi frequency*, defined by

$$\Omega = \frac{1}{\hbar}\, \boldsymbol{\mu} \cdot \mathbf{E}. \tag{2.21}$$

In the case of a monochromatic field with fixed polarisation, Ω provides a direct measure of how strongly the external light drives coherent oscillations between $|g\rangle$ and $|e\rangle$. The time evolution of the populations of these states is then governed by Rabi oscillations at frequency Ω, a phenomenon that forms the basis of many interactions in atomic physics.

2.3.4 Spontaneous and stimulated processes

In addition to this coherent driving, real atoms undergo dissipative processes due to their interaction with the vacuum electromagnetic field [34]. These are described by the Einstein A and B coefficients. The Einstein A coefficient, A_{eg}, gives the spontaneous emission rate for decay from $|e\rangle$ to $|g\rangle$, while the B coefficients describe stimulated absorption and emission in the presence of external radiation. In the dipole picture, the spontaneous emission rate can be related to the dipole matrix element as [34]

$$A_{eg} = \frac{\omega_{eg}^3}{3\pi\epsilon_0\hbar c^3}\, |\boldsymbol{\mu}_{eg}|^2, \tag{2.22}$$

where ω_{eg} is the transition frequency. Equation (2.22) makes clear the link between the strength of coherent driving (through Ω) and the strength of spontaneous decay: both depend on the same dipole matrix element. This balance between coherent excitation and dissipative loss will later appear explicitly in the optical Bloch equations.

2.3.5 Optical Bloch Equations

To describe the time evolution of an atom interacting with light, we must move beyond the wavefunction formalism and instead use the *density matrix* [46]. The density matrix ρ is a matrix-valued operator that provides a complete statistical description of the atomic state, encompassing both pure states and mixed ensembles [47]. Its diagonal elements, ρ_{ii}, describe the populations in each energy level, while the off-diagonal elements, ρ_{ij} with $i \neq j$, represent the atomic *coherences*, the phase relationships between different quantum states. The time evolution of the density matrix is governed by the Gorini–Kossakowski–Sudarshan–Lindblad (GKSL) master equation [48]:

$$\frac{\mathrm{d}\rho}{\mathrm{d}t} = -\frac{i}{\hbar}[\hat{H}, \rho] + \mathcal{L}(\rho), \tag{2.23}$$

where $\hat{H}$ is the Hamiltonian describing coherent evolution, $\mathcal{L}(\rho)$ is the Lindbladian, $[,]$ represents the commutator and i is the imaginary unit. The Lindbladian acts as a superoperator on the matrix ρ and incorporates all non-Hamiltonian processes such as spontaneous emission, collisions, optical pumping, and dephasing. For a decay channel $|e\rangle \to |g\rangle$ with rate Γ, the corresponding Lindblad term takes the standard form

$$\mathcal{L}_{eg}(\rho) = \Gamma\left(\hat{\sigma}_{ge}\rho\,\hat{\sigma}_{eg} - \frac{1}{2}\{\hat{\sigma}_{ee}, \rho\}\right), \tag{2.24}$$

with $\hat{\sigma}_{ij} = |i\rangle\langle j|$ and $\{\cdot,\cdot\}$ the anticommutator. Thus both the Hamiltonian and dissipative contributions act directly on the matrix elements of ρ. Under the rotating-wave approximation (RWA), the atom–light interaction Hamiltonian for a

two-level atom driven with Rabi frequency Ω and detuning $\Delta = \omega_L - \omega_{eg}$ is

$$\hat{H} = -\frac{\hbar\Delta}{2}\hat{\sigma}_{ee} + \frac{\hbar\Omega}{2}(\hat{\sigma}_{eg} + \hat{\sigma}_{ge}). \tag{2.25}$$

Substituting this Hamiltonian and the Lindblad operator for spontaneous emission into Eq. (2.23), and evaluating each matrix element explicitly, yields a set of coupled differential equations known as the optical Bloch equations [34]:

$$\dot{\rho}_{ee} = -\Gamma\rho_{ee} + \frac{i\Omega}{2}\left(\rho_{ge} - \rho_{eg}\right), \tag{2.26}$$

$$\dot{\rho}_{gg} = +\Gamma\rho_{ee} - \frac{i\Omega}{2}\left(\rho_{ge} - \rho_{eg}\right), \tag{2.27}$$

$$\dot{\rho}_{eg} = \left(i\Delta - \frac{\Gamma}{2}\right)\rho_{eg} + \frac{i\Omega}{2}\left(\rho_{ee} - \rho_{gg}\right). \tag{2.28}$$

Each component ρ_{ij} then evolves through a combination of coherent driving terms proportional to Ω and Δ, arising from $[\hat{H}, \rho]$ and dissipative relaxation terms proportional to Γ, arising from $\mathcal{L}(\rho)$.

In this thesis, the atomic ensemble reaches equilibrium well before measurements are taken: optical pumping, population transfer, and coherence dynamics occur on microsecond timescales, while data acquisition takes place on millisecond timescales or longer. Thus we typically solve for the steady state, i.e., all $\dot{\rho}_{ij} = 0$. The resulting steady-state density matrix encodes the complete optical response of the medium. The optical Bloch equations thus form the theoretical backbone for describing electromagnetically induced transparency, Rabi oscillations, optical pumping, and the steady-state absorption spectra observed throughout this thesis. All later modelling of Rydberg EIT and rf-coupled Rydberg systems uses this framework, extended to include more levels, and Doppler averaging.

The coupled linear equations formed by (2.23) are solved computationally using code based upon [49] in chapter 4. In later chapters we use another open-source software, `rydiqule` [50]. Both programs compute (2.23) based upon user input and then solve the set of coupled linear equations.

2.3.5.1 Dephasing

In real experimental systems, the decay of the atomic coherence ρ_{eg} is not governed solely by spontaneous emission. Other processes, referred to as dephasing, contribute to the loss of phase coherence between different atomic states without necessarily changing their populations.

The total decoherence rate of the optical coherence can therefore be written as some

$$\gamma_{ij} = \frac{\Gamma_{ij}}{2} + \gamma_\phi, \tag{2.29}$$

where the first term, $\Gamma_{ij}/2$, arises from population relaxation due to spontaneous emission, from some state $|i\rangle$ to some state $|j\rangle$ (as introduced in Section 2.22), and γ_ϕ represents an additional dephasing rate.

Sources of dephasing include:

- **Laser linewidth:** Finite spectral width of the driving field introduces phase noise, effectively broadening the transition and leading to random fluctuations in the optical phase [51].
- **Transit-time broadening:** In thermal vapour experiments, atoms move in and out of the laser beams, interrupting the interaction [52].
- **Collisional dephasing:** Elastic collisions between atoms, with a buffer gas or the cell walls can randomise the atomic phase without causing population transfer [52].

Including dephasing modifies the optical Bloch equations by replacing $\Gamma_{ij}/2$ in the coherence term with a more general γ_{ij}:

$$\dot{\rho}_{eg} = (i\Delta - \gamma_{eg})\,\rho_{eg} + \frac{i\Omega}{2}(\rho_{ee} - \rho_{gg}). \tag{2.30}$$

This term accounts for both spontaneous decay and all other mechanisms. Together, these processes form the realistic picture of atom–light interactions, where excitation,

spontaneous emission, and dephasing shape the internal dynamics of the atom. In the next section, we will see how these processes form the measurement used to make a sensor.

2.4 Rydberg Atom RF Sensing

We have so far described the dynamics of a single atom interacting with an external field. We now turn to how this picture is applied in a real Rydberg sensor, where the measurement signal arises from EIT and not from one atom but from a thermal ensemble of atoms inside a small glass vapour cell. In this setting the atoms move, experience Doppler shifts, and collectively determine the transmission of the probe laser.

Most Rydberg-atom-based rf sensors make use of electromagnetically induced transparency (EIT) [53, 26, 54], a coherent and non-destructive process that couples the properties of the Rydberg state to an optical transition from the atomic ground state, thereby allowing the perturbative effect of an incoming rf electric field on the Rydberg state, to be mapped onto an optical probe field, which is detected using a photodetector [27, 55]. This EIT technique effectively enables sensitive and SI-traceable measurements of RF electric fields to be extracted from an optical signal [56].

2.4.1 Electromagnetically Induced Transparency (EIT)

Electromagnetically induced transparency (EIT) is a coherence effect in which an otherwise absorbing medium becomes transparent to a weak probe field in the presence of a strong coupling field [57]. In Rydberg systems, EIT provides a highly sensitive and non-destructive means of probing atomic coherence and detecting external electromagnetic fields [52].

In a typical ladder configuration, a weak probe laser couples the ground state $|g\rangle$ to an intermediate excited state $|e\rangle$, while a strong coupling laser connects $|e\rangle$ to a highly excited Rydberg state $|r\rangle$. In the absence of the coupling field, atoms excited to $|e\rangle$ rapidly decay, resulting in strong absorption of the probe field.

When the coupling field is applied, it drives coherent Rabi oscillations between $|e\rangle$ and $|r\rangle$, such that excitation to $|e\rangle$ can occur both directly from the probe field and indirectly through coupling to the Rydberg state. At exact two-photon resonance, these excitation amplitudes interfere destructively, suppressing population of the intermediate state and therefore preventing absorption of the probe field. At exact two-photon resonance, these excitation amplitudes interfere destructively, suppressing population of the intermediate state. As a result, the atom can no longer efficiently absorb probe photons despite the probe remaining resonant with the $|g\rangle \rightarrow |e\rangle$ transition.

This destructive interference leads to the formation of a non-absorbing "dark state"

$$|D\rangle \propto \Omega_c |g\rangle - \Omega_p |r\rangle , \tag{2.31}$$

where Ω_p and Ω_c are the probe and coupling Rabi frequencies, respectively. Within this coherent superposition state, the system becomes effectively decoupled from $|e\rangle$ and probe absorption is suppressed.

In the density matrix formalism, this corresponds to cancellation of the coherence term ρ_{ge}, whose imaginary component determines probe absorption. The suppression of $\mathrm{Im}(\rho_{ge})$ produces a narrow transparency window in the probe transmission spectrum, as shown in Fig. 2.2, while the associated steep variation in $\mathrm{Re}(\rho_{ge})$ gives rise to strong dispersion. This dispersive response underpins applications such as slow light [58].

In Rydberg EIT-based rf sensing, an additional radio-frequency field couples two nearby Rydberg states, typically denoted $|r\rangle$ and $|r'\rangle$. This introduces an extra coherence into the density matrix and alters the optical response of the medium. Depending on the rf amplitude and detuning, this coupling can generate features

such as Autler–Townes splitting [59], in which the original EIT resonance divides into two distinct components whose separation directly yields the rf Rabi frequency $\Omega_{rr'}$ [29].

EIT therefore provides a mechanism by which microscopic atomic coherences are imprinted onto the optical absorption experienced by the probe laser. The density matrix and optical Bloch formalism introduced earlier predict these absorption features, and will be used throughout this work to model spectra.

2.4.2 Probe Laser Transmission

In this section we show how the atomic coherences calculated via the density matrix give rise to the macroscopic electric susceptibility experienced by the probe, and how this susceptibility ultimately determines the measured probe transmission. Consider a weak probe laser driving the $|g\rangle \leftrightarrow |e\rangle$ transition in an ensemble of N atoms per unit volume. Each atom develops a microscopic dipole moment, $\mathbf{p}$ [60, 47]

$$\mathbf{p} = \boldsymbol{\mu}_{eg}\, \rho_{ge}, \tag{2.32}$$

where $\boldsymbol{\mu}_{eg}$ is the transition dipole matrix element and ρ_{ge} is the coherence between the ground and excited states. The macroscopic polarisation or polarisation density, $\mathbf{P}$, of the ensemble is then simply the sum over all atoms [60]:

$$\mathbf{P} = N\,\mathbf{p} = N\,\boldsymbol{\mu}_{eg}\,\rho_{ge} \tag{2.33}$$

Here, N scales the microscopic response to the collective medium response. The polarisation is also related to the applied probe field $\mathbf{E}_{\mathrm{p}}(t)$ via the complex electric susceptibility χ:

$$\mathbf{P} = \varepsilon_0\, \chi\, \mathbf{E}_{\mathrm{p}}. \tag{2.34}$$

Comparing this to the previous expression, we see that the susceptibility is directly proportional to the atomic coherence and can be found as:

$$\chi = -\frac{2N\,|\boldsymbol{\mu}_{eg}|^2}{\hbar\epsilon_0\Omega_{ge}}\rho_{ge}. \tag{2.35}$$

The complex susceptibility $\chi = \chi' + i\chi''$ encodes both the dispersion, χ' or equivalently $\mathrm{Re}(\chi)$, and absorption, χ'' or equivalently $\mathrm{Im}(\chi)$, properties of the medium.

The propagation of the probe field through an atomic vapour is commonly described using Beer's law [34]. For a medium of length L, the probe intensity obeys

$$I(L) = I(0)\, e^{-\alpha L}, \tag{2.36}$$

where $\alpha = k\,\mathrm{Im}(\chi)$ is the absorption coefficient and k is the probe wavevector [61]. The corresponding measurable transmission is therefore,

$$T = \frac{I(L)}{I(0)} = e^{-k\,\mathrm{Im}(\chi)\,L}. \tag{2.37}$$

Equation (2.37) follows from a susceptibility χ is assumed to be uniform throughout the medium. This is accurate when the optical depth, $k\,\mathrm{Im}(\chi)L$, is not too large i.e., when the vapour is *optically thin*. In this regime, the probe intensity (or other field intensities) does not vary dramatically over the length of the cell, and the coherence ρ_{ge} (which determines χ) may be taken as constant along the propagation direction.

For high number density, long vapour cells, or conditions in which resonances lead to strong absorption, this approximation begins to fail. A large optical depth means that the probe is significantly attenuated as it propagates. Because the atomic response depends on the local probe intensity, the susceptibility becomes position-dependent, $\chi \to \chi(x)$, and Beer's law no longer captures the correct nonlinear propagation.

A more complete treatment couples Maxwell's wave equation for the probe field to the density-matrix (Bloch) equations describing the atomic medium, leading to the full *Maxwell–Bloch equations* [62]*. However, for the purposes of this work, where the vapour is operated in a regime of modest optical depth and the probe remains weak, the approximation of a uniform susceptibility and Eq. (2.37) provide an accurate and computationally efficient description of the probe transmission.

*For an application to Rydberg sensing see e.g. [63] or [64]

This derivation establishes the clear chain of causality:

$$\rho_{ge} \longrightarrow \chi \longrightarrow \mathrm{T},$$

showing that the probe transmission measured in the experiment directly reflects the underlying atomic coherence induced by the light fields. This is a key result used and, more often, observed throughout this thesis. Anything that modifies the atomic coherence directly determines the optical transmission that we detect experimentally when the power of the probe laser is detected.

2.4.3 Effect of Doppler Broadening

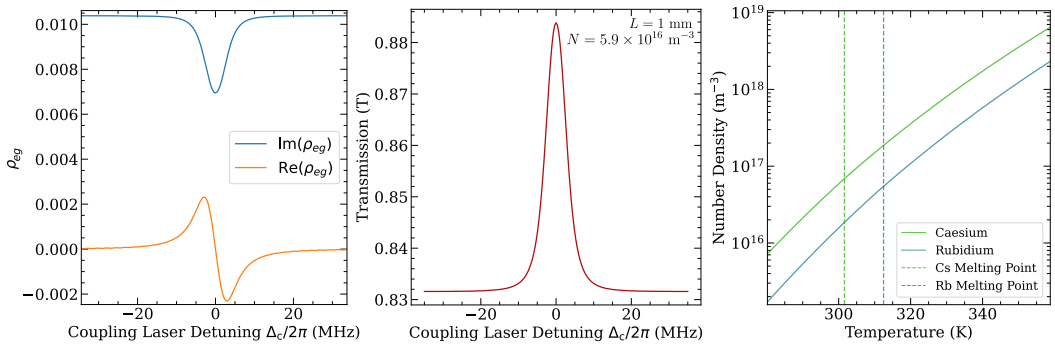

Figure 2.2: Overview of EIT of a three-level system in an atomic ensemble. *Left:* Doppler broadened electric susceptibility, χ, of a three level system with $\Omega_e = 2\pi \times 4\,\mathrm{MHz}$ and $\Omega_g = 2\pi \times 2\,\mathrm{MHz}$ showing the imaginary part, leading to absorption, and the real part, leading to a phase shift. *Middle:* EIT in a three-level system as part of a Doppler-broadened atomic ensemble with $L = 1\,\mathrm{mm}$, and number density $N = 5.9 \times 10^{16}\,\mathrm{m}^{-3}$. *Right:* Plot of the number density of two alkali-metal atoms, rubidium and caesium showing the drastic increase with temperature.

In a thermal vapour, atoms possess a velocity distribution that shifts the effective laser detuning through the Doppler effect. For an atom moving with velocity component v along the probe propagation direction, the probe detuning becomes

$$\Delta_\mathrm{p} \rightarrow \Delta_\mathrm{p} - k_\mathrm{p} v, \tag{2.38}$$

where k_p is the probe wavenumber. Similarly, any coupling or rf field with wavenumber k_i acquires the corresponding Doppler term $-k_i v$.

The ensemble susceptibility is obtained by averaging the single-velocity susceptibility $\chi(v)$ over the one-dimensional Maxwell–Boltzmann distribution

$$f(v) = \frac{1}{u\sqrt{\pi}} \exp\left(-\frac{v^2}{u^2}\right), \qquad u = \sqrt{\frac{2k_{\mathrm{B}}T}{m}}, \tag{2.39}$$

yielding the Doppler-broadened susceptibility

$$\chi_{\mathrm{D}}(\omega) = \int_{-\infty}^{+\infty} \chi(\Delta_{\mathrm{p}} - k_{\mathrm{p}}v)\ f(v)\, dv. \tag{2.40}$$

Doppler averaging generally broadens spectral features and reduces peak contrast.

For ladder-type EIT systems, the choice of counter-propagating probe and coupling beams can partially cancel Doppler shifts on the two optical transitions, narrowing the effective linewidth of the EIT resonance. In contrast, rf and THz fields contribute negligibly to Doppler broadening, since their associated wavevectors are much smaller than those of the optical fields.

Fig. 2.2 summarises these relationships by showing how the atomic coherence determines the susceptibility and, in turn, the probe transmission in a Doppler-broadened atomic ensemble.

2.5 Sensing Primer

Rydberg atoms have rapidly emerged as a versatile platform for precision electromagnetic field sensing. The last decade has seen an explosion of progress, with Rydberg-based receivers achieving state-of-the-art performance in the measurement of RF electric-field amplitude [65], frequency [66], and phase [65, 67], as well as vector quantities such as polarisation [68] and angle of arrival [69]. More recently, the intrinsically broadband nature of Rydberg transitions has enabled simultaneous detection across multiple independent frequency bands [70, 71].

Although alternative readout mechanisms exist such as fluorescence detection [72, 73], photon conversion [74], and ion-counting approaches [75], EIT remains the most

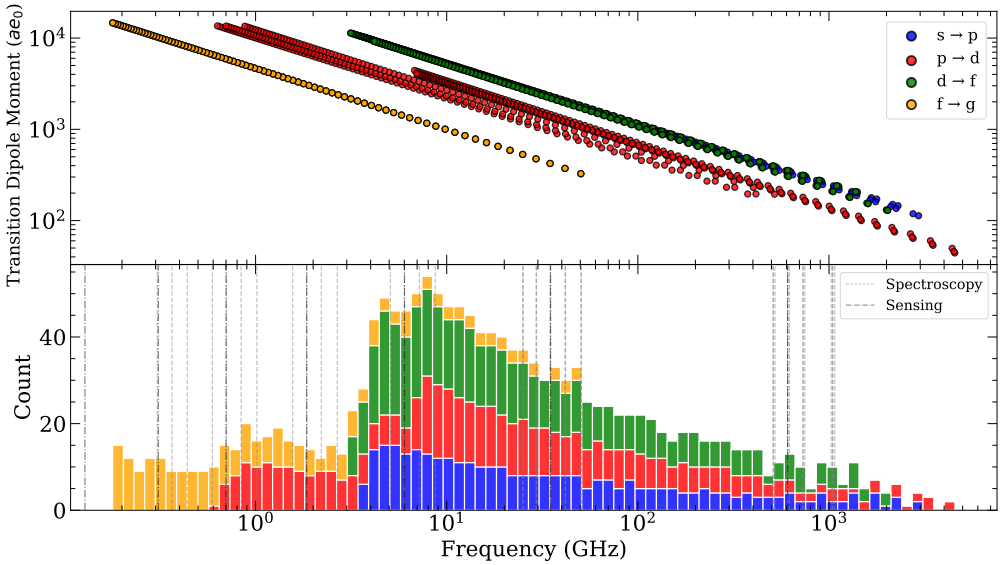

Figure 2.3: Overview of transition frequencies in caesium accessible using two- and three-photon methods and their distribution across the radio spectrum. These include all dipole allowed $\ell_j \to (\ell+1)_{j'}$ but exclude transitions with negligible radial overlap (those far-separated, e.g. $40s \to 50p$) are omitted, as they produce dipole moments too small to be driven appreciably. *Above:* Plot of the dipole matrix element against logarithmically spaced transition frequencies for different dipole allowed transitions in the range $n = 15$–100. *Below:* A histogram showing the distribution of logarithmically-binned transition frequencies and their count for the selected dipole allowed transitions. The dashed vertical lines show the transition frequencies that are used throughout this thesis for spectroscopy or sensing purposes. Some of these lines use higher ℓ transitions not shown in either plot.

widely adopted technique for RF sensing. Its combination of high sensitivity, non-destructive readout, (relative) experimental ease and direct traceability to fundamental atomic constants makes it particularly attractive for metrology applications. Accordingly, throughout this thesis, we focus exclusively on EIT-based schemes. A key advantage of Rydberg atoms is the vast range of accessible transition frequencies in the RF, microwave, and THz domains. Because the Rydberg level structure becomes increasingly dense with higher principal quantum number, two- and three-photon schemes* can address transitions spanning several orders of magnitude in frequency. Fig. 2.3 illustrates this broadband coverage by mapping the dipole matrix element and transition frequency for allowed Rydberg transitions between $s \to p, p \to d, d \to f$ and $f \to g$ states in caesium.

*Referring to the number of lasers needed to address Rydberg states.

The upper panel shows the frequency–dipole-moment relationship, highlighting how the enormous radial matrix elements associated with high-n Rydberg states lead to strong RF coupling even at very weak electric-field amplitudes. The lower histogram demonstrates the natural distribution of transition frequencies across the $0.1\text{–}1 \times 10^3$ GHz range, indicating that suitable transitions exist for essentially any frequency of interest within this band although it is most densely packed around 10 GHz. This clustering means that practical operation is naturally biased toward the microwave band, where suitable transitions are abundant. Conversely, outside this region, the sparser transition landscape limits flexibility but points towards better use-case as traditional technologies are poorer in higher frequency regions (> 100 GHz) [76] and, additionally, Rydberg sensors offer an interesting case of small sensor size for lower frequency (longer wavelength) detection [77].

The vertical dashed lines mark the particular transitions used in this thesis for spectroscopy and sensing. Some involve higher angular-momentum states not displayed for clarity, but the overall picture emphasises the intrinsic spectral flexibility of Rydberg systems. Together, this broad frequency coverage, electric-field sensitivity, and optical readout capability form the foundation for the sensing techniques developed and explored in the following chapters.

2.6 Conclusion

This chapter has established the theoretical backbone of the work presented in this thesis. We first built up the structure of the Rydberg atom from its hydrogenic origins, identifying the quantum numbers, wavefunctions, and matrix elements that govern its behaviour. We then developed the framework for light–atom interactions, beginning with the electric-dipole Hamiltonian and progressing through dipole selection rules, Rabi coupling, and spontaneous decay. The density-matrix and optical Bloch formalism provided the language needed to describe coherent evolution in the presence of dissipation, while the calculation of electric susceptibility linked

these atomic coherences directly to the measurable probe transmission. Extending the picture to a thermal vapour introduced Doppler effects and averaging procedures, yielding the realistic lineshapes central to Rydberg EIT spectroscopy. Finally, we used these concepts to motivate the operating principles of Rydberg-based RF sensors and to illustrate the broad frequency coverage enabled by the Rydberg level structure.

We are now equipped to construct a practical Rydberg sensor. The next chapter turns to the experimental tools that make these ideas into an experiment. We detail the design of a novel coupling laser, the optical layout for probe and coupling beams, laser frequency stabilisation, RF delivery schemes, and the control and data-acquisition infrastructure. Following this, all remaining measurements in this thesis are built, and they translate the theoretical mechanisms developed here into a functioning experiment.

Chapter 3

Experimental Methods

3.1 Introduction

In this work, Rydberg atoms are realised using a thermal vapour of caesium atoms contained within a glass cuvette. The atoms are optically excited using a sequence of laser fields at well-defined wavelengths to reach highly excited electronic states. By monitoring the transmitted power of one of these laser beams using a photodetector, information about the amplitude and frequency of external rf fields interacting with the atoms can be inferred. This chapter describes the key experimental methods required to generate and detect these Rydberg excitations, and how the measured atomic response can be used for rf field sensing.

Caesium is particularly well suited to such experiments owing to its convenient optical transition wavelengths, large dipole moments between Rydberg states, and high vapour pressure, giving a large number of atoms, at room temperature. These features enable strong light–atom interactions and sufficient optical depth in a

small package to be able to readily detect using an optical probe. The following section introduces the relevant energy level structure of caesium and outlines how the applied optical and rf fields are used to access the required atomic states.

3.2 Atomic System

The experiments in this thesis focus on the low-lying Rydberg states of the caesium atom. An ensemble of atoms within a vapour cell is excited using two optical lasers and a series of applied rf fields. The relevant energy levels explored throughout the thesis are illustrated in the top left of Fig. 3.1 and give an overview of the scale of energies involved.

The first ('probe') laser at 852 nm couples the ground state $6s_{1/2},\ F = 4$ to the excited $6p_{3/2},\ F = 5$ state via an electric dipole transition. Other specific hyperfine levels of these states* can be addressed by changing ('detuning') the frequency of the laser. This becomes relevant when we discuss stabilising these lasers to specific hyperfine levels in section 3.5. At these low principal quantum numbers, the energy spacing between adjacent n states is large ($\sim$1 eV), several orders of magnitude greater than the energy of the rf fields we aim to study ($\sim$ 10–100 µeV).

To reach Rydberg states where adjacent levels are much more closely spaced, a second ('coupling') laser couples the $6p_{3/2}$ state to Rydberg states with principal quantum numbers n = 18–22 and angular momentum $\ell = 2,\ j = 3/2, 5/2$, as determined by the accessible laser wavelengths. These states are shown in the top right of Fig. 3.1. In this region, the separation between dipole-allowed transitions lies in the range of 0.1–1 THz. The strong deviation of the low–ℓ (s, p, and d) states from the hydrogenic manifold ($\ell \geq 3$) is a consequence of their large quantum defects, which cause them to lie significantly lower in energy than the nearly degenerate high–ℓ states of similar n.

*Spaced $\simeq$ 100 MHz apart, see [78]

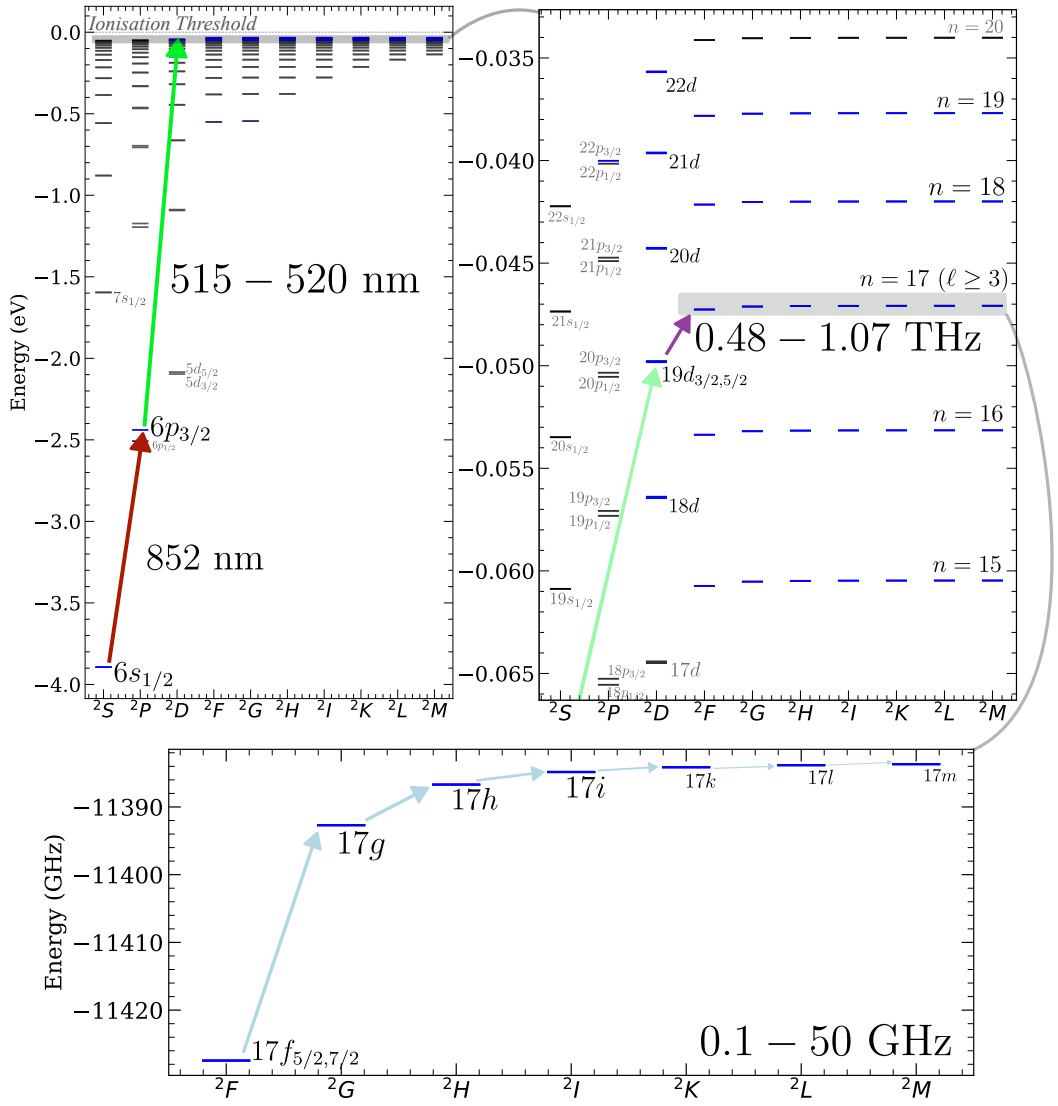

Figure 3.1: Energy level diagram showing the energy levels of caesium at different scales and principal quantum numbers. Additionally, we display the excitation scheme(s) used in this thesis ($5 \leq n \leq 22,\ 0 \leq \ell \leq 9$). Grey regions highlight the next panel (clockwise) *Top left:* The 852 nm probe laser (red arrow) couples the $6s_{1/2}$ ground state and the first excited $6p_{3/2}$ state, where a 515–520 nm coupling laser (green) couples to a range of high-lying states. *Top Right:* The caesium energy level 'neighbourhood' of the Rydberg states used (blue) throughout this thesis ($17 \leq n \leq 22,\ 0 \leq \ell \leq 9$), showing the nf states that are coupled using a range of THz transitions (purple) from the nd states. The range of THz frequencies used is shown. The nd states have fine structure which is not resolved at the scale shown in the diagram. *Bottom:* The (nearly) hydrogenic energy levels of the high angular momentum states explored in this thesis ($n = 17,\ 3 \leq \ell \leq 9$). Microwave fields are used to couple these states using radiowaves of various frequency in the range 0.1–50 GHz.

Focusing on these high–ℓ states (bottom of Fig. 3.1), we find that their energy separations decrease monotonically with increasing ℓ. Owing to their small separations, transitions between adjacent states can be driven by electromagnetic fields in the microwave and rf regime (<100 GHz). For the principal quantum numbers used in this work, these energy separations correspond to frequencies of approximately 0.1–50 GHz. The optical and rf systems used to produce and control these fields are described in detail later in this chapter.

3.3 Laser Systems

3.3.1 Probe Laser

The first optical source in the experiment is an infrared probe laser operating at 852 nm, resonant with the $6s_{1/2} \rightarrow 6p_{3/2}$ transition in caesium. The system is a commercial external-cavity diode laser (ECDL) supplied by *Toptica Photonics* (DL Pro), providing up to 40 mW of single-frequency output with a linewidth below 1 MHz. Diode lasers are compact semiconductor devices that generate coherent light through stimulated emission in a semiconductor junction. However, their native emission typically consists of multiple longitudinal modes and has a relatively broad linewidth (tens of MHz). Incorporating the diode into an external cavity allows for single-mode, narrow-linewidth operation and tunability by selecting and feeding back a single longitudinal mode. Coarse wavelength tuning is achieved by translating a diffraction grating, by applying a voltage to a piezo actuator. Fine adjustments of the wavelength are made through current adjustment of the diode. The laser frequency is actively stabilised using polarisation spectroscopy on the same transition, described in 3.5. This laser serves as the probe field in the Rydberg EIT scheme described.

3.3.2 Coupling Laser

Here we describe the design and operation of the coupling laser system used to excite atoms into Rydberg states. The initial aim was to access relatively low-lying Rydberg states ($n \approx 15$–25), for which the transitions to neighbouring states lie in the millimetre-wave and terahertz regions, frequencies of interest in previous work by this group for imaging and sensing applications [79, 80, 81]. Compared to higher-lying Rydberg levels, these states require excitation at slightly longer wavelengths, corresponding to photon wavelengths in the 515–520 nm range. This spectral region lies significantly above the typical 509 nm transitions commonly used for Cs Rydberg excitation, and therefore necessitated the development of a custom laser system capable of providing high output power, and broad tunability in this wavelength range.

To couple atoms to high-lying Rydberg states, the field must drive transitions with sufficiently large Rabi frequencies, which require high optical intensity at the target wavelength. The system implemented here is a Master Oscillator Power Amplifier (MOPA) configuration combined with second-harmonic generation (SHG). In a MOPA, a low-power, narrow-linewidth 'seed' laser (the master oscillator) is amplified by a high-power optical amplifier. Instead of directly generating visible light (400–700 nm), we use high power infrared light and double its frequency. Operating at near-infrared (NIR) wavelengths offers several advantages: semiconductor gain media in this region are capable of producing watt-level powers with good beam quality and stability. The visible light needed for Rydberg excitation is then produced by frequency doubling the NIR output using a non-linear crystal, a process known as SHG, in which two photons of frequency ω combine to form one photon of frequency 2ω in a phase-matched medium [62]. This approach is widespread in modern atomic physics experiments, as directly lasing, e.g. by using a diode, at visible wavelengths is considerably less efficient and typically limited to several milliwatts of output power unless at certain specific wavelengths.

Commercial high-power SHG systems meeting these specifications are often costly and optimised for standard wavelengths. Consequently, homebuilt frequency-doubling systems have become common in atomic and molecular physics, particularly when high power is required at non-standard wavelengths [82]. In this chapter, we detail such a system using an external-cavity diode laser (ECDL) operating around 1030−−1040 nm to seed a tapered amplifier, followed by coupling into a bow-tie enhancement cavity for frequency doubling to produce tunable 515–520 nm light.

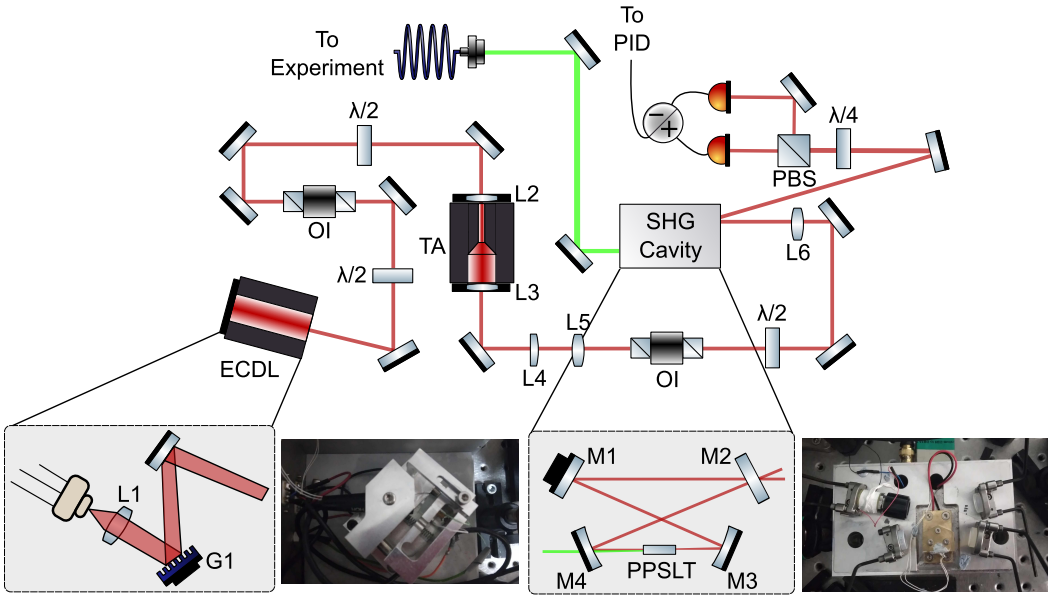

Figure 3.2: Diagram showing a homebuilt SHG MOPA laser system. $\lambda/2$ - Half-wave plate, $\lambda/4$ - Quarter-wave plate, OI - Optical Isolator, TA - Tapered Amplifier, PBS, polarising beam-splitter. *Above:* The beam diagram and optical layout of the MOPA system is shown for the production of high power infrared light to be subsequently frequency doubled. An ECDL laser produces coherent light which then passes through an optical isolator and a tapered amplifier chip for subsequent second harmonic generation of the amplified infrared light. The beam is focused inside the cavity where a standing wave is formed. Infrared light that traverses the cavity is and transmitted back through M2 is used to form the cavity lock. The frequency-doubled output beam passes through M4, a dichroic, where it is then launched into a fibre to be used in experiment. *Lower Left:* Internal diagram showing the layout of the ECDL laser where light from a laser diode is collimated and retro-reflected from a diffraction grating. A photograph of the assembled ECDL is shown beside the diagram. *Lower Right:* Internal diagram of the SHG bow-tie cavity detailing the 4 mirrors and the non-linear crystal where frequency doubling takes place. A photograph of the assembled cavity is shown beside the diagram, showing the brass oven containing the crystal and a thermistor to monitor temperature.

3.3.2.1 External Cavity Diode Laser (ECDL)

The seed source is a *Sacher Lasertechnik* (SAL-1030-060) laser diode integrated into a home-built ECDL in a modified Littrow configuration [83]. In the Littrow design shown in Fig. 3.2, a diffraction grating (*Thorlabs* GH13-12V), G1, is used as the wavelength-selective element. Light from the diode is first collimated using a short aspheric lens, L1. The first-order diffraction of the light from the grating is reflected back into the diode to form optical feedback, while the zeroth-order reflection provides the output beam. By adjusting the grating angle, one can select which longitudinal mode of the diode cavity is resonant with the external cavity, thus tuning the laser wavelength. Fine tuning is achieved through small adjustments to the grating angle using a piezoelectric actuator, while coarse tuning is obtained via temperature control of the diode, which changes the refractive index and gain spectrum of the semiconductor material or by mechanically tuning the angle grating.

The combined length of the diode and external cavity (typically a few centimetres) determines the mode spacing, which is on the order of a few GHz. The temperature is stabilised using a thermoelectric Peltier element set within the mechanical mount pictured with feedback control to within 0.01 K to ensure mode stability.

The ECDL output used is approximately 20 mW, sufficient to seed the tapered amplifier. Although higher seed powers can be achieved, the amplifier output does not scale linearly with input power due to gain saturation and mode-matching effects. Instead, the seed power is optimised to balance amplifier stability, beam quality, and output efficiency. This is changed as mostly dictated by mode-matching of the doubling cavity as will be discussed.

To prevent unwanted optical feedback, out of the back facet of the tapered amplifier, from destabilising the diode, an optical isolator is placed immediately after the ECDL. A half-wave plate (HWP, $\lambda/2$) before the isolator ensures maximum transmission, while a second HWP after the isolator adjusts the polarisation to match the input requirements of the optical amplifier.

3.3.2.2 Tapered Amplifier and Beam Preparation

The output of the external-cavity diode laser (ECDL) is coupled into a semiconductor tapered amplifier (TA; Coherent model TA-1060-2000), which provides optical gain over the wavelength range 1035–1040 nm, yielding an output power of up to approximately 1 W.

Semiconductor optical amplifiers, such as the TA, consist of a gain-guided waveguide structure with an input ridge section followed by a laterally broadened taper region, allowing amplification to high powers while maintaining reasonable beam quality. The amplification spectrum is centred around the designed gain peak (here, ~ 1060 nm), though some gain remains available at shorter wavelengths closer to our target region.

The seed beam from the ECDL is coupled into the narrow ridge section of the TA using a short focal-length aspheric lens (L2), which focuses the beam to match the mode size of the input waveguide. Efficient coupling is highly sensitive to alignment. The procedure is typically carried out by monitoring the emission from the back facet of the amplifier chip, which provides a visual reference for overlap of the ECDL beam and the facet of the TA. By collimating this back-facet light using L2, the ECDL beam can be steered with two preceding mirrors to achieve spatial overlap at the input facet. The TA output from the front facet (following L3) is continuously monitored on a power meter, and the alignment is optimised for maximum amplified output power, which serves as an indirect indicator of mode matching.

The TA is mounted in a custom-designed housing that provides mechanical stability, thermal management, and fine alignment of mode-matching lenses for the TA. The mount includes a Peltier thermoelectric cooler connected to a temperature controller for thermal stabilisation, and a large aluminium heat sink to dissipate the substantial thermal load generated at the high operating currents required by the TA. Two anti-reflection (AR) coated aspheric lenses (L2 and L3) are integrated into the housing to couple light into and out of the TA chip.

The amplified output beam exhibits strong astigmatism and ellipticity, arising from the asymmetric geometry of the amplifier's tapered region. To produce a near-Gaussian spatial profile suitable for efficient coupling into the second-harmonic generation (SHG) cavity, the beam is passed through a series of mode-correcting optics. The sequence of lenses and optical elements used is illustrated schematically in Fig. 3.2.

The first element (L3) is a short focal-length aspheric lens that collects the divergent beam, followed by a cylindrical lens (L4) that corrects for the horizontal divergence. A second cylindrical lens (L5) is used to complete the collimation, yielding a more symmetric beam profile. The output then passes through an optical isolator to suppress optical feedback from the bow-tie cavity, and a half-wave plate is inserted to align the polarisation with the phase-matching axis of the non-linear crystal.

The final beam-shaping lens (L6, $f = 300\,\mathrm{mm}$) is positioned such that its focal point coincides with the centre of the non-linear crystal within the bow-tie doubling cavity. The positions of the cylindrical and collimating lenses are iteratively adjusted to maximise the SHG power, which serves as a proxy for optimal mode matching.

Achieving a high-quality Gaussian mode is needed for efficient coupling into the SHG cavity, as poor beam quality can drastically reduce the intra-cavity power build-up and therefore the overall conversion efficiency.

3.3.2.3 Bow-tie Cavity and Second Harmonic Generation

The generation of 515–520 nm light for Rydberg excitation is achieved via second-harmonic generation (SHG) in a resonant bow-tie optical cavity. A bow-tie cavity consists of four mirrors arranged in a unique geometry that allows for propagation of light in a square or 'bow-tie' geometry (see Fig. 3.2). Such cavities are widely used for SHG because they support tight focusing in the non-linear crystal while maintaining good spatial mode quality and efficient coupling to external beams. The travelling-wave nature of the bow-tie geometry also suppresses spatial hole burning,

improving frequency stability and reducing multi-mode operation compared to standing-wave cavities.

Optical cavities act as frequency-selective resonators, supporting standing-wave modes at discrete frequencies separated by the free spectral range (FSR). The FSR depends on the total (path) cavity length, L, and the refractive index, n, of the medium within the optical path,

$$\Delta\nu_{\mathrm{FSR}} = \frac{c}{nL}. \tag{3.1}$$

For the cavity used here, which contains a nonlinear crystal, the measured FSR is approximately 1GHz. This spacing is sufficiently small that at least one cavity resonance lies within the mode-hop-free tuning range of the seed ECDL, allowing reliable locking of the cavity to the laser frequency and efficient intracavity power build-up.

The cavity is composed of four mirrors: a planar input coupler (M2, *LayerTec* 103406, $\mathrm{T}_1 = 0.96$), a second planar mirror (M1, *LayerTec* 101041) mounted on a piezoelectric actuator for cavity-length control, and two concave mirrors (M3, and M4, both *LayerTec* 102289) with radii of curvature of 30 mm. The final mirror (M4) serves as the output coupler, with high transmission ($> 95\%$) at the second-harmonic wavelength (515–520 nm) and high reflectivity ($> 99.5\%$) at the fundamental wavelength. The curved mirrors are positioned such that the cavity focuses to a specific beam waist at the centre of the non-linear crystal, optimised according to Boyd–Kleinman theory [84]. Theoretical estimates for these positions are obtained using ray-transfer matrix analysis*, and *many* adjustments are made empirically to maximise the generated second-harmonic power.

The frequency doubling stage uses two periodically poled stoichiometric lithium tantalate (PPSLT) crystals (poling periods 7.28 µm and 7.35 µm, dimensions $0.65 \times 2 \times 20$ mm). PPSLT is chosen for its large effective nonlinear coefficient, high optical damage threshold, and superior resistance to moisture and thermal cycling compared

*J. Pritchard, private communication

with more traditional nonlinear materials such as Lithium niobate (PPLN). When the intense intra-cavity field propagates through the crystal, the induced nonlinear polarisation generates radiation at twice the optical frequency, producing the green output. The nonlinear response of the medium may be expanded in powers of the electric field [62],

$$\mathbf{P} = \varepsilon_0 \left(\chi^{(1)}\mathbf{E} + \chi^{(2)}\mathbf{E}^2 + \chi^{(3)}\mathbf{E}^3 + \cdots \right) \tag{3.2}$$

where a non-zero second-order susceptibility $\chi^{(2)}$ enables second-harmonic generation. In classical terms, SHG corresponds to the nonlinear polarisation oscillating at 2ω, which acts as a source term driving coherent emission at the doubled frequency. In quantum terms, it is the annihilation of two ω photons and the creation of a single 2ω photon, consistent with energy conservation. Efficient SHG requires that the nonlinear polarisation and the generated second-harmonic field remain in phase as they propagate. However, due to material dispersion, the phase velocities of the ω and 2ω waves generally differ, causing destructive interference and poor conversion efficiency over the length of the crystal [85]. Quasi-phase matching (QPM) circumvents this by periodically inverting the sign of $\chi^{(2)}$ [85]. The condition for first-order QPM is:

$$k_{2\omega} = 2k_{\omega} + \frac{2\pi}{\Lambda}, \tag{3.3}$$

where Λ is the poling period. Thermal expansion and the temperature dependence of the refractive indices both shift this condition, so the phase-matching wavelength can be tuned by temperature. Each PPSLT crystal therefore provides a tunable window around its design wavelength.

In the experiment, the crystal is mounted in a temperature-stabilised oven (operating in the range 30–105 °C) inside the doubling cavity. The quasi-phase-matching point is identified by maximising the green output power, which shows the expected sinc^2-like dependence on crystal temperature around the optimum. The beam's polarisation is adjusted using a half-wave plate before the cavity to ensure coupling to the correct non-linear component. In PPSLT, two extraordinarily polarised

fundamental photons combine to generate an extraordinarily polarised second-harmonic photon [86, 87]. This orientation maximises the effective non-linear coefficient d_{eff}, a key parameter governing the overall conversion efficiency. Here, extraordinary polarisation refers to light whose electric field lies in the plane containing the optical axis of the crystal, experiencing an effective refractive index that depends on the propagation direction.

The alignment procedure begins by removing the input coupler (M2) and maximising the single-pass SHG efficiency. This step optimises the beam waist and orientation of the input mode relative to the crystal. The cavity mirrors are then aligned such that the transmitted and retro-reflected beams overlap precisely, ensuring that successive round trips retrace the same optical path. When correctly aligned and the input coupler is replaced, the cavity exhibits visible 'flashes' of green light as it momentarily resonates with the input field.

Once coarse alignment is achieved, the piezo-mounted mirror (M1) is driven with a small triangular ramp voltage to scan the cavity length. The transmitted and reflected powers, monitored with photodiodes, display a series of resonant peaks corresponding to cavity modes. Fine adjustments to mirror positions and input collimation are made to maximise transmission through resonance. The cavity is then actively locked to a transmission peak using a feedback loop that stabilises the piezo voltage, maintaining resonance and ensuring stable, high-power SHG output. In 3.5, we detail the method used to stabilise the cavity to peak power.

We obtain approximately 80 mW of 520 nm light for around 1 W of input within the doubling cavity which decreases to approximately 20 mW at 515 nm. Although this represents a successful frequency-doubling configuration, the conversion efficiency is lower than that achieved in comparable systems at 509 nm [88]. The reduced performance is most likely attributed to limitations in the tapered amplifier (TA) used to boost the fundamental light. Specifically, the TA's gain spectrum is rated for operation around 1040–1060 nm, whereas our system operates closer to 1030–1040 nm. At these shorter wavelengths, the available gain decreases signific-

antly, and the amplifier exhibits increased amplified spontaneous emission (ASE) outside the desired mode. This results in less effective amplification of the seed light and consequently lower intra-cavity power at the fundamental wavelength, reducing the overall SHG output.

3.4 Radio Frequency Equipment

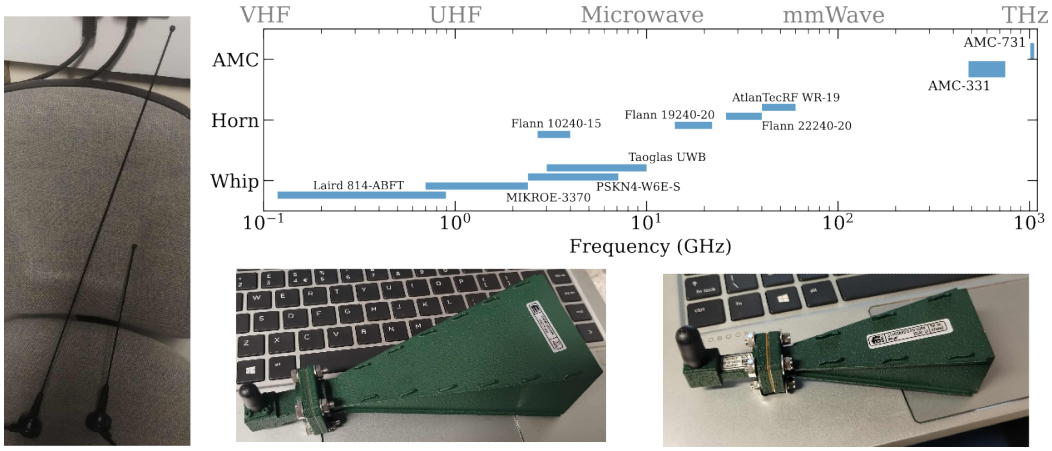

Figure 3.3: *Top Right:* A plot showing the various radio-frequency equipment used in this thesis and the available frequency span of each component. These approximate frequency ranges of the antennas are shown along with the product names for reference. *Left and Below:* Reference images of the antennas used. Two *Laird 814-ABFT* monopole whip antennas tuned for $\approx 140\,\mathrm{MHz}$ and $\approx 300\,\mathrm{MHz}$, and the *Flann Microwave Ltd.* 19240-20 and 22400-20 horn antennas (left to right).

In this section, we describe the equipment used to coherently generate and deliver rf and microwave radiation* for the experiments presented in this thesis. The radio spectrum, and those accessible via Rydberg transitions, spans many orders of magnitude in frequency, and no single source can cover its full range with sufficient power, and tunability. Consequently, a combination of rf instruments is employed, each for a particular frequency band. The accessible frequency range of these sources directly determines which transitions between Rydberg states can be driven, and therefore influences both the atomic states that can be reached and the types of spectroscopy and sensing experiments that can be performed. These frequency

*The terms *rf* and *microwave* are used interchangeably throughout the thesis. However, we often use microwave to refer to the higher-frequency portions of whole radio spectrum.

sources were selected based on the Rydberg states accessible via the coupling laser we previously built, which in turn determine the adjacent states that can be resonantly coupled and the corresponding rf transition frequencies.

3.4.1 Microwave Sources and Antennas

The microwave radiation used to coherently couple Rydberg states in this work is generated and emitted using a series of whip and horn antennas that span a wide range of frequencies, as shown in Fig. 3.3. These antennas cover the regime from the very high frequency (VHF) region through to the extremely high frequency or millimetre-wave region, enabling coupling between Rydberg states separated by transitions from a few hundred megahertz up to tens of gigahertz.

For the generation of single-frequency microwave tones, we employ multiple *WindFreak SynthHD Pro* signal generators. These sources provide tunable outputs over the 0.1–24 GHz range, are compact and able to operate two tones simultaneously. The generated signals are fed into the appropriate antenna depending on the target transition frequency. For frequencies above 24 GHz, we use an *Anritsu* MG3696A signal generator, capable of continuous-wave output up to 65 GHz. The highest microwave frequency employed in this work is 50.6 GHz. The next highest frequency we employ is 480 GHz, in which the system enters the terahertz (THz) regime discussed below.

3.4.2 Terahertz Sources

The THz radiation used in this thesis is produced using commercial amplifier-multiplier chain (AMC) modules from Virginia Diodes Inc. (VDI). These devices take a microwave seed tone, typically in the 10–15 GHz range, and generate harmonics through successive frequency multiplication stages, yielding a THz output. The seed frequencies are produced using the aforementioned *WindFreak* generators, which are fed into the AMC.

Two AMCs were employed throughout this work:

- **AMC-331:** A widely tunable, low-power THz source covering 475–750 GHz. This source was used for most experiments, including the rf-sensing measurements in chapter 4 and the spectroscopic studies in chapters 5 and 6. The available power ranges from approximately 50 µW at its peak near 600 GHz to around 1 µW at the extremes of its tuning range.
- **AMC-731:** A higher-power ($\sim$ 400 µW) source covering $\approx$ 1.01–1.08 THz. This was employed for specific high-frequency transitions requiring greater coupling strength, as detailed in chapters 5 and 6.

The emitted power of the THz source can be controlled via a user-controlled attenuator (UCA) which allows a voltage controlled attenuation of the output, this was programmed as needed using a National Instruments Digital I/O programmed using `pyVISA`. The THz radiation is emitted from standard waveguide horn antennas (WR1.5/1), and collimated using polytetrafluoroethylene (PTFE) lenses to form a near-Gaussian beam. The linear polarisation of the emitted field is defined by the orientation of the horn aperture.

3.5 Laser Frequency Stabilisation

In this section we go over the various instruments and methods used in stabilising lasers. Lasers are inherently sensitive to fluctuations in temperature, current, and mechanical alignment (through vibrations), all of which can cause the output frequency to drift over time or fluctuate rapidly. Frequency drift must be suppressed so that the laser remains resonant with a stable optical reference. This is achieved through active feedback control, where a portion of the optical signal is monitored to generate an error signal that represents how far the system is from its resonance or target condition.

A proportional–integral–derivative (PID) controller is the standard feedback mechanism used to stabilise such systems. It continuously compares the measured error signal with a setpoint (the desired value) and applies a corrective response to minimise the difference. The proportional term reacts to the instantaneous error, providing fast correction, the integral term compensates for steady-state offsets by accumulating the error over time, and the derivative term anticipates future changes based on the rate of error variation, improving stability and damping oscillations.

In the context of laser frequency stabilisation, a PID loop can act on either the laser frequency (by adjusting the grating or current) or the cavity length (by adjusting a piezo-mounted mirror).

3.5.1 Probe Laser Polarisation Spectroscopy

In all of the experimental work presented in this thesis, the probe laser is frequency-stabilised ('locked') using polarisation spectroscopy on the caesium $6s_{1/2}, F = 4 \rightarrow 6p_{3/2}, F' = 5$ transition. The technique, described in detail by Pearman *et al.* [89], provides a method of generating an error signal suitable for laser frequency locking. In this scheme, optical pumping by a circularly polarised pump beam creates an anisotropic population distribution among the ground-state hyperfine sublevels, resulting in circular birefringence and dichroism in the atomic vapour. A weak, linearly polarised probe beam experiences a differential phase shift between its left- and right-circularly polarised components as it passes through the medium. When analysed with a polarising beam splitter (PBS) and balanced photodetector, these differential phase shifts result in intensity changes in the two orthogonal linear components, producing a dispersive error signal centred on the atomic resonance. The probe laser includes integrated locking electronics that enable direct current control using the generated error signal.

3.5.2 Coupling Laser

3.5.2.1 Cavity Lock

As described in section 3.3.2.3, resonant enhancement of the fundamental field within the bow-tie cavity is needed for efficient generation of 515–520 nm light. To maintain resonance, the cavity length is actively stabilised using the Hänsch–Couillaud (HC) method [90], which generates a dispersive error signal from polarisation changes in the reflected light. The technique provides a modulation-free alternative to other stabilisation schemes such as Pound–Drever–Hall (PDH) locking [91]. The resulting error signal is processed and stabilised via a digital PID feedback loop implemented on a STEMlab Red Pitaya control board [92] or using a *Moku:Go*, a lab multi-instrument which includes PID control loops. In the HC method, the input beam, composed of two orthogonal linear polarisations, is converted to an elliptical polarisation by an intracavity element that introduces polarisation-dependent loss or phase shift. In our setup, the non-linear crystal itself provides this birefringent behaviour. The reflected beam from the input coupler (M2) is directed through a quarter-wave plate that converts the circularly polarised components into orthogonal linear polarisations. A polarising beam splitter (PBS) separates these components, which are detected on two photodiodes. Their difference forms the error signal, which changes sign as the cavity crosses resonance. The dependence of this signal on cavity detuning can be expressed as:

$$I = 2I_0 \cos(\theta)\sin(\theta)\frac{T_{\text{in}}\mathcal{R}\sin(\phi)}{(1-\mathcal{R})^2 + 4\mathcal{R}\sin^2(\frac{1}{2}\phi)}, \tag{3.4}$$

where θ is the angle of the half-wave plate before the cavity, T_{in} is the input coupler transmission, ϕ is the phase difference between the two waves, and $\mathcal{R}$ is the effective round-trip reflectivity. Setting $\theta = \pi/4$ maximises the error signal, though in practice this is reduced to 1–2 ° to maintain sufficient power along the primary polarisation for efficient frequency doubling.

The PPSLT crystal introduces additional birefringence, leading to polarisation-

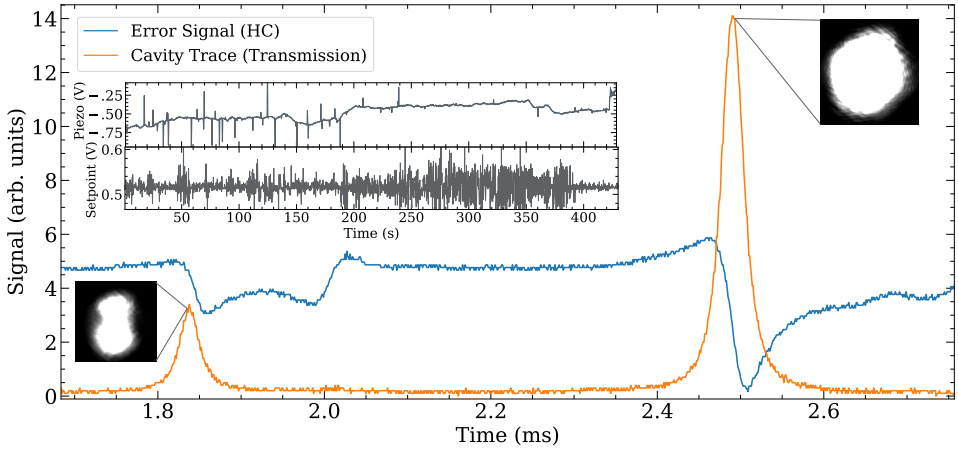

Figure 3.4: Typical error signal (blue) used for cavity locking when the cavity is roughly aligned, overlaid with the corresponding cavity transmission spectrum (orange). The primary large zero-crossing, corresponding the largest production of green light, is the TEM_{00} (pictured top right) extraordinary-polarised mode, while the smaller adjacent feature arises from the lower-amplitude TEM_{01} mode (pictured bottom left). The crossing associated with the ordinary-polarised wave is also visible for this mode in the error signal (middle blue feature) but not in the transmission profile (as no green light is generated!). The TEM_{01} mode is suppressed and the TEM_{00} mode is enhanced as the cavity is better aligned. Inset: Piezo offset signal supplied by the *Red Pitaya* (RP) during lock operation, together with the PID set-point over several minutes, illustrating stable feedback performance.

dependent refractive indices for the ordinary and extraordinary components [93]. This results in two distinct error-signal zero crossings corresponding to the two cavity resonances, as shown in Fig. 3.4. Each crossing has an opposite slope, allowing the PID controller to distinguish between them by inverting the sign of the proportional, integral, and derivative constants. Temperature drift can modify the birefringence, shifting the separation between the crossings and occasionally causing overlap, leading to unstable locking conditions. To mitigate this, temperature stability of the cavity mount is maintained, and in some systems an additional intracavity wave plate can be used to control birefringence [93], though this was not required in our implementation.

The error signal, generated from the cavity pick-off optics shown in Fig. 3.2, is fed into the Red Pitaya (and later a *Moku:Go*), which performs analogue-to-digital conversion (ADC), applies a digital PID algorithm, and outputs a correction

voltage via its DAC to the piezo-mounted cavity mirror (M1). Although the ±1 V input/output range limits the dynamic locking range we use an additional voltage amplifier which provides sufficient long-term stability for our application. Fig. 3.4 shows a typical locking signal overlaid with the cavity transmission spectrum, as well as the PID output behaviour over several minutes.

3.5.2.2 Excited State Lock

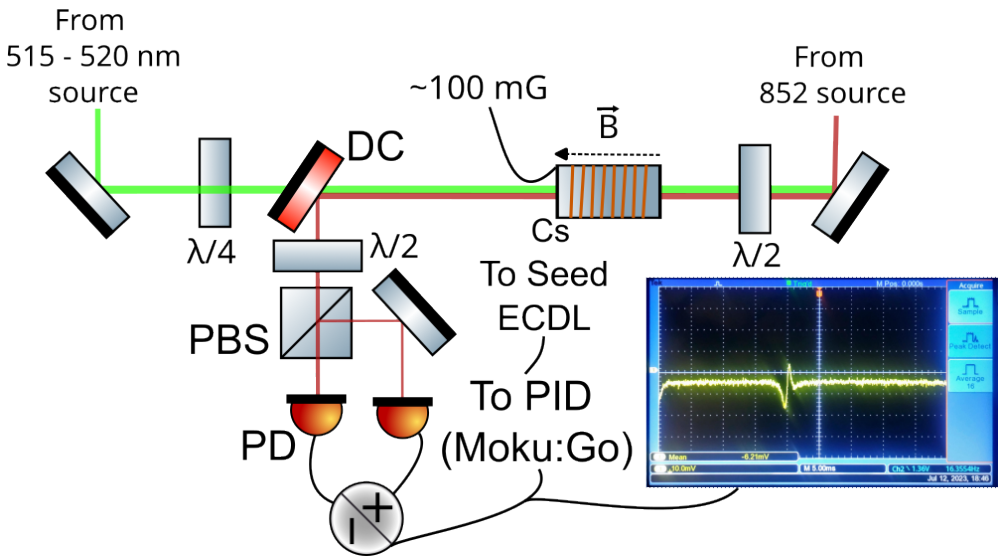

Figure 3.5: Experimental diagram showing the layout to produce an excited state signal for the coupling laser frequency stabilisation. A circularly polarised coupling laser propagates against a linearly polarised probe beam inside a Cs vapour cell where a magnetic field is aligned along the probe beam direction. A PBS then separates the two orthogonal components of the polarised probe beam. The difference signal between the two signals then produces a dispersive error signal on resonance of the Rydberg state shown in the bottom right of the diagram. The signal is processed by a *Moku:Go* which feedbacks to the coupling seed laser.

For the coupling laser, the cavity lock maintains constant intra-cavity power and thereby stabilises the frequency-doubling efficiency, an additional feedback loop is required to stabilise the wavelength of the external-cavity diode laser (ECDL) itself. This is achieved by controlling the grating actuator of the ECDL using a separate electronic feedback loop, as described below.

To generate the necessary error signal, a nonlinear polarisation spectroscopy tech-

nique is employed [94]. In this scheme, small fractions of the probe and coupling laser beams are diverted from the main optical path to form an auxiliary Rydberg EIT setup within a vapour cell. The principle is similar to the ground-state polarisation spectroscopy used to stabilise the probe laser: optical pumping creates an anisotropic (birefringent) medium, which rotates the polarisation of the probe beam as a function of laser detuning.

A small magnetic field is applied along the propagation direction, lifting the degeneracy between the $m_F = \pm F$ Zeeman sublevels. This introduces a frequency-dependent birefringence that produces a dispersive, zero-crossing signal at line centre. When the coupling laser polarisation is made slightly elliptical, achieved by adjustment of a quarter-wave plate, the two circular components of the coupling field contribute unequally to the interaction, resulting in a well-defined, dispersive error signal.

The experimental arrangement used to realise this lock is shown schematically in Fig. 3.5. After transmission through the vapour cell, the probe beam is analysed by a polarising beam splitter that separates the orthogonal linear polarisation components. The difference between the two resulting photodiode signals yields the error signal, which is fed back to the ECDL grating actuator to stabilise its wavelength. Here, a *Moku:Go* is used as the control electronics and PID loop for the system. This non-linear polarisation spectroscopy lock provides long-term frequency stability of the coupling laser while preserving the efficiency of the SHG cavity lock.

3.6 Experimental Configurations

3.6.1 Rydberg RF Electrometry

In the first experiment presented in this thesis, we explore the coherent excitation and coupling of Rydberg states in caesium atoms using a combination of optical, THz, and rf fields. A schematic of the experimental layout is shown in Fig. 3.6. The purpose of this experiment is to demonstrate how multiple Rydberg states

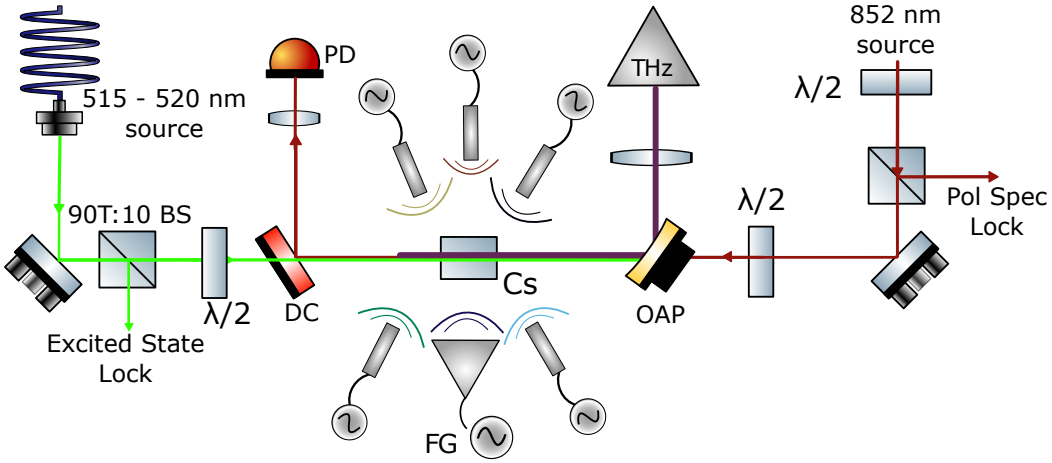

Figure 3.6: General experimental layout for the Rydberg EIT rf sensing. The coupling laser is launched from a fibre, where it has been fibre coupled from a separate optical table. It is split by a 90T:10R non-polarising beam splitter whereby it counter-propagates against the 852 nm probe laser within the Cs vapour cell. The resulting probe after transmission is diverted from a dichroic mirror and measured on a photodiode. An off-axis parabolic (OAP) mirror is used to reflect a coherent THz beam to the vapour cell where it has been partially collimated using a PTFE lens. Dipole whip antennas and antenna gain horns are positioned around the vapour cell whereby various microwave fields are generated, modulated and propagate to the Cs vapour cell.

can be connected in a cascade, or ladder-type, configuration to probe the atom's response across a wide range of frequencies. As we have seen, Rydberg atoms are particularly well suited to this task due to their large dipole moments and varying closely spaced energy levels.

The probe and coupling lasers are used to excite the atoms from the ground state to a chosen Rydberg state via a two-step excitation process. A linearly polarised probe laser resonant with the $6S_{1/2}, F = 4 \rightarrow 6P_{3/2}, F' = 5$ transition interacts with a room-temperature vapour of caesium contained in a 10 mm cubic glass cell. A second, counter-propagating coupling laser drives the upper transition from the $6p_{3/2}$ state to the $19d_{5/2}$ state. The probe and coupling beams have powers of 20 µW and 21 mW and $1/e^2$ beam waists of 1.20(7) mm and 0.96(7) mm respectively. Rydberg EIT then allows the probe transmission to be used to infer properties, such as the Rabi frequencies of the probe and coupling field.

Once the probe and coupling laser are both established, additional fields at THz

and rf frequencies are applied to couple neighbouring Rydberg states of increasing angular momentum. The THz field is launched from a diagonal horn antenna, collimated using a polytetrafluoroethylene (PTFE) lens and focused in the Cs cell using an off-axis parabolic (OAP) mirror. The OAP contains a 2 mm through-hole to allow the laser beams to copropagate with the THz beam and is estimated to have a power of 10 µW and beam waist of approximately 1.5 mm within the cell. The rf fields are emitted from the various horn and whip antennas detailed in the previous section and are placed approximately 10–20 cm from the cell where there is clear line-of-sight.

These transitions form a cascade of connected states, each linked by a resonant electromagnetic field, extending from the optically excited $19d_{5/2}$ state to high–ℓ states such as f, g, and beyond. The THz field couples the $19d_{5/2} \rightarrow 17f_{7/2}$ transition at 0.607 THz, while lower-frequency rf fields couple adjacent higher–ℓ states, with transition frequencies ranging from hundreds of megahertz to several gigahertz. Each additional field modifies the probe transmission spectrum, providing a direct optical signature of the underlying couplings. This approach effectively links transitions spanning optical to THz and rf frequency domains within a single atomic system.

3.6.2 Rydberg High Angular Momentum Spectroscopy

In chapters 5 and 6, Rydberg EIT is used to investigate the response of the thermal caesium vapour to applied THz and microwave fields. By monitoring changes in the probe laser transmission as these fields are applied, the frequency of the THz or microwave radiation can be precisely determined, enabling accurate measurement of atomic transition frequencies. A schematic of the experimental layout is shown in Fig. 3.7.

Two excitation schemes are employed to access different Rydberg manifolds in Cs: a two-photon ladder scheme for excitation to nd_j states and a three-photon

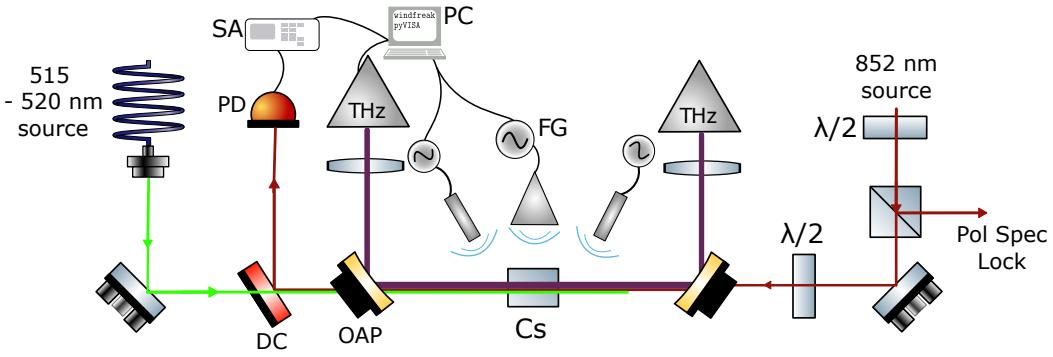

Figure 3.7: General experimental layout for the Rydberg high ℓ spectroscopy. The green Rydberg laser is launched from a fibre and passes through a dichroic. As in the sensing experiment, it counter-propagates against the 852 nm probe laser within the Cs vapour cell. The resulting probe after transmission is diverted from a dichroic mirror and measured on a photodiode. Depending on the transition being measured, two off-axis parabolic (OAP) mirror reflect coherent THz beams to the vapour cell. Dipole whip antennas and antenna gain horns are positioned around the vapour cell whereby various microwave fields are generated and propagate to the Cs vapour cell. Extended experimental control of the microwave fields, DAQ from the photodiode, and the resulting signal on the oscilloscope (SA) are shown in addition. In contrast to the previous experiment, the coupling laser is scanned and does not require active frequency stabilisation.

(using an additional laser to access an intermediate state, $7s_{1/2}$, before exciting to a Rydberg state) ladder scheme for access to Rydberg np_j states. The present work focuses on the two-photon excitation scheme, while the data from the three-photon configuration collected by Downes [80] is used for additional data analysis in Chapter 5. In the two-photon scheme, the counter-propagating Rydberg laser drives the $6p_{3/2} \rightarrow nd_j$ transitions. The laser powers are typically 10–20 mW, with similar beam waists to those used in previous sections. To improve atomic transmission and enhance the observed EIT contrast, the vapour cell is occasionally heated to 40–60 °C using a ceramic heater placed within the vapour cell's mount (*Thorlabs* HT24S), increasing the number density and resultant optical depth. The THz radiation is emitted and used similarly to the previous section. However, in contrast to the previous experiment, both THz AMC sources are used, covering different frequency ranges which define the accessible set of adjacent Rydberg transitions. In this configuration, the applied THz field couples the excited nd_j state to neighbouring nf_j states. Additional microwave or THz fields can be applied to further couple to

higher-ℓ states (g, h, etc.), with horn antennas used for frequencies above 20 GHz and whip antennas for frequencies below 10 GHz. These microwave fields, typically $\sim$10 µW within the cell, are applied perpendicular to the propagation direction of the optical and THz beams. In the absence of applied electromagnetic fields, the transmitted probe signal exhibits a single Lorentzian EIT resonance as the Rydberg laser is scanned. Although the experiment is performed in a thermal vapour, where optical transitions are typically Doppler broadened and therefore Gaussian, the EIT resonance itself is dominated by homogeneous broadening mechanisms (natural linewidth, transit-time, power broadening, dephasing). In particular, for near counter-propagating probe and coupling beams, the two-photon resonance condition is largely insensitive to atomic velocity, leading to a significant suppression of Doppler broadening. In contrast, a Gaussian lineshape would arise if Doppler broadening dominated, for example in the absence of Doppler cancellation or for single-photon absorption resonances. The EIT lineshape can display enhanced absorption just below and above the two–photon resonance [26, 95]. However, this only occurs for a much weaker probe power not used in throughout this work.

When additional THz or microwave fields are present, this resonance splits or shifts depending on the detuning of the field. By examining the observed lineshapes, the transition frequencies can be extracted with sub-megahertz precision.

3.7 Optical Readout and Data Acquisition

As in Rydberg EIT experiments, the transmission of the atomic vapour is modified by the presence of external electromagnetic fields. The transmitted optical power of the probe laser once it has passed through the vapour is detected by a photodiode (*Hamamastu* APD C5460) that produces a voltage proportional to the incident probe power. To quantitatively relate this voltage to the optical transmission of the vapour, several calibration and data-handling steps are required so that the recorded signal can be interpreted in physical units and analysed computationally.

3.7.1 Calibration

In both experimental configurations presented in this thesis, the coupling laser frequency is scanned across an atomic resonance while the probe laser remains fixed. The photodiode voltage therefore varies as a function of time according to the detuning of the coupling laser, producing a characteristic transmission profile or 'scan' on the oscilloscope.

Because the oscilloscope records voltage, calibration measurements must be performed before each data set to relate the voltage to the transmitted optical power. With the probe laser locked, the probe power is measured both before and after the vapour cell. The ratio of these powers provides the absolute transmission of the probe transition and a scaling factor, P_{p}/V, that is used to convert photodiode voltage to optical power. This calibration must be repeated whenever the probe power, beam waist, or cell temperature is changed, as these parameters influence the transmission through the vapour.

With the coupling laser scanned and the probe laser locked, the Doppler-broadened background is effectively removed, simplifying the spectrum but eliminating a straightforward reference (The Doppler broadened width) for the frequency axis. The laser frequency detuning (x-axis) calibration is therefore obtained by referencing the known hyperfine splitting between the $F' = 4$ and $F' = 5$ states of the $6p_{3/2}$ manifold, 251.00(2) MHz [78] modified by a Doppler factor $(\lambda_p/\lambda_c - 1)$ [26]. When the frequency scan range of the coupling laser is sufficiently large, two EIT peaks are visible corresponding to transitions from the $6p_{3/2}$, $F' = 4$ and $F' = 5$ hyperfine states to the excited state and their 'time' separation on the oscilloscope trace provides a conversion factor between time and frequency detuning (MHz/t) i.e., some 'scan rate'. For scans of a smaller detuning range, this factor can be reused provided that the laser scan rate remains constant. While more rigorous methods exist for accurately determining the frequency axis [96], such precision is not required here, and this calibration is used here only to provide a sense of the frequency

range, as the results presented throughout this thesis do not explicitly depend on an absolute or relative frequency scale.

3.7.2 Data Acquisition and Automation

Oscilloscope traces are transferred to a control computer via the `pyVISA` Python package [97], which provides a standard interface for communicating with laboratory instruments using the Virtual Instrument Software Architecture (VISA) protocol. The acquired data are then processed and analysed using custom Python routines for baseline correction, fitting, and frequency calibration.

Automation is an essential part of the data collection process, particularly for spectroscopy measurements that require the acquisition of hundreds of transmission profiles at different rf frequencies or powers. To facilitate this, we employ the `windfreak` Python package, which provides USB control of the Windfreak *SynthHD* signal generators [98]. This allows programmable adjustment of the rf frequency and output power, during long data acquisition sequences. The *Anritsu* frequency generator had to be manually adjusted for each data acquisition.

3.8 Conclusion

In summary, this chapter has detailed the construction and stabilisation of the laser systems and optical components used to generate and manipulate coherent light fields for Rydberg excitation in thermal caesium vapour. The development of a stable SHG system provided access to the 515–520 nm wavelength range, used for coupling to higher-lying electronic states. Frequency stabilisation of both the probe and coupling lasers was achieved through polarisation spectroscopy, while the doubling cavity was locked using a Hänsch–Couillaud method implemented with a digital PID controller. Together, these systems provide long-term frequency stability required for the spectroscopy and sensing using multiple Rydberg states.

These setups form the experimental foundation for the measurements and results presented in the following chapters, where these laser systems are applied to explore couplings between Rydberg states, THz and microwave sensing, and multi-level ladder schemes in atomic vapour.

Chapter 4

Radio Frequency Sensing Using High-Angular-Momentum States

> The work presented in this chapter is based on material published in [1].

In the previous chapters we developed the theoretical background and experimental tools needed to produce and detect Rydberg states in caesium. In this chapter, we present a novel excitation scheme to access and coherently detect a wide range of Rydberg states by using multiple rf fields, along with the optical fields, applied simultaneously. In addition to a probe and coupling laser used to prepare the Rydberg state, additional coherent rf fields are applied concurrently, each resonantly coupling the next-highest angular momentum ($\ell \to \ell + 1$) state. As the ℓ values increase, the energy spacing between adjacent states decreases, allowing access to an extremely broad range of radio frequencies within a single atomic ensemble.

4.1 Introduction

A key feature of this scheme is that it enables continuous, non-destructive optical readout of these high–ℓ states through the probe transmission. Traditionally, spectroscopy of such states has relied on field-ionisation techniques [99, 100, 101], which are inherently destructive and provide only static information about the energy levels. In contrast, the method presented here allows real-time observation of coherent dynamics and rf-induced couplings through electromagnetically induced transparency (EIT), opening the way to both sensitive rf detection and high-resolution spectroscopy of high–ℓ Rydberg manifolds.

We show that the optical response of the multi-level rf-driven system can be accurately reproduced using a Lindblad-master-equation model and demonstrate experimentally that a series of amplitude-modulated rf tones can be detected *simultaneously* using a common optical readout. This approach allows a Rydberg receiver to detect signals across multiple frequency bands, from the very high frequency (VHF) to the terahertz (THz) range, using a single optical detection channel. In addition to its technological relevance for broadband quantum sensors, this method also provides a new tool for high-resolution spectroscopy of high–ℓ Rydberg states, which are otherwise difficult to access experimentally.

4.2 Overview

One of the major advantages of Rydberg-atom rf receivers, when compared to traditional antenna-based rf technologies, is its potential to detect electromagnetic fields across an enormous frequency range using a single device [77]. Indeed, Rydberg-atom receivers have demonstrated rf field detection at frequencies across 12 orders of magnitude, from below 1 kHz [102] to above 1 THz [103].

The low-frequency* end of the radio spectrum can be accessed using an off resonant detection method (quasi-DC), making continuous frequency coverage possible [27, 77, 104]. However, sensitivity is typically lower as it relies on a different mechanism (the polarisability of the states). In contrast, in the resonant ac regime, where transitions between Rydberg states are driven close to resonance, much higher sensitivity is achievable [29, 105], but only within narrow frequency windows defined by those transitions.

The resonant frequency between adjacent Rydberg levels decreases as the principal quantum number n increases, approximately scaling as n^{-3} [18]. Consequently, accessing lower-frequency transitions (e.g., below 4 GHz) requires very high-n states ($n > 100$). However, such states present experimental challenges:

- The dipole matrix element between the ground and Rydberg state scales as $n^{-3/2}$, meaning the required laser power increases with n for a given Rabi frequency, putting larger demands on the laser.
- High-n states suffer from strong Rydberg–Rydberg interactions, DC Stark shifts, and ionisation, which degrade measurement accuracy [26].

Much of the electromagnetic spectrum used for practical communication and sensing, including maritime, navigation, and radar bands below 2 GHz remains outside the range of conventional Rydberg receivers [106]. To date, Rydberg sensors have demonstrated their highest sensitivities in the microwave regime around 10 GHz [32], but extending their operation to lower-frequency bands is highly desirable. Unlike conventional antennas, Rydberg receivers are not constrained by the limitations that apply to so-called electrically-small antennas, where the physical size of the antenna (or in this case, the atomic vapour volume within the excitation lasers) is much smaller than the wavelength of the detected field [107, 108]. In traditional systems, this size restriction sets fundamental limits on sensitivity, bandwidth

*'low-frequency' for Rydberg atoms (< 2 GHz) is very different to low frequency in traditional rf technologies (<1 MHz!) owing to the way in which energy levels are spaced in typically used states ($n = 30$–80 and $\ell \leq 3$) as shown in Fig. 2.3.

and data capacity [109, 110]. These limits arise from thermal noise within the detection electronics and from the Chu limit, where the latter restricts the bandwidth and data capacity of electrically small antennas by relating them to the stored reactive energy in the near field [111]. Rydberg sensors, by contrast, are not bound by the Chu limit, since they do not rely on resonant current distributions in a conductive structure [109, 110]. Instead, their ultimate sensitivity is governed by quantum projection noise of the atomic ensemble, allowing for potentially much lower fundamental noise floors. Further discussion of sensitivity in comparison to traditional antennas is given in chapter 7.

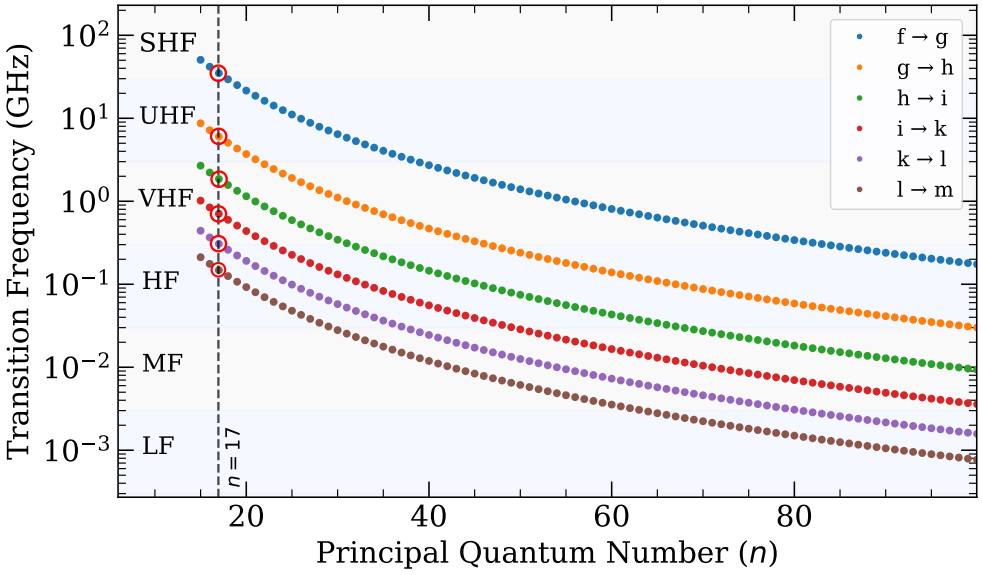

Figure 4.1: A plot of transition frequencies of the form $n\ell \rightarrow n(\ell + 1)$ showing the lower frequency regions accessed by going to higher angular momentum states. Overlay regions showing the IEEE spectrum [112] with $n = 15$–100. The transitions used for the excitation scheme demonstrated in this chapter are are circled in red for reference.

To reach lower resonant frequencies for sensing, recent work has focused on exploiting higher angular momentum (ℓ) states to reach lower-frequency transitions without resorting to extremely high n or other non-resonant (less sensitive) methods. The energy spacing between states of the same n but successive ℓ values scales approximately as ℓ^{-5} compared to n^{-3} with increasing n [18], allowing access to rf

and microwave transitions at more experimentally manageable n. For reference and interest, the transition frequencies between successive ℓ states are shown in Fig. 4.1 for a range of principal quantum numbers.

Recent work includes a three-step laser excitation schemes [113] combined with an rf coupling can drive $nf \to n'g$ ($\ell = 3 \to 4$) transitions, extending sensitivity to the $\simeq 0.5$–$3\,\mathrm{GHz}$ range for $n \approx 40$–70 [114]. Similarly, two rf couplings can be used to access $nf \to n'g$ transitions, where one is used as an auxiliary rf field to first couple to $nd \to nf$ states allowing access to higher ℓ states. This has been demonstrated for satellite signal detection near $2.3\,\mathrm{GHz}$ [115]. More recently, multi-frequency excitation schemes have demonstrated simultaneous demodulation across frequencies from 1.7–$116\,\mathrm{GHz}$ using adjacent $nd \to n'p$ and $nf \to n'd$ transitions in varying $\Delta n = |n - n'|$ [70]. Also worth mentioning is a recent proposal for dc electric field sensing which uses spectroscopy of states up to $\ell = 6$ in Rb [116].

In this chapter, we extend these approaches substantially. We demonstrate that a Rydberg ensemble can support simultaneous coupling via multiple rf fields (seven in our implementation) each connecting adjacent ℓ states in a ladder-like structure. The resulting transitions span from the very high frequency range (30–$300\,\mathrm{MHz}$) to the THz (0.3–$3\,\mathrm{THz}$) regime, corresponding to more than twelve frequency octaves*. Due to the limited bandwidth intrinsic to the atomic state, the frequency coverage is not continuous, and instead acts a set of discrete narrow ‘windows‘, analogous to, say, an array of narrowband antennas.

At accessible frequencies, we additionally show that amplitude-modulated tones imposed on each rf field can be independently detected and demodulated through the optical probe transmission, enabling simultaneous multi-band communication at each ‘carrier’ frequency using a single atomic receiver. Finally, this same scheme provides high-resolution access to high–ℓ Rydberg states, offering a new platform for precision spectroscopy of, otherwise, difficult to reach states. This is explored

*One could insincerely regard the probe and coupling lasers as further ‘frequencies’ being detected by the Rydberg ensemble. However, the point is that the enhanced sensitivity arises from the large dipole moments at high n, which is ultimately what enables sensitive detection.

in subsequent chapters. By utilising resonant transitions at significantly lower-frequency radio bands, we extend the resonant methods of Rydberg rf sensing to frequencies around 100 MHz, and potentially much lower at higher principal quantum number.

4.3 Multi-level EIT Cascade Scheme

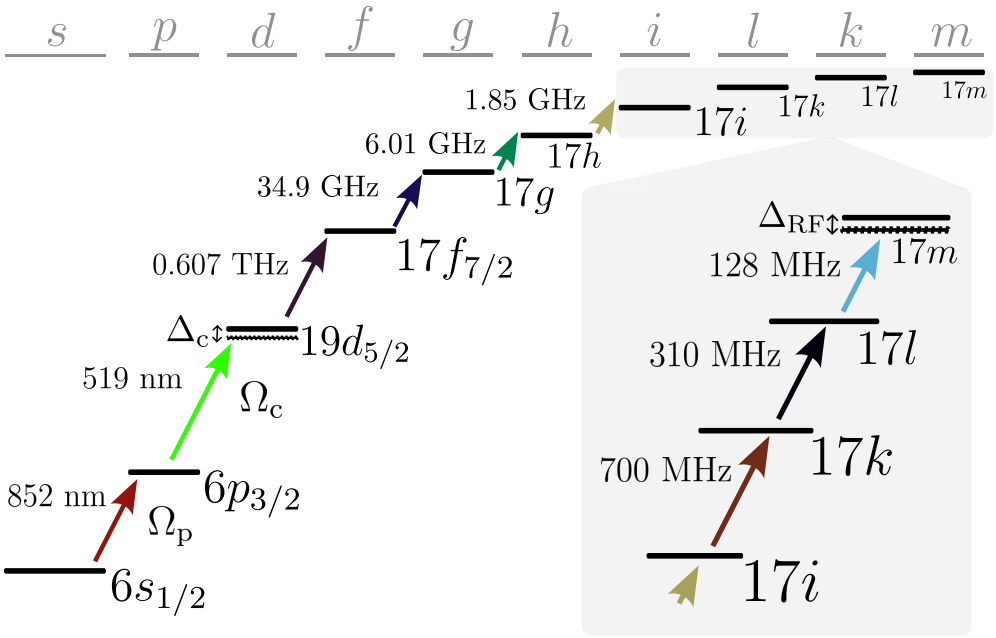

Figure 4.2: An energy-level diagram showing the electronic states used and the couplings from the various rf fields used where Ω_p is the probe Rabi frequency and Ω_c is the coupling Rabi frequency with detuning, Δ_c. A zoomed inset shows the 17ℓ states with $\ell \geq 6$ for clarity. Transitions are colour-coded to their counterpart in Fig 4.5 and display the frequency of the rf field used.

The excitation scheme used is shown in Fig. 4.2. The resulting experimental spectra, shown in Fig 4.3 can be understood in terms of a N-level EIT cascade scheme [117]. With the probe laser locked, a transparency window in the probe absorption profile is expected around $\Delta_c = 0$, resulting in a coherent EIT transmission feature as the coupling laser is detuned across this resonance. Applying the THz field results in a reduction in transmission of the probe field at $\Delta_c = 0$. For large THz field strengths, this results in the Autler-Townes (AT) splitting seen prominently in

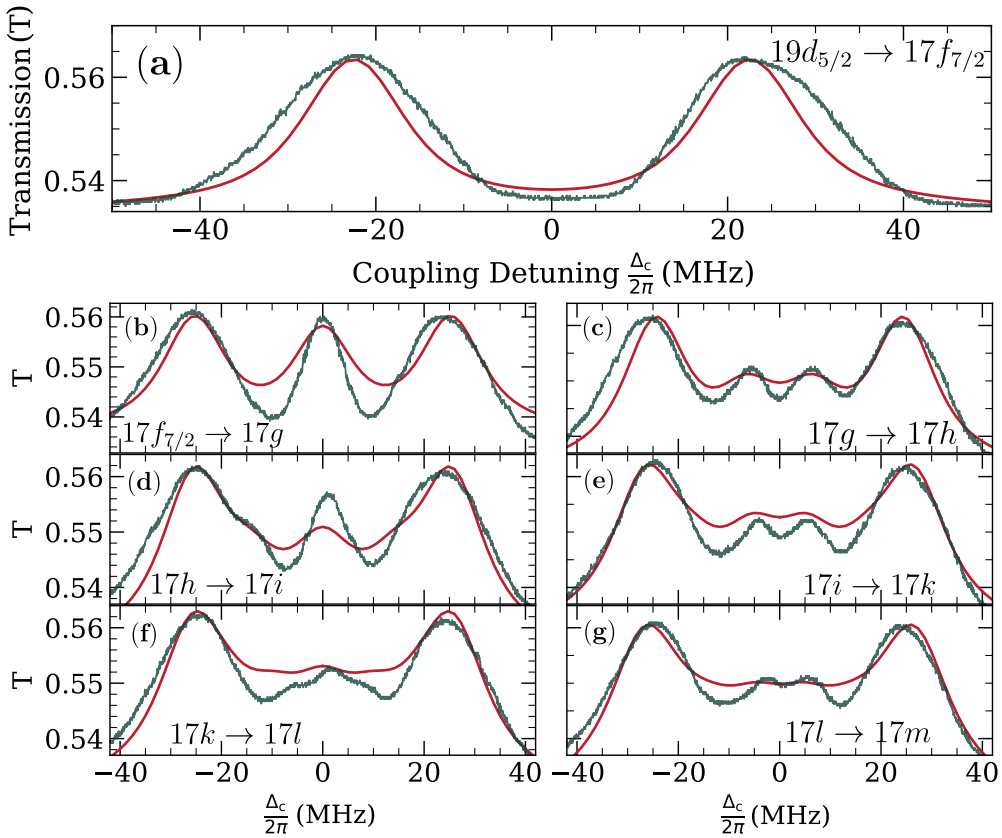

Figure 4.3: Absolute probe transmission traces from the experiment (green) with each subsequent addition of a field in the ladder system overlaid with an n-level master equation model (red). The frequency scale is calibrated via the $6P_{3/2}$, $F = 4 \leftrightarrow F = 5$ separation. (a) The probe and coupling field on with the THz field resonant to the $19d_{5/2} \rightarrow 17f_{7/2}$ transition. The subsequent microwave fields are then resonant with the (b) $17f_{7/2} \rightarrow 17g$ (c) $17g \rightarrow 17h$ (d) $17h \rightarrow 17i$ (e) $17i \rightarrow 17k$ (f) $17k \rightarrow 17l$ (g) and $17l \rightarrow 17m$ transitions. Each transition is labelled with the respective $\ell \rightarrow \ell'$ for clarity. Figure reproduced from [1].

Fig 4.3(a). With the addition of another field, there is again transparency in the line centre. This is apparent in the data in the left-hand column of Fig 4.3, showing the distinct increase in the probe transmission at zero detuning of the coupling field for an odd number of levels. For an even number of levels, there is absorption about the line centre, shown in the right hand column of Fig 4.3. When the subsequent rf fields are applied, the previous resultant AT splitting is further shifted from the line centre and decreases in amplitude. These features become hard to distinguish in the lineshape, nevertheless modulation of these fields causes a change to the transmission of the probe beam. The atomic ensemble is modelled

using a Lindblad master equation approach we introduced in section 2.3.5, which gives a time evolution of the density matrix. The series of differential equations formed are then solved in the steady state to give the susceptibility of the atomic ensemble. In this chapter we use the modelling of reference [49] to produce the theoretical fits in Fig. 4.3. The system is repeatedly solved for varying velocity classes and integrated over a bounded velocity distribution to obtain the Doppler broadened profile, as in (2.40). Minimisation of numerical solutions, to best fit the data, inclusive of Doppler broadening is computationally expensive. Instead, model inputs such as the Rabi frequencies for each field, were varied around the experimental values to give the best fit by eye.

Atomic transition	Final ℓ	rf (GHz)	DME (ea_0)
$19d_{5/2} \rightarrow 17f_{7/2}$	3	607	354
$17f_{7/2} \rightarrow 17g_{9/2}$	4	34.9	423
$17g_{9/2} \rightarrow 17h_{11/2}$	5	6.01	414
$17g_{11/2} \rightarrow 17i_{13/2}$	6	1.85	406
$17i_{13/2} \rightarrow 17k_{15/2}$	7	0.700	395
$17i_{15/2} \rightarrow 17l_{17/2}$	8	0.310	383
$17l_{17/2} \rightarrow 17m_{19/2}$	9	0.128	368

Table 4.1: A list of the electronic states that are coupled by the series of cascading rf fields. DME - (Radial) dipole matrix element calculated using `arc`. Whilst the fine structure splitting is not resolved beyond F, we label the strongest coupled j state for completeness. Note that by convention 'j' is omitted as the symbol for the $\ell = 7$ azimuthal quantum number.

The resulting model spectra are shown by the red lines in Fig 4.3, along with those from the experiment. Only one m_j state is used for each level; including all sub-levels would result in a model consisting of 110 levels. Fine structure beyond the f state is ignored but note that the $j = \ell + \frac{1}{2}$ states are most strongly coupled and transitions to these states are assumed in the calculation of dipole matrix elements for g, h and beyond.

While the model reproduces the overall spectral structure and level splittings, it does not fully capture the detailed experimental lineshapes or linewidths. Several effects likely contribute to these discrepancies. Firstly, the omission of magnetic sublevels neglects the distribution of ac Stark shifts experienced by different m_j

states in the strong applied fields, leading experimentally to additional inhomogeneous broadening that is absent from the model. Secondly, the applied THz field, and to a lesser extent the microwave fields, are spatially non-uniform across the vapour cell. Atoms therefore experience a distribution of field strengths, producing asymmetric broadening and distortion of the observed spectral features [118]. Finally, the model parameters, including the Rabi frequencies and homogeneous decay rates, were chosen to reproduce the qualitative behaviour of the system rather than obtained through a global fit to the experimental data. Consequently, the simulated linewidths are broader than those observed experimentally, particularly for transitions involving successively higher Rydberg states where the cumulative effect of coupling approximations becomes more significant.

We find good agreement with the model in the generality of adding additional levels. The parameters used for the model were $\Omega_{\mathrm{p}} = 2\pi \times 1.8\,\mathrm{MHz}$, $\Omega_{\mathrm{c}} = 2\pi \times 3.7\,\mathrm{MHz}$ and $\Omega_{\mathrm{THz}} = 2\pi \times 46\,\mathrm{MHz}$. The remaining Rabi frequencies of the rf fields varied by a few MHz but were approximately $2\pi \times 20\,\mathrm{MHz}$. Increasing the power of the THz field, which is limited due to technical restraints, would result in a larger transmission window and hence better estimation of the Rabi frequencies of subsequent fields without the use of a model. Each distinct splitting could be distinguished and measured directly from the experimental data.

4.4 Detuning Resonant fields

Fig. 4.4(a) shows behaviour of the lineshape in response to detuning the rf field from resonance. Here, the probe laser power ($\sim$100 μW) and the power of the rf fields are increased in order to improve signal to noise and visibility of the distinct AT splittings arising from each of the rf field couplings. The contrast is seen in Fig. 4.4(b) when compared to Fig. 4.3(e) whereby each of the distinct AT peaks are separated and can be distinguished.

The transmission window in the lineshape persists over a large detuning range,

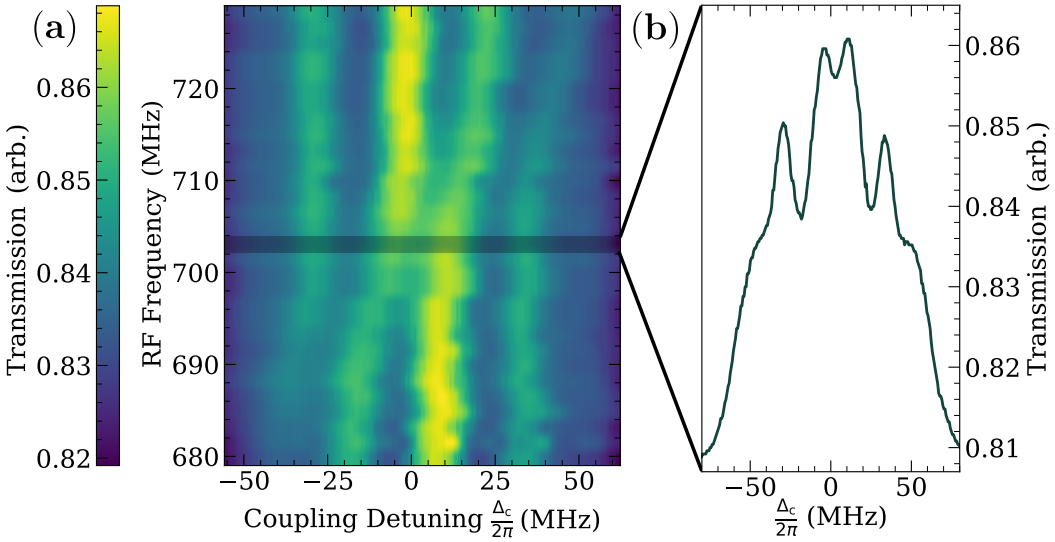

Figure 4.4: Spectral map when the $i \rightarrow k$ coupling is added and this rf field is swept and the coupling laser is detuned across resonance. (**a**) A color map made up of the resultant probe transmission traces in response to scanning the rf field over resonance for the $17i \rightarrow 17k$ transition at ∼700 MHz. As the coupling laser detuning is scanned, the system evolves through regions where different rf-coupled dressed states become resonant with the optical excitation pathway, leading to level hybridisation and the formation of avoided crossings at the distinct rf resonance conditions. The resulting level repulsion produces splittings whose magnitude is set by the effective rf Rabi frequency associated with each coupled transition. (**b**) A plot of the probe transmission against the coupling detuning for an rf field of 703 MHz — a grey bar shows the EIT trace which makes up that respective part of the color map. Figure reproduced from [1].

$\Delta_{\mathrm{rf}} = \pm 20$ MHz. As this is an even level system, the induced transparency from the presence of the previous field slowly shifts about the line centre and splits until symmetric at $\Delta_{\mathrm{rf}} = 0$ MHz. The resonance of the feature is seen at ∼705 MHz compared to the previously observed 700 MHz used in Fig 4.3(e). This can be attributed to ac Stark shifts or detunings of previous fields that accumulate error for each rf field that is on resonance.

4.5 Amplitude Modulation of RF Fields

The rf fields were amplitude modulated to demonstrate simultaneous detection across the various frequencies that are resonant with the atomic transitions. A

change in each rf field amplitude will independently change the transmission of the probe beam. When amplitude modulated, the baseband tones on each rf field can then be extracted via performing a fast Fourier transform (FFT) of the probe transmission signal. In a Rydberg atom detector, demodulation of the rf frequencies are performed by the atom in and of itself, so no additional demodulation of the signal is necessary. The signal from the photodiode then reflects the baseband signal that is transmitted along with any other instrumental noise and noise associated with the power of the probe laser. Each of the electronic states detailed above were simultaneously coupled by the probe, coupling, THz and the six rf fields with powers similar to those used in the spectra of Fig. 4.3. A baseband tone in the kHz frequency range was modulated on each carrier rf field and detailed in Fig. 4.5. The modulation index of the AM used on all of the carrier frequencies was 0.5 controlled by settings in the *Windfreak* frequency generators. The resulting modulus of the fast Fourier transform of the probe signal is shown in Fig 4.5(a).

The data show that the baseband tone from each of the independent carriers can be recovered from the probe signal. The decreasing strength of the FFT signal as the carrier frequency decreases can be partially attributed to the decreasing DME of the transitions. Additionally, the large modulation depth of each field may decrease sensitivity of subsequent states, through a change in the response of the vapour, and also from the different driving Rabi frequencies of each field.

In order to remove servo noise that we observed in the FFT, the data presented is taken by disengaging the coupling laser frequency lock and subsequently saving a trace. Due to technical limitations, the THz source and 34.9 GHz microwave generator could not be amplitude modulated. However, there is nothing to suggest that amplitude modulation of these transitions could not be detected.

Finally, to complement Fig. 4.5, a mobile phone was connected to the Windfreak signal generator, which was configured to produce a continuous-wave carrier at 700 MHz. The audio output from the phone's 3.5 mm phone connector ('audio jack') was fed into the amplitude modulation (AM) input of the generator, such that the

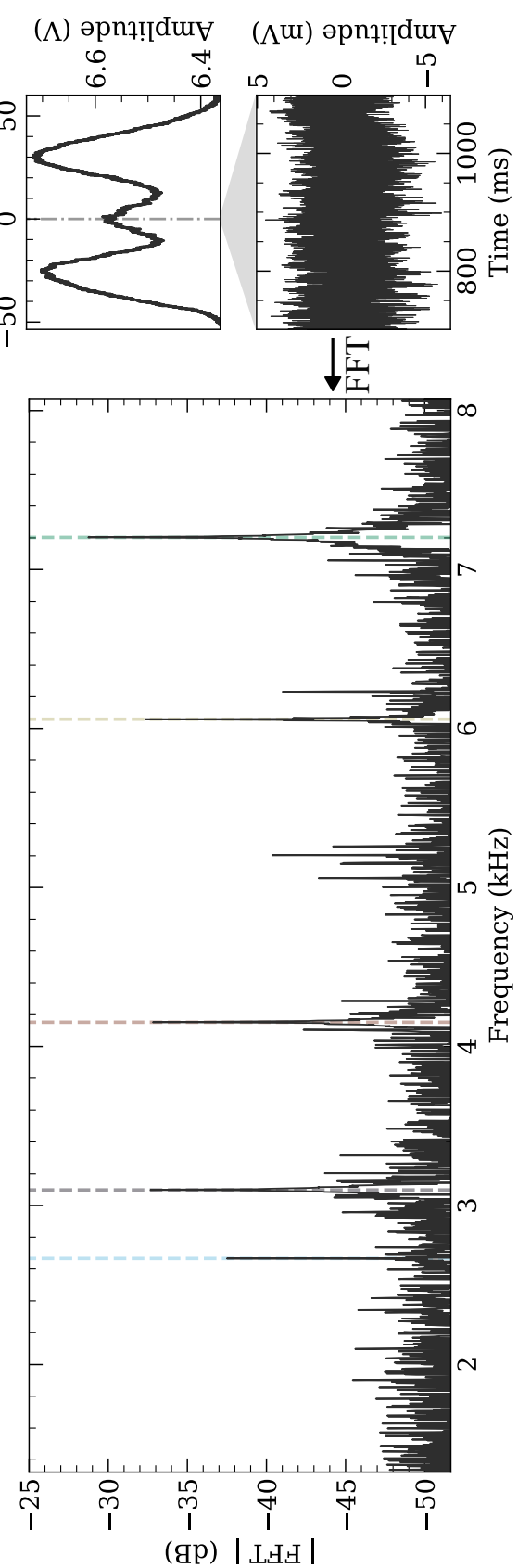

Figure 4.5: Simultaneous detection of five independent AM tones using five of the seven rf carriers by measurement of the probe laser power. (a) The modulus of an FFT of the probe transmission at $\Delta_c = 0$. The amplitude-modulated tones used were 7.2 kHz, 6.05 kHz, 4.15 kHz, 3.1 kHz, and 2.66 kHz on carrier frequencies of 6.01 GHz, 1.85 GHz, 700 MHz, 310 MHz, and 128 MHz, respectively. A dashed line is shown on each of the peaks for visual aid. The resolution bandwidth of the oscilloscope is 2.5 Hz. (b) An inset showing a typical scan of an EIT feature during modulation of the rf fields. A vertical dashed line shows the point at which the coupling laser is locked. (c) A typical photodiode trace before it is discrete Fourier transformed. Figure adapted from [1].

audio waveform acted as a modulation signal. The ensemble of atoms transduces the amplitude-modulated microwave field onto the probe laser transmission via the EIT process. The resulting optical signal, detected on a photodiode, can be directly connected to a speaker (after applying a DC block/high-pass filter) to recover the original audio – an 'atomic radio'. Representative recordings of this demonstration cannot be included in the supplementary materials due to copyright restrictions but can be obtained from the author upon request*. This is identical to previous demonstrations [119] albeit with a much lower carrier frequency allowed by the method presented in this chapter.

4.6 Discussion

In principle, the number of fields that could be applied is limited by the possible angular momentum states, $(n-1)$. At higher principal quantum number, the sensitivity to the fields would increase, and the splitting between neighbouring ℓ states would decrease. For example, neighbouring angular momentum transitions $\ell \geq 8$ at higher n (40–70) would correspond to resonant fields in the medium frequency (300 kHz–3 MHz) or high frequency (3 MHz–30 MHz) radio bands as shown in Fig. 4.1.

We note that at low n, many perturbing effects such as DC Stark induced state mixing and Rydberg-Rydberg collisions are significantly reduced [120]. Despite the lower sensitivity to external rf fields, electrometry at low principal quantum number may be more suitable for calibration of an rf field or metrology applications.

In this work, Rabi frequencies were chosen so that transition frequencies could be determined from visual inspections of the lineshape. Consequently, the rf field strengths detected throughout this manuscript are large and approximately $\simeq$9 V/m although this is not in the limit of a minimum detectable field. Generally, the Rabi

*Audio modulation sources used for this demonstration were excerpts from "Never Gonna Give You Up" by Rick Astley (link) and a fan-made Simpsons parody of "Feel Good Inc." (original by Gorillaz) created by 'NPCarlsson' (link)

frequency of an rf field can be foremost determined by measuring the resultant AT splitting [121]. Increasing the power of the THz field, which is limited due to technical restraints, would result in a larger transmission window and hence better estimation of the Rabi frequencies of subsequent fields without the use of a model. Each distinct splitting could be distinguished and measured directly from the experimental data.

A sensitivity assessment of the method to each of the applied rf fields is beyond the scope of this thesis as the sensitivity for each transition depends upon the driving strength of all previous transitions making the parameter space very large. Regardless, we note that our sensitivity could be improved using rf heterodyning techniques and lock-in detection.

Heating the cell would also improve signal to noise ratio by increasing the optical depth. We do not expect to match the sensitivity of other Rydberg microwave detectors because of the lower dipole moments of transitions at low principle quantum number. However, implementation of these techniques would allow apt comparison to an equivalent two/three-photon method measuring resonant transitions of $\simeq$ 100 MHz at $n > 100$.

Furthermore, the use of other well-characterised antennas for the lower frequency fields would allow a better estimation of the electric field strengths involved. The $\lambda/4$ monopole antennas used are not well-characterised, are omnidirectional, and have poor efficiency, resulting in significantly less power estimated from the lineshapes in comparison to that fed to the antennas.

In the following chapter, the method presented above is used to investigate higher-angular-momentum states in alkali-metals, which are not as well studied as the s, p, d and f states. There is currently no recent published work on quantum defects in Cs higher than $g_{7/2}$ known to the authors [122, 123], whilst some exists for rubidium [124, 101, 125].

At the time of this work, `arc` used an approximate method to determine the higher-

ℓ quantum defects ($\ell \geq 4$), extrapolating from the measured Cs $g_{7/2}$ quantum defect [33]. More recent versions of the package* now employ a more complete treatment based on the atomic core polarisability. The observed resonances were found to be in general agreement and were additionally compared to the scarce available literature [100]. Discrepancies on the order of several MHz are found for $\ell \geq 5$ in comparison to said literature. There is no control of stray magnetic/electric fields which may cause further splitting of the numerous m_j states. Additional discussion of using the experimental method presented for precision spectroscopy of high ℓ states is presented, along with associated systematic error, in the following chapter.

When compared to traditional rf technologies, Rydberg atomic sensors offer a fundamentally different approach to frequency detection and control. Conventional receivers rely on resonant electronic components, antennas, mixers, and oscillators whose physical dimensions and parameters constrain the accessible frequency range. Even the most agile architectures, such as frequency-hopping spread-spectrum (FHSS) systems or cognitive radios, operate over comparatively narrow bandwidths and require active tuning of electronic components to move between frequency bands [106, 126]. In contrast, Rydberg receivers are limited not by circuit bandwidth but by the accessible transitions.

The inherent spectral flexibility of the method presented suggests a novel secure communication method. In such a scheme, the optical excitation wavelength determines the initial Rydberg state, thereby defining the set of rf transitions to which the atomic ensemble is sensitive. By changing the excitation laser, the receiver can be reconfigured to detect entirely different frequency bands without any electronic retuning. One could envision some frequency-hopping protocol, in which both transmitter and receiver share a lookup table mapping optical wavelengths to Rydberg transition frequencies. Communication could then proceed

*From version 3.7.0 onward, `arc` includes an updated model that calculates the energies of these states using the atomic core polarisability, as detailed in Chapter 6. The author contributed to the implementation of this update.

by hopping between widely separated transitions, e.g. from 128 MHz to 34.9 GHz to 0.601 THz, according to a pre-agreed sequence. Unlike classical FHSS systems, where the hopping is limited by oscillator tuning speed and hardware bandwidth, such atomic-state hopping could, in principle, span many orders of magnitude in frequency, while also providing a degree of physical-layer security: an eavesdropper would not only need to detect the signal across an extremely large band but also know which Rydberg state the receiver is tuned to. In this way, Rydberg-based receivers naturally fit the bandwidth agility requirements of frequency-hopping spread-spectrum methods. While highly speculative, such an approach highlights the broader potential of Rydberg platforms than solely sensitivity metrics.

4.7 Conclusion

Simultaneous detection of rf fields across 12 octaves detected by an optical probe is demonstrated. The method opens up a new way of conducting rf electrometry using a cascade of rf fields across adjacent angular momentum coupled states which allows access to a number of lower resonant frequency states. We have furthermore demonstrated that the simultaneous amplitude modulation of several of these rf fields can be clearly resolved in the resulting EIT optical signal, offering a path to simultaneous multi-band rf communication at increasingly lower radio bands using significantly lower principal quantum numbers.

Further work should be done to characterise, optimise and generalise the technique both for higher principal quantum number and 3-photon electrometry methods so that sensitivities are on-par with current demonstrations [32]. Such a task may be impractical to perform in experiment and may lend well to experimental modelling to see the effect on bandwidth and how modulation depth of other fields affects the detection of subsequent fields in the chain.

Chapter 5

Transition Frequencies and Quantum Defects

The work presented in this chapter is based on material published in [1] and [2]. Some work, such as Fig. 5.4, Fig. 5.5, and table 5.3, were produced in collaboration with L. Downes and uses data from their thesis [80].

In the previous chapter, a novel sensing scheme was demonstrated in which a ladder of optical and rf fields was used to coherently couple a chain of Rydberg states in caesium. In this chapter, we employ the same multi-field excitation scheme to perform high-precision spectroscopy of transitions between many different Rydberg states. From these measurements, we extract the quantum defects for each ℓ_j series of the caesium atom, that is well-described by a quantum defect, via equation (2.8), by fitting to an extended Rydberg–Ritz formula.

In the following chapter, transitions involving higher ℓ states are used to extract the polarisabilities of the ionic core, providing insight into the response of the ionic

Cs core to the Rydberg (valence) electron's field. These constants allow accurate modelling of the energy spectrum in caesium at high-ℓ.

5.1 Overview

High-precision spectroscopy of atomic and molecular states is fundamental to our understanding of the structure of matter and allows us to refine fundamental theories and discover new physics [127, 128]. Detailed knowledge of the energy levels of atoms and molecules is also essential for the development of many modern atom-based quantum technologies [5, 129] with systems involving highly-excited Rydberg levels showing particular promise for quantum computing and electric-field-sensing applications [130]. Rydberg atom-based systems are increasingly being used for electric-field sensing [65], communications [131, 132] and metrology [29] applications spanning the radiofrequency [133] to terahertz range [103, 134] and often include transitions to states with high angular momentum [116, 115]. To model these systems, open-source software such as `arc` [33] are widely used for calculating the properties of alkali atoms, relying on precision measurements of constants, such as quantum defects, to calculate energy levels, in order to improve predictive accuracy. Others can calculate these properties from first principles [135] for which these experiments can then be compared to.

The most comprehensive measurements of the quantum defects in Cs were made in 1987 by Weber & Sansonetti [136]. They determined the quantum defects of the $ns_{1/2}$, $np_{1/2}$ and $nd_{5/2}$ states, and rely on fine-structure intervals measured by Goy *et al.* [137] for calculation of the $nd_{3/2}$ quantum defects, and from Sansonetti & Lorenzen [138] for calculation of the $np_{3/2}$ quantum defects. Data were also taken for the $nf_{5/2}$ and $ng_{7/2}$ states, with the latter having no other recent measurements. Recently, there have been more precise measurements of Rydberg states to determine the $nf_{5/2,7/2}$ [139] and the $ns_{1/2}$, $np_{1/2,3/2}$ and $nd_{5/2}$ quantum defects [140] by millimetre-wave spectroscopy of ultra-cold Cs [141]. However, these

measurements still rely on data from older sources, primarily [136], rather than providing an independent reference. The most recent direct measurements for the quantum defects of the $nd_{3/2}$ state in Cs was made by Lorenzen & Niemax in 1984 [142]. Consequently, there is no single independent reference for accurate values of the quantum defects for all states with $\ell \leq 4$. This situation mirrors challenges in other areas of precision spectroscopy and metrology, where reliance on a patchwork of older measurements can propagate systematic errors and obscure true uncertainties [143, 144]. Independent, internally consistent determinations, as recommended in CODATA adjustments, can establish reference values without correlations between many data sets.

In this chapter, we present values for the quantum defects for the $s_{1/2}$, p_j, d_j, f_j and g_j states of Cs, using Rydberg EIT in conjunction with THz and rf fields. Frequency intervals between Rydberg states are measured using our THz and microwave sources to couple the states using the principle of the method used in the previous chapter for the application of sensing. The results are compared to the most recent determinations of the Cs quantum defects. Finally, by using our measurements of Rydberg states with $\ell \geq 4$, accurate values of the Cs^+ dipole and quadrupole polarisabilities can be extracted which we explore further in the subsequent chapter. This enables the precise calculation of energies for states with $\ell \geq 5$.

Both analyses lead to a complete, by which we mean for *every* ℓ_j series in caesium, independent set of Cs energy levels based on the findings in the following two chapters.

5.2 Method

At the heart of our method is the use of the symmetry of the EIT lineshape to determine transition frequencies between atomic states, even in the presence of multiple additional rf fields. As discussed in the previous chapter, resonant coupling to an additional atomic state modifies the transmission through the vapour. When

the rf field is detuned from resonance, it induces an asymmetry in the lineshape, which can be systematically analysed to extract the transition frequency. Similar observations have been used in warm vapour systems [145, 146], particularly in rf sensing [147] for metrology purposes, although precision spectroscopy in these environments has been less common compared to cold atom systems. Our method leverages this lineshape asymmetry as a tool for frequency determination.

5.2.1 4-Level Scheme

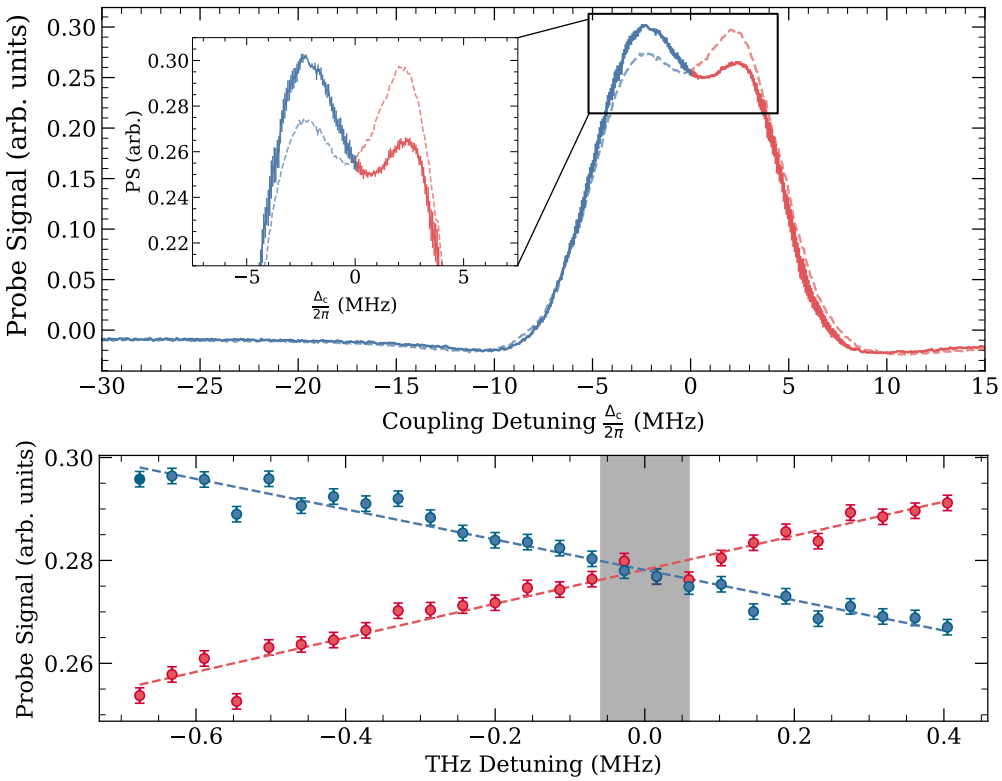

Figure 5.1: Plot showing the dependence of EIT line shape on detuning of a THz field. *Top:* Examples of the 2-photon Rydberg EIT signal with an applied THz field that is approximately 0.7 MHz below (solid line) and 0.4 MHz above (dashed line) resonance. When the THz field is resonant with the transition, we expect the height of the two Autler-Townes peaks to be equal. As the THz field is detuned, we see clear asymmetry in the peaks. *Bottom:* Height of the blue detuned (blue) and red-detuned peak (red) as a function of THz frequency - the above peaks corresponding the first and last pair of data points. By fitting straight lines to these points, we can find the resonant transition frequency as the point at which the lines intersect. In this example we measure the frequency of the $18d_{5/2} \rightarrow 16f_{7/2}$ transition to be 730.40683(6) GHz, indicated by the shaded region. Figure reproduced from [2].

The simplest case, frequently used in Rydberg sensing experiments, is a four-level system. Here, the single EIT peak generated by the probe and coupling lasers splits into two peaks when a fourth level is coupled via a resonant rf field. As shown in Fig. 5.1, detuning the rf field changes the relative amplitude of the two peaks. By measuring this amplitude asymmetry for small detunings, the rf transition frequency can be extracted [80].

In our two-photon excitation scheme, the coupling laser accesses $nd_{3/2}$ and $nd_{5/2}$ states with $n = 18$–22. THz fields then couple these to nearby $nf_{5/2}$ and $nf_{7/2}$ states, as well as a $np_{3/2}$ state, that are accessible with our AMC sources. Transmission lineshapes are recorded for each transition, Lorentzian peaks are fitted, and peak heights extracted. The measured transitions are summarised in Fig. 5.1.

We collect transmission lineshapes for each available transition with the coupling laser and fit Lorentzian distributions to the data in order to extract the peak heights. A table of all intervals measured using a 4-level scheme and those subsequently used for the data fitting (from [80]) in this chapter is given in appendix A and only the transition frequencies measured as part of this thesis are given in table 5.1.

5.2.2 N-Level Scheme

In adding additional fields, we establish the principle of extracting the transition frequencies without loss of generality. In the ladder excitation scheme, addition of an rf field resonant with an adjacent level modifies the spectrum in one of two ways.

For even numbers of levels, a strong rf field causes an Autler-Townes (AT) splitting in the lineshape, resulting in two distinct peaks appearing in the spectrum. On resonance, the amplitude of these peaks are equal, which can be used as criteria for determining the exact transition frequency. For small detuning about resonance, the change in amplitude of the features is linear, and the transition frequency can be extracted from the intersection of two straight-line fits as shown in Fig. 5.2.

For an odd number of levels, the field creates a central transparency peak, the relative

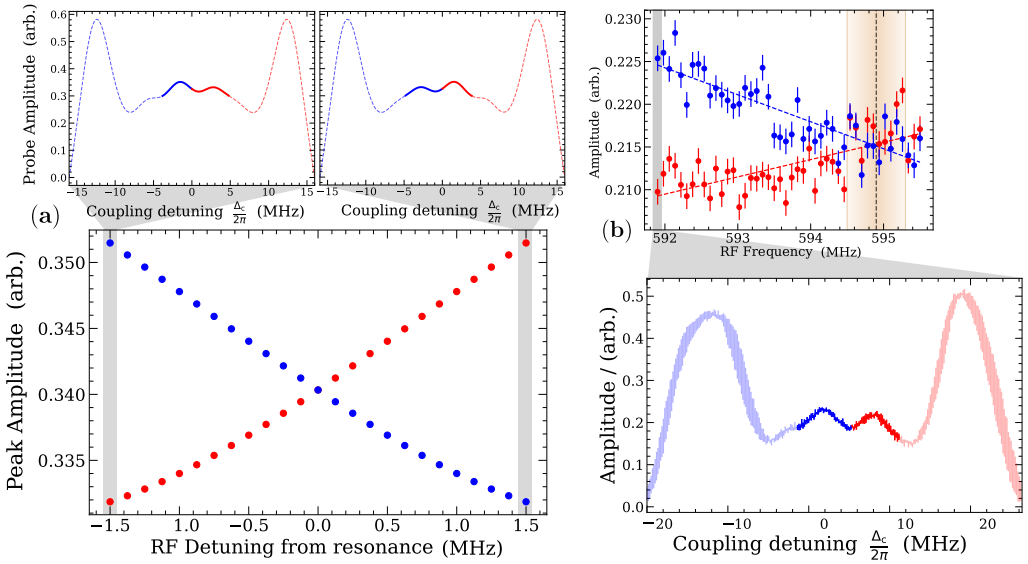

Figure 5.2: Demonstration of method for determining transition frequencies using EIT in even-numbered ladder systems. (**a**) Modelled peak amplitudes (using [49]) against rf detuning of the $18i \rightarrow 18k$ transition. The two insets show modeled spectra when the rf field is detuned 1.5 MHz either side of the $18i \rightarrow 18k$ resonance, corresponding to the first and last pairs of data points. (**b**) Measured peak amplitude data of the $18i \rightarrow 18k$ transition as the rf is detuned. The straight dashed line fit determines where the AT splittings have the same amplitude - assumed to be on resonance when neglecting perturbing effects. The blacked dashed line shows the extracted transition frequency, 594.9(4) MHz, and the error as the shaded beige band, calculated from statistics of the fit. The inset shows the measured spectrum used to extract the first pair of data points when the rf field is 592 MHz. Figure adapted from [2].

detuning of which from the previous AT peaks varies linearly and can similarly be used to determine resonance. An example is shown in Fig. 5.3. Here, once excited to the $18d_{5/2}$ state, a THz field is used to couple to the $15f_{7/2}$ on resonance, which we previously measured to be $-1034.94423(7)$ GHz. With this additional field on, a horn antenna is then used to detune across the $15f_{7/2} \rightarrow 15g_{9/2}$ transition with the other fields kept on resonance. Both methods are then generalised for the higher $\ell \rightarrow \ell'$ measurements. A table of the intervals studied in this thesis and the obtained transition frequencies using these particular schemes are shown in table. 5.2. For certain transitions, we selectively excite the $j = \ell - \frac{1}{2}$ sublevel of the initial state so that only the corresponding $j' = \ell' - \frac{1}{2}$ final state is addressed, effectively excluding the $j' = \ell' + \frac{1}{2}$ state from the observed lineshape. For example, to measure the $g_{7/2}$

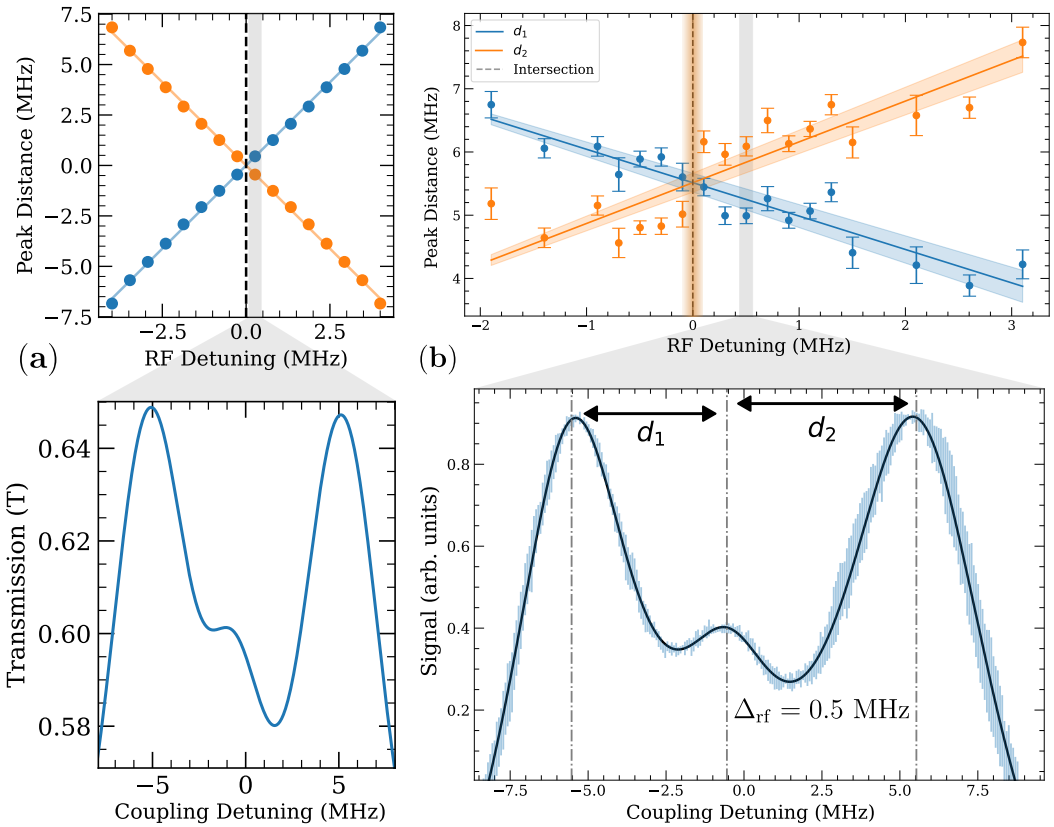

Figure 5.3: Demonstration of method for determining transition frequencies using EIT in an odd-numbered level ladder system. (**a**) Model peak amplitudes (using [50]) against rf detuning. The panel below shows a modelled spectra when the rf field is red-detuned +0.27 MHz (**b**) Extracted peak separations of the data from the $15f_{7/2} \rightarrow 15g_{9/2}$ transition as the rf frequency is detuned. The intersect of the two straight line fits (shown with shaded 1σ standard error regions) determine where the peaks have the same separation with respect to the central feature - assumed to be on resonance when neglecting perturbing effects. The blacked dashed line shows the extracted transition frequency, 50.6009(1) GHz, and the error as the shaded beige band, calculated from statistics of the fit. The panel below shows the measured spectrum used to extract the first pair of data points when the rf field is red-detuned by +0.5 MHz.

state, we excite from the $nf_{5/2}$ state rather than the $nf_{7/2}$ state, since the g-state fine structure cannot be resolved when starting from $nf_{7/2}$. For states with $\ell > 4$ (beyond g), our experimental resolution is insufficient to resolve the fine structure, so we do not attempt selective excitation from the $j = \ell - \frac{1}{2}$ sublevels. Having established how the transition frequencies are extracted from the measured spectra, we now quantify the reliability and limitations of these measurements by analysing the dominant sources of experimental uncertainty.

5.2.2.1 Tables of Measured Intervals

Transition	**Frequency (GHz)**
$18d_{3/2} \rightarrow 15f_{5/2}$	−1034.944 23(7)
$18d_{3/2} \rightarrow 16f_{5/2}$	746.664 04(9)
$18d_{5/2} \rightarrow 15f_{5/2}$	−1050.974 05(8)
$18d_{5/2} \rightarrow 15f_{7/2}$	−1051.248 88(9)
$18d_{5/2} \rightarrow 16f_{5/2}$	730.634 72(8)
$18d_{5/2} \rightarrow 16f_{7/2}$	730.406 83(6)
$19d_{3/2} \rightarrow 17f_{5/2}$	620.578 51(8)
$19d_{5/2} \rightarrow 17f_{5/2}$	607.2809(1)
$19d_{5/2} \rightarrow 17f_{7/2}$	607.091 49(5)
$20d_{3/2} \rightarrow 17f_{5/2}$	−715.185 66(9)
$20d_{3/2} \rightarrow 18f_{5/2}$	521.361 82(9)
$20d_{5/2} \rightarrow 17f_{5/2}$	−726.3370(1)
$20d_{5/2} \rightarrow 17f_{7/2}$	−726.527 29(8)
$20d_{5/2} \rightarrow 18f_{5/2}$	510.2102(1)
$20d_{5/2} \rightarrow 18f_{7/2}$	510.0500(1)
$20d_{5/2} \rightarrow 22p_{3/2}$	1025.9229(2)
$21d_{3/2} \rightarrow 18f_{5/2}$	−603.9741(1)
$21d_{5/2} \rightarrow 18f_{7/2}$	−613.5782(1)
$22d_{3/2} \rightarrow 19f_{5/2}$	−514.6726(1)
$22d_{5/2} \rightarrow 19f_{7/2}$	−522.876 75(9)

Table 5.1: Measured $d \rightarrow f$ and $d \rightarrow p$ transition frequencies with statistical uncertainties from the fitting procedure in parentheses, ordered by principal quantum number of the initial d_j state. The '−' of a transition frequency indicates the final state is lower in energy than the initial state.

Transition	Frequency (GHz)
$15f_{5/2} \rightarrow 15g_{7/2}$	50.3241(2)
$15f_{7/2} \rightarrow 15g_{9/2}$	50.6009(1)
$15g \rightarrow 15h$	8.7008(4)
$15h \rightarrow 15i$	2.6751(5)
$15i \rightarrow 15k$	1.016(1)
$15k \rightarrow 15l$	0.439(1)
$16f_{5/2} \rightarrow 16g_{7/2}$	41.5844(2)
$16f_{7/2} \rightarrow 16g_{9/2}$	41.8139(1)
$16g \rightarrow 16h$	7.1905(5)
$16h \rightarrow 16i$	2.2069(5)
$16i \rightarrow 16k$	0.840(1)
$16k \rightarrow 16l$	0.365(1)
$17f_{5/2} \rightarrow 17g_{7/2}$	34.7509(1)
$17f_{7/2} \rightarrow 17g_{9/2}$	34.9430(1)
$17g \rightarrow 17h$	6.0072(5)
$17h \rightarrow 17i$	1.8513(4)
$17i \rightarrow 17k$	0.705(1)
$17k \rightarrow 17l$	0.306(1)
$18f_{5/2} \rightarrow 18g_{7/2}$	29.3321(1)
$18f_{7/2} \rightarrow 18g_{9/2}$	29.4946(1)
$18f_{7/2} \rightarrow 19g_{9/2}$	1071.337 78(7)
$18g_{9/2} \rightarrow 19h$	1046.1632(3)
$18g \rightarrow 18h$	5.0718(5)
$18h \rightarrow 18i$	1.5634(5)
$18h \rightarrow 19i$	1042.4245(5)
$18i \rightarrow 18k$	0.594(1)
$19f_{5/2} \rightarrow 19g_{7/2}$	24.981(1)
$19f_{7/2} \rightarrow 19g_{9/2}$	25.1200(8)
$19f_{7/2} \rightarrow 18g_{9/2}$	−1016.7236(1)
$19g \rightarrow 19h$	4.3206(5)

Table 5.2: Table of measured transition frequencies using the method described in this chapter, for $f \rightarrow g$, $g \rightarrow h$, $h \rightarrow i$, $i \rightarrow k$ and $k \rightarrow l$ transitions measured via EIT ladder schemes. Fine structure beyond f is not resolved for higher ℓ, but $j = \ell + 1/2$ is used if not indicated in the transition. The '−' of a transition frequency indicates the final state is lower in energy than the initial state.

5.2.3 Measurement Uncertainties

The main source of error from statistical fits is derived from the laser amplitude noise which causes a change in the detected probe power. This could be reduced in experiment via use of laser amplitude stabilisers.

Any detuning from resonance of the previous fields in the ladder scheme will cause an asymmetry in the lineshape. This compounds into a change in the measured resonant frequency of subsequent fields by shifting the AT peak amplitudes. We minimised this uncertainty by first measuring transition frequencies of previous states before those of subsequent states. The uncertainty in these measurements can then be taken as the uncertainty in the rf detuning of the following field. This effect was studied and found to be negligible compared to the statistical errors for our ℓ measurements. This analysis is detailed in appendix B.

The dc stark effect results in a shift of the transition frequency due to stray electric fields in the cell, introducing a further uncertainty [148]. It has been recently highlighted that the polarisability scales significantly with high ℓ states and as such would present a significant uncertainty on the higher ℓ transitions measured [116]. Whilst we cannot currently reliably measure the magnitude of any stray dc electric fields in the cell, we can place bounds on the expected shift using the polarisability of the state of interest. For example, the polarisability of the $n = 17i$ ($\ell = 6$) state is $119\,\mathrm{MHz\,cm^{-2}/V^2}$ [149]. From this, we can calculate that a dc electric field uncertainty of order $0.1\,\mathrm{V/cm}$ results in a $0.6\,\mathrm{MHz}$ error in the measured transition frequency. At higher principal quantum number, this effect presents a significant uncertainty due to the already present n^7 scaling. The $40i$ state has an expected polarisability of $(56.8\times10^3)\,\mathrm{MHz\,cm^{-2}/V^2}$. Whilst this effect is not significant for the f or g transitions, this is a significant uncertainty when measured transitions are on the order of hundreds of MHz and would be significantly larger at higher Rydberg states. During our measurements, we did not observe any mixing of different states in the Rydberg manifold if the rf field was significantly detuned.

The ac Stark effect may become significant as the number of fields increases during higher ℓ measurements. Similarly, this was minimised by first taking a measurement at low power of the dressing field to minimise this shift. Numerical models, such as those included in `arc` (using an implementation of Shirley's time-independent floquet Hamiltonian [77]), could be used to estimate the ac Stark shift for a given electric field strength which could be estimated from the Rabi frequency of said field. The shift in the resonance of subsequent fields could be investigated against the field strength of previous fields and the resonant frequency could be taken in the limit of zero field strength. However, from observation we found that there was no indication of large ac Stark shifts on the level of errors provided from the statistical fits which we do not expect at our low n and the rf powers used ($\lesssim 10$ µW).

5.3 Quantum Defect Determination

In contrast to some precision spectroscopy approaches, we do not reference our measurements to the absolute ground state ($6s_{1/2}$), and are therefore insensitive to the absolute ionisation energy. Instead, we measure energy intervals between Rydberg states. These relative measurements are sufficient to determine the quantum defects for each ℓ_j series through a global least-squares minimisation, which is carried out in this section.

Previously we have given the absolute energy of a state of an alkali-metal atom. The energy separation, as a frequency ν_0, between two states described by the quantum numbers n, ℓ, j and n', ℓ', j' is given by

$$\nu_0 = cR_{\mathrm{Cs}} \left(\frac{1}{(n - \delta_{\ell j}(n))^2} - \frac{1}{(n' - \delta_{\ell' j'}(n'))^2} \right), \tag{5.1}$$

where R_{Cs} is the Rydberg constant (in m^{-1}) corrected for the mass of the relevant species (Cs in this case). The quantum defects, $\delta_{\ell j}(n)$, can be parametrised using the modified Rydberg-Ritz equation as [150]

$$\delta_{l,j}(n) = \delta_0 + \frac{\delta_2}{(n - \delta_0)^2} + \frac{\delta_4}{(n - \delta_0)^4} + \frac{\delta_6}{(n - \delta_0)^6} + \ldots \tag{5.2}$$

where the values for $\delta_{0,2,4,...}$ are coefficients that are distinct for different ℓ and j. Using previously reported values of these coefficients (see Table 5.3), we calculated the expected transition frequencies from Eq. (5.1) and compared them to those measured in this work. The predicted and measured frequencies show noticeable deviations, particularly for states with $n < 20$.

Fig. 5.4 illustrates the difference between the predicted and measured transition frequencies as a function of the average principal quantum number of the transition, $n_{\text{avg}} = (n + n')/2$, where n and n' correspond to the initial and final states of each transition respectively.

The plot reveals a distinct structure, with each data point corresponding to a different measured transition. For all series considered, the differences are more apparent at lower n. Since the value of the quantum defect $\delta_{\ell,j}$ depends inversely on n, we posit that inaccuracies in the underlying empirical coefficients $\delta_{0,2,4}$ are responsible for the observed difference between experiment and theory. These differences are not correlated with frequency, so are not due to any frequency-dependent effects in the terahertz or microwave generation. While there may be slight shifts in our measurements caused by external effects such as for example a dc electric field, any such shifts would typically increase with n and so are unlikely to be the cause of the differences seen here.

The three largest discrepancies are for measurements of the $p_j \rightarrow d_j$ transitions at low n where a difference of over 100 MHz is observed between our intervals and those predicted by the collated historical quantum defects. As n increases the observed discrepancy is less apparent, on the order of several MHz at higher n, with $np_{3/2} \rightarrow n'd_{5/2}$ transitions showing discrepancies of up to 4 MHz. The $s_{1/2} \rightarrow p_j$ series measurements show a systematic discrepancy of several MHz throughout, suggesting some inaccuracy present in the δ_0 coefficient of the $s_{1/2}$, $p_{1/2}$ or $p_{3/2}$ quantum defects. Given that the $p_j \rightarrow d_j$ set of intervals describe the data well at high n, and that there is no structure when comparing the $s_{1/2} \rightarrow p_{1/2}$ and $s_{1/2} \rightarrow p_{3/2}$ intervals, the most likely source of this discrepancy lies in the $s_{1/2}$

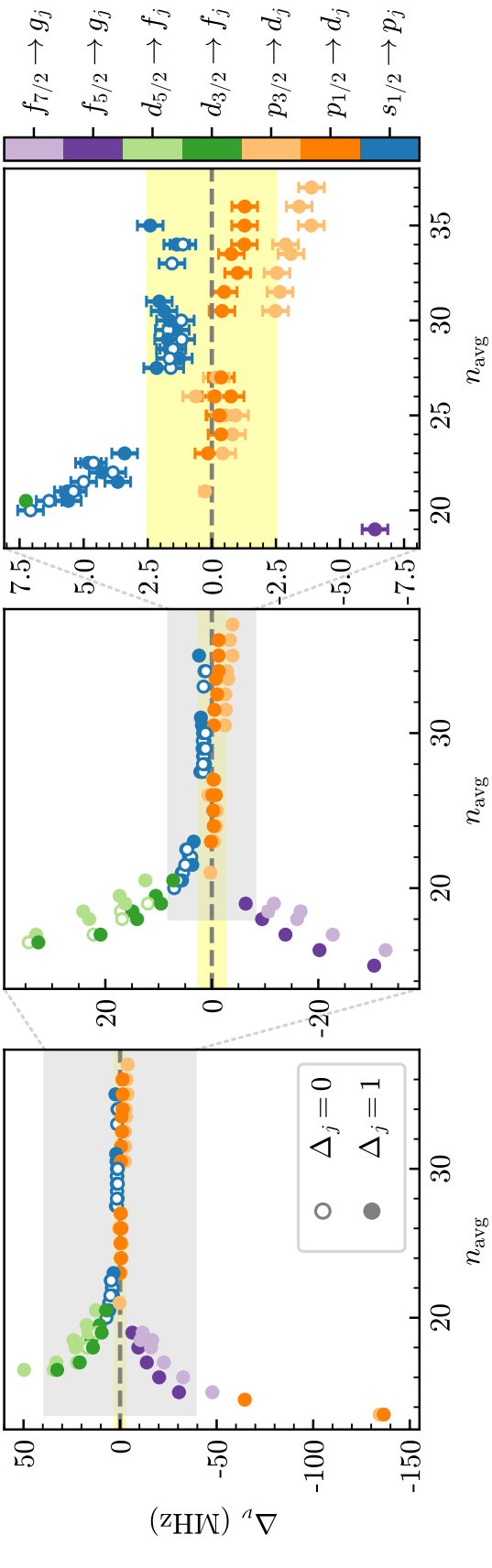

Figure 5.4: The difference (Δ_ν) between our observed transition frequencies and those calculated using quantum defect values from the most recent measurements for each ℓ_j state. The marker style denotes the change in j with $\Delta_j = +1$ (filled) or $\Delta_j = 0$ (empty). The colours of the points correspond to the different ℓ series considered. Error bars are derived from the determination of the crossing point as shown in Fig. 5.1. The grey shading indicates the zoom region shown in the subsequent panel. The yellow shading highlights the range in which our optimised values lie. Figure reproduced from [2] and uses data from [80].

quantum defects. For the $d_j \rightarrow f_j$ and $f_j \rightarrow g_j$ transitions, discrepancies on the order of tens of MHz are observed with a clear n dependence. This suggests that the f-state defects from [139] are inaccurate at low n. When accounting for this in our g-state analysis, and comparing to transition frequencies based on the $g_{7/2}$ defects from [136], we find that the g quantum defect given from this work overestimates the transitions by several MHz relative to our measurements.

In addition to this literature comparison, we use our measured transition frequencies to extract measurements of the quantum defect parameters $\delta_{0,2,4}$ in Cs for all states with $\ell \leq 4$ without relying on any data from other sources. In addition to the transition frequencies determined in this thesis, we also use measurements from those of Downes using a similar method in a three-photon experiment [80]. These include measurements of $s_{1/2} \rightarrow p_j$ and $p_j \rightarrow d_j$ states so that these quantum defects can be determined. A full list of the transitions used in the global fit is included in Appendix A. By using THz frequencies, measuring intervals at significantly lower n than other publications is possible, increasing our sensitivity to changes in quantum defects. A global fit was performed, optimising the values of all quantum defects simultaneously. We use equations (5.1) and (5.2) as a theoretical model to calculate the transition frequencies for initial values of δ_0, δ_2, and δ_4 for all relevant states. A least-squares χ^2 minimisation method, implemented via the SciPy `optimise` package in Python, varied the values of δ_i to minimise the differences between the predicted and measured transition frequencies. Table 5.3 shows our optimised values of the coefficients from equation (5.2) and the residuals of the fit are shown in Fig. 5.5.

Although the Ritz expansion in equation (5.2) may formally be extended to arbitrarily high order, inclusion of terms beyond δ_4 did not produce a statistically significant improvement in the reduced χ^2 value for the present dataset. Higher-order coefficients were also found to be poorly constrained and strongly correlated with lower-order parameters, indicating that the available experimental precision was insufficient to reliably determine additional terms. Including further free para-

meters therefore increased the risk of overfitting the experimental noise without improving the physical accuracy of the model [151]. For this reason, the expansion was truncated at fourth order.

Our values for the quantum defects largely agree with the values reported in [136] but, in contrast to the work presented there, do not rely on data from other sources. The error in their measurements is likely underestimated, especially for the higher order quantum defects where values are quoted to a superfluous number of significant figures. While our measurements are of a lower precision than [140], they agree within error.

5.4 Discussion

In the minimisation it was found that there are strong correlations between the optimum values of the δ_i coefficients for each $\delta_{\ell,j}$. Whilst this would not affect the optimum value of the fit parameters, it does put bounds on the precision for each coefficient. Additionally, as the fitting minimises transitions between pairs of states, quantum defects for a specific ℓ are correlated to those with $\ell \pm 1$. Further details of the correlations between parameters can be found in the appendix of [2]. One of the main use-cases for quantum defect measurements is to calculate the frequency of a specific atomic transition through equation (5.1). In this case the precision of the quantum defect parameters is the dominant source of error and must be accounted for. In the simplest case all parameters ($\delta_{0,2,4}$) can be considered as independent (uncorrelated) and the error in the transition frequency can be calculated by summing the contributions from the uncertainty on each parameter in quadrature [151].

Using the optimised values and their precision as quoted in Table 5.3 we can calculate values of transition frequencies at the MHz level for $n > 30$. Incorporating the correlations between fit parameters in the calculation of the error on the predicted transition frequencies is non-trivial but possible, details of two methods are given

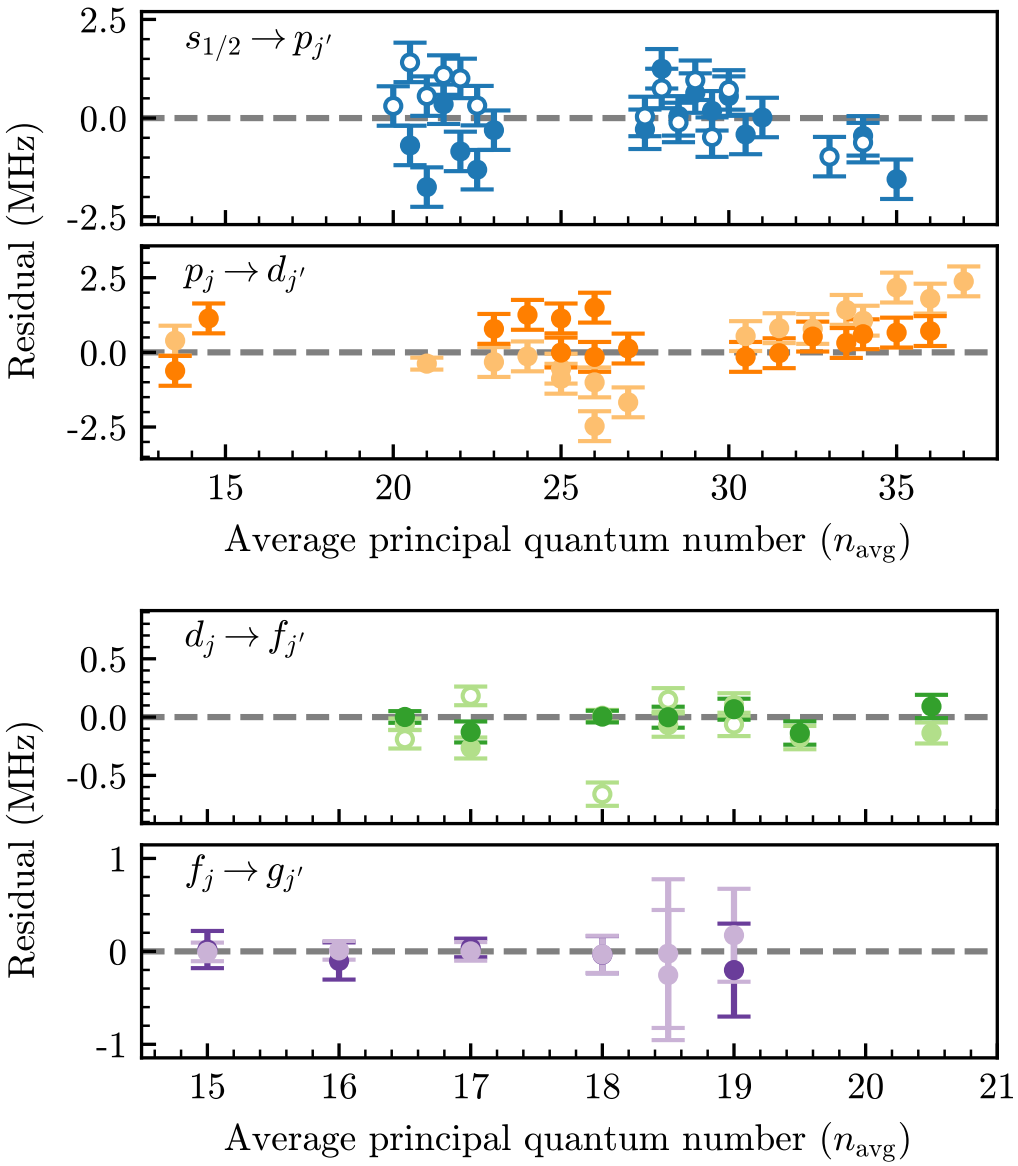

Figure 5.5: Residuals from a global fit to all quantum defects using the transition frequency data. Measured minus calculated transition frequencies as a function of $n_{\mathrm{avg}} = (n + n')/2$ for optimised values of $\delta_{0,2,4}$. The marker style denotes a transition with initial state $n\ell_j$ to a final state $n'\ell'_{j'}$ where $\Delta j = +1$ (filled) or $\Delta j = 0$ (empty). The lighter (darker) points indicate transitions from the higher (lower) fine-structure state, as in Fig 5.4. Figure reproduced from [2] and uses data from [80].

		$s_{1/2}$	$p_{1/2}$	$p_{3/2}$	$d_{3/2}$	$d_{5/2}$	$f_{5/2}$	$f_{7/2}$	$g_{7/2}$	$g_{9/2}$
This work	δ_0	4.049368(3)	3.591606(3)	3.559091(3)	2.475474(4)	2.466327(4)	0.033429(3)	0.033570(3)	0.007057(5)	0.007049(4)
	δ_2	0.2333(14)	0.3569(13)	0.3657(13)	0.0051(14)	0.0101(14)	-0.2025(12)	-0.2016(11)	-0.054(2)	-0.0512(16)
	δ_4	0.8(2)	0.81(14)	1.17(14)	-0.06(16)	0.06(16)	0.69(13)	0.45(11)	0.5(3)	0.20(19)
Historical Works[a]	δ_0	4.0493532(4)	3.5915871(3)	3.5590676(3)	2.4754562	2.466 3144(6)	0.03341537(70)	0.0335646(13)	0.00703865(70)	-
	δ_2	0.2391(5)	0.36273(16)	0.37469(14)	0.009320	0.01381(15)	-0.2014(16)	-0.2052(29)	-0.049252	-
	δ_4	0.06(10)	-	-	-0.43498	-0.392(12)	-	-	0.01291	-
	δ_6	11(7)	-	-	-0.76358	-1.9(3)	-	-	-	-
	δ_8	-209(150)	-	-	-18.0061	-	-	-	-	-
Shen et. al (2024)[152] and Shen et. al (2025)[153].	δ_0	4.04935994(17)	3.5915871(3)	3.5590676(3)	2.47545840(13)	2.46631529(14)	0.03341493(18)	0.03356289(19)	-	-
	δ_2	0.238017(18)	0.36273(16)	0.37469(14)	0.008339(62)	0.013431(65)	-0.20036(14)	-0.20289(14)	-	-
	δ_4	0.1747(33)	0.0	0.0	-0.3769(95)	-0.3613(61)	0.2825(8)	0.2998(9)	-	-

Table 5.3: A table of quantum defect values found in this work compared to a collation the most recent measurements. The quantum defect coefficients for all spectral series up to $\ell = 4$, both our optimised values and the most recent literature values are listed. The error in the optimised coefficients was calculated from the covariance matrix generated during the fit. Errors on the literature values are given where available.

[a]The $s_{1/2}$, $p_{1/2}$, $p_{3/2}$, $d_{5/2}$, quantum defects are from [140], the $d_{3/2}$ are from [142], the $f_{5/2}$ and $f_{7/2}$ are from [139] and the $g_{7/2}$ quantum defect is from [136]. No $g_{9/2}$ literature value was found.

in the appendix of [2]. Doing so increases the precision of transition frequencies calculated using our quoted parameters by up to an order of magnitude. This means that we can predict transition frequencies with a similar precision as those calculated using more precise measurements of $\delta_{0,2,4}$ such as quoted in Table 5.3.

Since performing the analysis presented in this chapter and tabulating the quantum defects listed in Table 5.3, more precise measurements for the $s_{1/2}$, $d_{3/2}$ and $d_{5/2}$ states have been made [152]. Using the updated values to compute theoretical transition frequencies did not significantly reduce the discrepancies with our data, particularly the >10 MHz shifts at low n_{avg} and the consistent 1–2 MHz offsets at higher n_{avg} seen in Fig. 5.4. Notably, [152] excludes states with $n \leq 20$, where most of the large deviations occur.

The global fit residuals of ±2 MHz in Fig. 5.4 for $s_{1/2} \rightarrow p_j$ and $p_j \rightarrow d_j$ transitions at $n_{\mathrm{avg}} = 35$ are consistent with a small ($< 10\,\mathrm{mV/cm}$) dc electric field. However, most measurements are in the lower $n = 15$–30 range or involve higher ℓ, where any resulting shifts are smaller than our measurement uncertainties (10–100 kHz). Inclusion of electrodes in the cell would allow for compensation of small electric fields, especially if measurements were carried out at higher n.

Laser power fluctuation is a large source of error in determining the peak heights, this could be reduced by the inclusion of amplitude stabilisation techniques. In the ladder scheme, the error caused by any detuning of the previous transitions was minimised by measuring each resonance sequentially, and associated shifts were found to be negligible compared to the dominant fitting uncertainty. AC Stark shifts from earlier rf fields were also negligible at the low field strengths used. Electric-field non-uniformity would cause distortion of the lineshape [118] however such distortions are symmetric and were not observed with the rf powers used in this work. Implementation of amplitude stabilisation would likely require reevaluation of the other errors mentioned previously as they would come into the same order of magnitude as the reduced statistical error.

The frequency separation of the Autler-Townes splitting itself could be used to determine resonance. However, this approach is non-linear in detuning and sensitive to laser scan calibration. Additionally, the small detuning range used in this work results in near-constant splitting. Fitting relative peak heights could reduce common-mode noise, but it introduces correlations that add to the error. Ideally, normalisation of peak height using background scans would be preferred, but rapid laser power fluctuations occur on timescales shorter than our rf/THz switching, limiting the practicality of this approach.

5.5 Conclusion

In this chapter, we have presented a comprehensive set of independent measurements of Rydberg transition frequencies in caesium using electromagnetically induced transparency combined with tunable THz and rf fields. By exploiting the symmetry and amplitude asymmetry of EIT lineshapes, we demonstrated a method for determining resonance frequencies.

Our measurements span the $s_{1/2}$, $p_{1/2}$, $p_{3/2}$, $d_{3/2}$, $d_{5/2}$, $f_{5/2}$, $f_{7/2}$, $g_{7/2}$ and $g_{9/2}$ Rydberg series, covering transitions over a wide range of principal quantum numbers. Through global least-squares fitting of the observed transition frequencies, we have derived new values of the quantum defect parameters $\delta_{0,2,4}$ for all states with $\ell \leq 4$. These results form the first independent, complete and self-contained set of quantum defects for caesium. Our findings show clear deviations from previously reported values, particularly for low-n transitions, where the sensitivity to variations in $\delta_{\ell,j}$ is greatest. Strategies to further reduce these sources of uncertainty, such as amplitude stabilisation and electric-field compensation, are proposed for future work.

The optimised quantum defect values obtained here allow for the calculation of Cs Rydberg energy levels and transition frequencies to MHz-level precision across a broad range of n. This precision provides a solid foundation for subsequent determinations of the Cs^+ core polarisabilities, discussed in the following chapter,

and for benchmarking ab initio theoretical methods. More broadly, this work establishes a complete and independent reference dataset for caesium Rydberg states up to $\ell = 4$, supporting improved modelling in applications ranging from quantum sensing and communications to fundamental tests of atomic structure.

Chapter 6

Core Polarisability Analysis

The work presented in this chapter is based on material published in [2].

6.1 Introduction

In the previous chapter, transition measurements between low-angular-momentum states were used to extract the quantum defects for each ℓ_j series in caesium. In principle, this procedure could be extended to determine quantum defects for all higher ℓ_j series. However, such measurements become experimentally impractical at larger ℓ, since accessing these states requires multi-photon excitation pathways with progressively complex line shapes. Moreover, attempting to determine several quantum defects simultaneously through a global fit would introduce significant parameter correlations, leading to larger uncertainties, particularly when only a limited number of experimental data points are available.

Rather than use a quantum defect approach, the energies of all higher ℓ states

($\ell \geq 5$) can be calculated from the polarisabilities of the ionic core, which describe the decrease in energy caused by the polarisation of the atomic core, Cs^+, due to the electron's motion [17]. As the wavefunction's penetration into the core is small [40] for high–ℓ states, the total energy becomes increasingly dominated by the long-range polarisation potential, rather than any energy shift due to penetration, a shift due to the electron's wave function penetration into the ionic core, or exchange effects, the energy shift due to the exchange interaction between the core electrons and the valence electron [154].

In this chapter, an overview of Rydberg high–ℓ spectroscopy is given as well as the applications in determination of the polarisabilities and consequences of improving the accuracy in calculation of the energy levels. We use our measured transition frequencies between high–ℓ states to determine the dipole (α_d) and quadrupole (α_q) polarisabilities of the Cs ionic core, Cs^+. These constants are used to model the energies of states with angular momentum $\ell \geq 5$ and provides a systematic framework for determining the quantum defects of all higher ℓ states [40] without their direct measurement.

The measurement of Rydberg high–ℓ states has been used to extract ion polarisabilities [155]. This technique is not limited to alkali metals [156, 157, 158] and has been explored in alkaline-earth elements [159, 160] and other species [161, 162]. For simpler species, such as He and H_2, comparisons between theoretical and experimental results have further validated these models [163, 164]. Beyond this, ionic polarisabilities have a range of applications [165] from the study of ion-neutral and atom-atom interactions [166, 167, 168] to addressing black-body radiation uncertainties in ionic and atomic clocks [169, 170]. Proposals to trap atoms using circular states [171] and improve measurements of the Rydberg constant have highlighted the need for improved ionic polarisability constants [172, 173] with recent studies identifying it as a leading uncertainty [174]. Accurate determination of atomic polarisabilities is also critical for calculating tune-out wavelengths and Stark shifts, which depend on the contribution from the core [175, 176]. In a recent Cs measurement, this is

the dominant source of error in determining the ratio of the $6p$ reduced matrix elements [177].

More fundamentally, the better accuracy of the core polarisabilities to determine energy levels would be principally used in the calculation of the Stark structure of alkali-metal atoms [148]. Here, the Hamiltonian in the presence of a dc electric field is diagonalised requiring the calculation of the entire n and, often, adjacent n manifolds to accurately determine mixing between states and the magnitude of dc-Stark shifts [148, 120], useful for the study of circular Rydberg states [99]. Additionally, the constant is used to compute the electronic wavefunctions in alkali-metal atoms [41] which in turn enter into calculations of scalar and tensor polarisabilities of atomic states [178] as well as dipole matrix elements [179]. In particular for Cs, the contribution of the ionic core polarisability to the total state polarisabilities is significantly larger than all other alkali metals [180]. The accuracy of these constants directly impact the performance of Rydberg atom–based electric field sensors and neutral atom–based quantum computing platforms [152]

Previous studies of core polarisation in alkali metals typically relied on atomic beam experiments, where multi-photon microwave and rf transitions populate excited $n\ell$ states, which were subsequently detected via field ionisation [181, 182, 100]. Techniques like resonant excitation Stark ionisation spectroscopy (RESIS), where an atomic or ionic beam is excited and captures an electron by passing through a Rydberg target, which is then subsequently excited by a Rydberg laser and ionised. These experiments have observed ℓ states as high as 14, though significant experimental setup and dc Stark corrections are required [183, 184]. Here we use our measured Cs Rydberg high–ℓ transitions to extract the dipole and quadrupole polarisabilities of the Cs ionic core.

The energy of an atomic state in an alkali metal, encapsulated by its quantum defect, reflects the combined influence of several physical effects, including relativistic corrections, core polarisation, and valence–core exchange interactions. To interpret these shifts quantitatively, the total energy of a Rydberg state can be expressed as

the sum of additive contributions:

$$E_{n\ell j} = E_{I_{\mathrm{Cs}}} - \frac{hcR_{\mathrm{Cs}}}{n^2} - \Delta E_{\mathrm{pol}} - \Delta E_{\mathrm{fs}} - \Delta E_{\mathrm{ex}} - \Delta E_{\mathrm{pen}} - \Delta E_{\mathrm{rel}}. \tag{6.1}$$

where $E_{I_{\mathrm{Cs}}}$ is the ionisation energy and R_{Cs} the reduced Rydberg constant for caesium. The correction terms ΔE_{pol}, ΔE_{fs}, ΔE_{ex}, ΔE_{pen}, and ΔE_{rel} represent the polarisation, fine-structure, exchange, penetration, and relativistic energy shifts, respectively [154].

For states with high angular momentum ($\ell \geq 4$), the penetration and exchange contributions become negligible, as the Rydberg electron very weakly penetrates the ionic core. Consequently, the total energy deviation from the hydrogenic term in this regime is dominated by the polarisation term. The definition of 'high–ℓ' adopted here is somewhat conventional and accuracy dependent. These states retain a small but finite core overlap, yet within the precision of modern high-resolution spectroscopy (typically $\sim$1 MHz), such residual effects lie well below the experimental uncertainty. Throughout this thesis, therefore, the term 'high–ℓ state' refers to those for which the energies are accurately described by the hydrogenic model to within current experimental precision, modified only by the core polarisability of the specific atom.

Under this assumption, the observed energy intervals $E_{n\ell} - E_{n\ell'}$ (explicitly, the same n but different ℓ) primarily reflect differences in the polarisation energy, which can be expressed analytically in terms of the dipole and quadrupole polarisabilities (α_d and α_q) and the quantum numbers n and ℓ. The remaining corrections arise from the fine-structure and relativistic contributions, which, for hydrogenic states, take the forms [39]

$$\Delta E_{\mathrm{fs}} = -\frac{\alpha^2 hcR_{\mathrm{Cs}}}{2\ell(\ell+\frac{1}{2})(\ell+1)n^3}\left[j(j+1) - \ell(\ell+1) - \tfrac{3}{4}\right], \tag{6.2}$$

and

$$\Delta E_{\mathrm{rel}} = \frac{\alpha^2 hcR_{\mathrm{Cs}}}{n^3}\left(\frac{1}{\ell+\frac{1}{2}} - \frac{3}{4n}\right), \tag{6.3}$$

these terms incorporate the spin-orbit interaction, Darwin term and relativistic correction we previously mentioned in section 2.2.1. In the present analysis, we

assume this hydrogenic fine-structure scaling and correct all measured intervals such that transitions correspond to an effective $|n\ell\rangle$ level located at the centre of mass of the $|n\ell j\rangle$ manifold. This approximation has been validated in previous studies [101], where the measured fine-structure splittings for g and higher ℓ states in Rb were found consistent with hydrogenic predictions. At lower principal quantum numbers, or for heavier atoms such as Cs with larger cores, small deviations from this approximation may arise. These are expected to produce systematic shifts of order tens to hundreds of kilohertz well below the uncertainty level of the present measurements [185].

Penetration and exchange energies are estimated following the treatment in [185], which shows good agreement with other calculations of g states [154, 158]. While penetration and exchange corrections for g states are small ($\simeq$15 MHz), they are not negligible compared to experimental errors. For $\ell \geq 5$, these corrections are < 100 kHz, well below measurement uncertainty but included for completeness.

This transition from quantum defect to polarisability-based modelling not only reflects the underlying physics but also enables the grouping of our sparse high-ℓ data into a single framework, allowing predictions of unmeasured ℓ_j states. We analyse core polarisation energies using so-called *adiabatic* and *non-adiabatic* models. The former has historical precedence and enables comparison with prior experimental results, while the latter provides greater accuracy in determination of the Cs^+ polarisabilities as it uses a more complete description of the polarisation potential [186, 165].

6.2 Analysis

6.2.1 Adiabatic Model

The adiabatic polarisation energy ΔE_{pol}, in atomic units, is given by [187]

$$\Delta E_{\text{pol}} = -\frac{1}{2}\alpha_d' \langle r_{n\ell}^{-4} \rangle - \frac{1}{2}\alpha_q' \langle r_{n\ell}^{-6} \rangle, \tag{6.4}$$

where α_d' and α_q' are the effective dipole and quadrupole polarisabilties of the Cs^+ ion, and $\langle r_{n\ell}^m \rangle$ are the radial m^{th} power expectation values of the hydrogenic wavefunction, $|n\ell\rangle$ [188]. Equation (6.4) is from a perturbative treatment from [189] which considers the decrease in energy of the valence electron due it polarising the ionic core from the electrostatic interaction. The $'$ denotes the 'effective' polarisabilities which imply the treatment considers the electron slowly moving, referring to the ionic core developing an instantaneous dipole to follow the electron, because the internal excitations of the core are much faster than the electron's motion. This nomenclature follows that of Freeman and Kleppner [40]. Literature may use this model but not explicitly refer to the adiabatic model, meaning their results of the dipole or quadrupole polarisability are the effective values [100]. A non-adiabatic model is one which includes corrections to account for the electron's motion, shown later in this chapter.

It is instructive to examine how polarisation energy varies with angular momentum; in particular, transitions of the form $n\ell \to n\ell'$ (at fixed n) provide a sensitive probe of the underlying polarisation dynamics. These transitions, conveniently our measurements shown in the previous chapter, display differences in polarisation energy which can be linearised through using equation (6.4) to

$$2\frac{\Delta E_{\text{pol},n\ell} - \Delta E_{\text{pol},n\ell'}}{\langle r_{n\ell}^{-4} \rangle - \langle r_{n\ell'}^{-4} \rangle} = \alpha_d' + \alpha_q' \frac{\langle r_{n\ell}^{-6} \rangle - \langle r_{n\ell'}^{-6} \rangle}{\langle r_{n\ell}^{-4} \rangle - \langle r_{n\ell'}^{-4} \rangle}, \tag{6.5}$$

where $\Delta E_{\text{pol},n\ell} - \Delta E_{\text{pol},n\ell'}$ are polarisation energies extracted from the measured transitions. In this way, the gradient and intercept of this linear equation correspond to the effective quadrupole, α_q' and dipole polarisability, α_d', respectively. Such a plot is sometimes called a 'polarisation plot' and can take different forms depending on completeness of the polarisation potential used [165, 190].

We apply the adiabatic model to two different datasets. One data set uses intervals of the form $n\ell \to n\ell'$ where the principal quantum number has not changed. However, given our $nf \to n'g$ measurements contain information on the energies of g states, we can neglect the need for identical n intervals to perform a linearisation of data

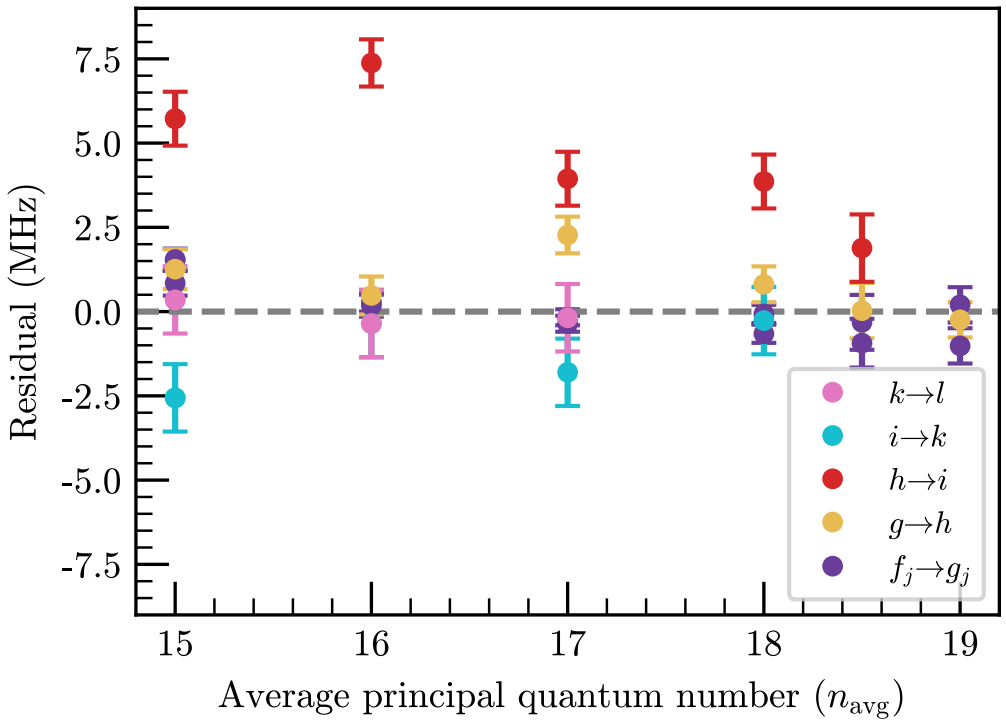

Figure 6.1: Plot of transition frequency intervals obtained from describing $\ell \geq 4$ states using an adiabatic model for polarisation energy. A fit inclusive of g_j states (from the measured $nf_j \rightarrow n'g_j$ intervals) is included with the series of $\ell \geq 4$ measurements taken where the energy of a state is described as a series of contribution from the fine-structure, relativistic, exchange, polarisation and penetration corrections. Figure reproduced from [2].

and perform a second global fit using all available intervals. In this way, a state $n\ell$ with $\ell \geq 4$ is simply given by equation (6.4) instead of unique quantum defects for each ℓ_j series. Physically, there is no difference in the way the energies are described in the two data sets but the linearisation of the model allows better visual inspection and comparison of the data to the adiabatic model, as when inclusive of the $f \rightarrow g$ data, only fitting residuals can be inspected. The residuals for the adiabatic model when using all available data is shown in Fig. 6.1.

The adiabatic model describes the data well and shows good agreement with previous literature values of α'_d as shown in table 6.1. Conversely, the value of α'_q is in reasonable agreement considering the significant variance between publications. Our disagreement with [136] and [154] can likely be attributed to them only performing

measurements on f and/or g states, where inclusion of higher ℓ states give better information on the value of α_q'. Additionally, the inclusion of very low n values, where the adiabatic approximation is more inaccurate and core penetration is much more significant [120], forms part of their analysis. In [100], low-lying Rydberg states ($n = 16$–18, $4 \leq \ell \leq 6$) were used but core penetration and exchange effects were not taken into account for g states. Omitting these corrections would lead to an increase in α_q' and decrease α_d' as ΔE_{pol} would be larger than expected for g states. Furthermore, there is disagreement between our measurements of the same $nf_j \rightarrow ng_j$ intervals. Whilst the penetration and exchange energies are small and only represent 0.1% of the measured transition frequencies, they have significant impact on the value of α_q' given their relative sensitivity, compared to higher ℓ states, from the larger ratio of $\frac{\langle r_{n\ell}^{-6}\rangle - \langle r_{n\ell'}^{-6}\rangle}{\langle r_{n\ell}^{-4}\rangle - \langle r_{n\ell'}^{-4}\rangle}$. By including the g_j levels from the set of $f_j \rightarrow g_j$ transition data, the value of α_d' decreases and α_q' increases expected from the weighting of these data points to lower ℓ transitions.

Inspection of the global fit in Fig. 6.1 suggests that the nh levels are anomalous. This is indicated by slightly elevated $g \rightarrow h$ residuals and large $h \rightarrow i$ residuals. While the former may be attributed to an overestimation of E_{pen} for the g states, this explanation does not account for the latter measurements, as the penetration energies are on the order of kHz. We considered that this may be the result of a large dc stray electric field, as polarisability scales significantly with ℓ [187]. This would decrease the transition frequency for successive $n\ell \rightarrow n\ell'$ measurements. While this effect is observed in the $h \rightarrow i$ dataset, it is not supported by the higher $\ell \rightarrow \ell'$ transitions, which do not show a corresponding decrease in energy. It is interesting to note that [181] also observed smaller $h \rightarrow i$ intervals than their fit. They made similar conclusions, but they do not measure to higher ℓ to further clarify whether this is the result of a stray dc electric field.

Additionally, [100] agrees well with our set of $h \rightarrow i$ measurements within their precision. Their interval sizes are not significantly larger, meaning they do not indicate the presence of a large stray field in our work. Using a non-adiabatic

Reference	α'_d (a_0^3)	α'_q (a_0^5)	$\chi^2_{\nu,\,\mathrm{min}}$
This work ($\ell \geq 4$)	15.634(17)	59.8(13)	6.0
This work (global fit)	15.689(17)	55.7(18)	7.3
Safinya *et al.* [100] (Expt.)	15.544(30)	70.7(29)	
Sansonetti *et al.* [154] (Expt.)	15.79(1)	38.7(19)	
Curtis & Ramanujam [191]*	15.759	47.990	
Weber & Sansonetti [136] (Expt.)	15.770(3)	48.9(4)	
Zhou & Norcross [192] (Expt.)	-	33.60(66)	

Table 6.1: Table of effective Cs^+ polarisabilities compared to previous experimental results of the effective dipole, α'_d, and quadrupole, α'_q, polarisability. The table shows our results for two data sets, one excluding the $nf \rightarrow n'g$ intervals ('$\ell \geq 4$') and one inclusive ('global fit'). The fitted parameters were found by the minimisation of the reduced χ^2 statistic and the errors by re-fitting to $\chi^2_{\mathrm{min}} + 1$ [151].

model as in the following section somewhat resolves this discrepancy. Further measurements of higher ℓ states or a larger sample of n may put more confidence on whether this is a systematic error or an unaccounted perturbation.

6.2.2 Non-Adiabatic Model

A non-adiabatic model introduces corrections to equation (6.4) by accounting for the delayed response of the core dipole to the outer electron's motion [195], allowing extraction of the true static polarisabilities. The non-adiabatic model accounts for the dynamic lag of the core electrons, which becomes relevant as the Rydberg electron's orbital frequency approaches the core excitation frequencies. This work presents the first experimentally determined values of the true static polarisabilities of the Cs^+ ion, as all previously reported values have been based on *ab initio* calculations, as well as the latest experiment to determine Cs core polarisabilities in almost forty years [122].

Two recent treatments addressing adiabatic corrections are Berl *et al.* [181] and Peper *et al.* [158]. The former corrects for non-adiabatic effects using the method of Gallagher for measurements in Rb, introducing correcting factors as coefficients in equation (6.4) by considering ionic dipole and quadrupole matrix elements [187].

*Using data from [154, 193, 194]

The latter follows the treatment of Eissa and Öpik in ^{39}K [196] whereby correction factors, y_0^d, y_0^q, and y_2^d, are introduced into equation (6.4) giving

$$\Delta E_{\text{pol}} = -\frac{1}{2}\alpha_d(y_0^d\langle r_{n\ell}^{-4}\rangle + y_2^d\langle r_{n\ell}^{-6}\rangle) - \frac{1}{2}\alpha_q y_0^q\langle r_{n\ell}^{-6}\rangle, \tag{6.6}$$

where each correcting factor is a function of n and ℓ. Physically, these arise from higher multipole moments induced by the electron as it polarises the core, sometimes described as 'distortion' in this literature. Evaluation of these is beyond the scope of this work but described in [196]. The treatment given in [158] approximates each $y(n,\ell)$, over their much higher Rydberg states ($n = 30$–47), to be static and uses constants found in previous work to evaluate these. For our case, it is likely that y would need to be evaluated for each $n\ell$ state as we are at much lower n. The work of Patil for the treatment of non-adiabatic polarisation effects was also considered as a method for modelling the data [197, 198] however, this was not used due to the absence of experimental studies applying it in the context of Cs or comparable alkali systems. In the absence of empirical validation or precedent, its applicability remains uncertain. This highlights a broader issue: the variety of treatments for non-adiabatic effects and extensions to the polarisation potential underlines the need for a more systematic and comparative analysis, as also noted in [165]. In this chapter, we follow the treatment given by Drake and Swainson to extract the true polarisabilities [199]. The non-adiabatic polarisation energy, ΔE_{pol}, can be written as [165]

$$\Delta E_{\text{pol}} = -\frac{1}{2}\alpha_d\langle r_{n\ell}^{-4}\rangle - \frac{1}{2}(\alpha_q - 6\beta)\langle r_{n\ell}^{-6}\rangle + E^{(2)} + \ldots \tag{6.7}$$

Here, β is a non-adiabatic correction factor [195], a constant which is estimated via extrapolation of oscillator strength sum rules. Specifically, we have [200]

$$S(k) = \left(E_{01} - \frac{a}{(2.5-k)} + \frac{b}{(2.5-k)^2}\right)^k S(0) \tag{6.8}$$

where E_{01} is the energy difference between the ground and first excited state of the core, $5p^6\ {}^1S_0 \rightarrow 5p^5 6s\ 3/2\ [3/2]_2^\circ$, in Rydbergs [201]. The a and b are fitting constants which can be determined from the values $S(0)$, the number of electrons in the core, $S(-1) = \frac{1}{3}\langle\sum_i r_i^2\rangle$, where r_i are the positions of the core elections, and

$S(-2) = \alpha_d/4$ with $S(-3) = \beta/4$ being the quantity to be estimated. The quantity $S(-1)$ is estimated by using the values of the isoelectronic Xe for which $S(-1)$ is known and the ratios of the diamagnetic susceptibilities of Cs^+ and Xe which are taken from theory [202]. Since the extrapolation of $S(-1)$ depends on the dipole polarisability, α_d, being extracted, an iterative fitting process is used in which fits are refined until the value of β converges, which we find to be 8.4, close to that reported in [186]. The term $E^{(2)}$ represents second-order polarisation effects, a correction term which is a function of α_d, n, and ℓ. Higher-order corrections, not included in equation (6.7), to the polarisation potential depend on ionic oscillator strength sums [184] for Cs^+, which are not well characterised. A renewed interest in the theory may be warranted, especially in the case of caesium, which has few literature analyses in comparison to other species and little accessibility when compared to established non-adiabatic theory in studies of K [196, 158].

The non-adiabatic model describes the data well and an extension of equation (6.5) to include non-adiabatic corrections is shown in Fig. 6.2. We find $\alpha_d = 15.729(18)\, a_0^3$ and $\alpha_q = 76.3(1.9)\, a_0^5$ which show good agreement with the theoretical results shown in Table 6.2 [202, 203, 204], the value of α_d we obtain is within 0.5% of these predictions. However, we note the variance in α_q in the literature and the fact that our experimental value is smaller than all theoretical predictions. The non-adiabatic model somewhat resolves the anomalous $h \to i$ data although there is still some discrepancy when performing a global fit inclusive of the $f \to g$ data which give less weight to the $h \to i$ set of data.

Quantum defects for states with $\ell \geq 5$ can then be directly determined from expansions of equation (6.4) [199], or their energies can be expressed using equation (6.1) where their penetration and exchange effects can be considered negligible.

*Inferred from their effective value, α_q'

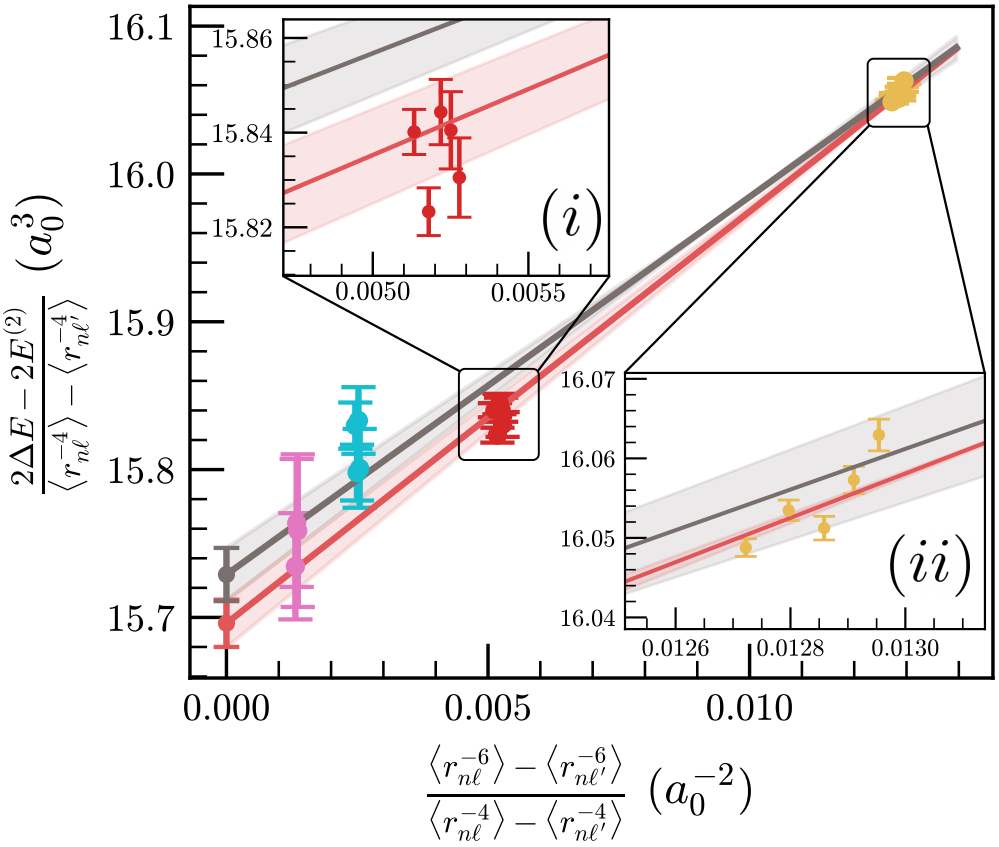

Figure 6.2: Analysis of the data using the non-adiabatic model for two sets of data using a polarisation plot. Linearisation of the data by extending equation (5) to include the non-adiabatic polarisation energy from equation (6), allowing extraction of the dipole, α_d, and quadrupole, α_q, polarisability. A global fit to all data (including g_j states from the $nf_j \rightarrow n'g_j$ intervals) is included in the plot (black) for comparison to data where only intervals of the form $n\ell \rightarrow n\ell'$ (same n) are used (red). The shaded regions show the $\pm 1\sigma$ standard errors in the fitted parameters (see table 6.2). Groups of data points correspond to different sets of transitions with increasing ℓ: **(i)** $nh \rightarrow ni$ **(ii)** $ng \rightarrow nh$. In the lower left, the transitions $ni \rightarrow nk$, $nk \rightarrow nl$ are shown, along with the y-intercepts, which correspond to α_d for the two fits. The data sets are grouped by colour similarly to Fig. 6.1. Figure reproduced from [2].

6.3 Discussion

The set of quantum defects presented in the previous chapter for the s, p, d, f and g states and the determination of core polarisabilities in this chapter will allow more accurate energy levels for reference databases such as `arc` [149], Rydberg atom interaction potentials and in the calculation of long-range Rydberg

Reference	α_d (a_0^3)	α_q (a_0^5)	$\chi^2_{\nu,\,\mathrm{min}}$
This work ($\ell \geq 4$)	15.696(16)	78.6(12)	4.2
This work (global fit)	15.729(18)	76.3(19)	5.6
Zhou & Norcross [192] (Expt.)	15.644(5)	96.8(40)*	
Safronova *et al.* [204] (Th.)	15.84	-	
Johnson *et al.* [202] (Th.)	15.81	86.4	
Lim *et al.* [203] (Th.)	15.8(1)	-	
Sternheimer [205] (Th.)	-	118.26	
Mahan [206] (Th.)	15.9	108	

Table 6.2: Table of true Cs^+ polarisabilities compared to various theoretical results of the dipole, α_d, and quadrupole, α_q, polarisability. The table shows our results for two data sets, one excluding the $nf \rightarrow n'g$ intervals ('$\ell \geq 4$') and one inclusive ('global fit') along with their χ^2_ν statistic [151].

molecules [207, 208, 209]. Previously, `arc` used an estimation, $\delta_\ell \approx \delta_g(4/\ell)^5$, which is taken from [187], by truncating $\langle r_{n\ell}^{-4} \rangle$ to the leading term. We advocate for using an adiabatic treatment when predicting the energies of states (by evaluating the polarisation energy) as the accuracy in predicting energies of high–ℓ states is preserved whilst using relatively simple calculations [†]. The non-adiabatic theory is used to improve the extracted accuracy of the dipole and quadrupole polarisability constants of the core to be used in other contexts such as evaluating core contributions in state polarisabilities [204] or calculation of the wavefunction [41]. However, the extended expression of the non-adiabatic energy, especially when inclusive of $E^{(2)}$, is cumbersome and does not substantially improve the predictive accuracy of the high–ℓ energy levels.

In previous studies of the core polarisability of Cs [154] and other alkali-metal atoms [158, 40, 157], f_j has been included as a 'non-penetrating' state. For [154], this gave results for α_d and α_q that were not in agreement with their ng_j energies. By contrast, in lighter species such as Na and K, inclusion of small penetration and exchange corrections for the nf states gave good agreement with experimental energies [158, 40, 157], reflecting the reduced core overlap in these atoms, and, perhaps,

[†]As stated previously, from version 3.7.0 onward, `arc` calculates the energies of these states using the effective atomic core polarisabilities. The author contributed to the implementation of this update.

the reduced precision in older precision spectroscopy experiments. Regardless, the inclusion of our f states in a core polarisation analysis would place better bounds on the value of α_q and only slightly change our value of α_d. Additionally, the polarisation energies for these states would depend substantially on the accuracy of the theoretically predicted penetration and exchange energies. We note the importance of including high–ℓ states beyond f and g states in core polarisability analyses as they allow the deduction of the dipole and quadrupole polarisabilities without reliance on calculation of the exchange and penetration energies.

Extending measurements to higher ℓ yields diminishing returns, as the reduced transition frequencies lead to larger relative uncertainties, and these states primarily constrain α_d with limited sensitivity to α_q. In contrast, a broader range of principal quantum numbers n offers greater leverage for improving the accuracy of both polarisabilities. In our experiment, we are limited both by the range of the THz sources and the two-photon Rydberg laser, which dictate the Rydberg transitions we can measure. A three-photon scheme reaching f Rydberg states would omit the need for a THz source and allow couplings to g states and higher ℓ states with microwaves and mm-waves.

A full list of the intervals used in this chapter and their corresponding transition frequencies, is provided in Appendix A.

6.4 Conclusion

In this chapter, we transitioned from a quantum defect analysis to a core polarisation model to accurately describe caesium Rydberg states with $\ell \geq 4$. By analysing our measured transition frequencies with a non-adiabatic model, we successfully extracted the static dipole (α_d) and quadrupole (α_d) polarisabilities of the Cs^+ ion.

Our derived value for α_d agrees with theoretical predictions to within 0.5%, and inclusive of our result for α_q, both provide an experimental update to historical literature. Collectively, these refined constants allow for the precise prediction

of high-ℓ energy levels without direct measurement. This improved accuracy is predicted to be useful for reducing uncertainties in many atomic physics platforms.

Chapter 7

Technical Noise of EIT-based Rydberg Receivers

Some work presented in this chapter is based on material to be published in *Rydberg Receivers for Space Applications* Gianluca Allinson *et al. arXiv:2601.20631.* This chapter was developed during a secondment on a parallel project investigating Rydberg sensors for space-based applications. As such, it differs somewhat in emphasis from the predominantly experimental work presented in earlier chapters. It is included as part of the wider research carried out during this PhD and remains closely related to Rydberg atom sensors..

7.1 Introduction

In this chapter, a theoretical study on the sensitivity of EIT-based Rydberg atom sensors is undertaken, with an emphasis on breadth rather than depth. The aim here is to identify the factors that most strongly influence the performance of a *practical*

sensing system. For example, laser frequency noise which informs requirements for laser power and linewidth, rather than to provide a comprehensive exploration of the atomic physics, as other studies have attempted previously [63, 210, 64, 211, 212]. To emphasise this practical analysis, we aim to compare the sensitivities of Rydberg detectors to more traditional techniques. In doing so, we introduce the concept of noise equivalent field (NEF), a metric often used for Rydberg atom sensors, and noise temperature T_n, a standard metric in rf receiver design. This chapter does not weigh other advantages of Rydberg sensors, such as the dielectric nature or small sensor size, against traditional antennas.

Given the complexity of the problem, arising from parameter interdependencies, the large parameter space, detection frequencies, and the different methods or architectures, we structure this chapter into three parts. First, we examine the general behaviour of various noise sources for a generic representative superheterodyne Rydberg receiver operating at different detection frequencies for *fixed* temperature, cell length, beam waist and so on. Second, we investigate how sensitivity changes when the sensing region (through its length and beam waist) is scaled according to the wavelength of the detected radiation. Lastly, we see how incorporating Rydberg vapour cells into resonant structures affects the sensitivity. This framing of the problem, and the associated scaling of the sensor model, is motivated by several considerations: (i) It enables us to examine how the dominant noise processes scale largely independently of specific experimental choices; (ii) It allows a direct and fair comparison with conventional antennas, whose optimal performance typically requires physical dimensions on the order of the wavelength (e.g., $\lambda/2$ dipoles), and which therefore exhibit strong wavelength-dependent constraints on sensitivity, bandwidth, and impedance matching; (iii) It provides a natural route to understanding how Rydberg vapour cells might be embedded within resonant or quasi-resonant microwave structures, where scaling with wavelength again plays a central role. Together, these considerations motivate treating the atom-based sensor in a way that parallels traditional antennas, while highlighting the fundamentally different

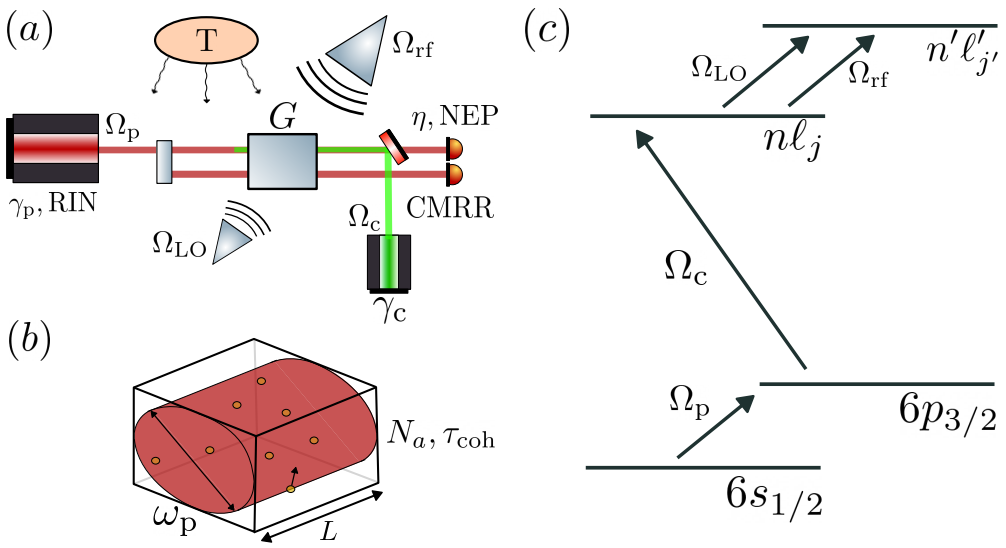

Figure 7.1: Overview of the probe measurement and the factors that determine the sensitivity. (a) Simplified experimental diagram showing the general superheterodyne two-photon scheme considered in this chapter with relevant parameters labelled next to the appropriate source. T - temperature of surroundings, G - gain of receiver, $\gamma_{\mathrm{p,c}}$ - linewidth of the probe/coupling laser, $\Omega_{\mathrm{p,\ c,\ rf,\ LO}}$ - Rabi frequency of the probe/coupling/signal/local oscillator, RIN - (laser) relative intensity noise, η - quantum efficiency of the photodiode, NEP, $\mathcal{N}$ - noise equivalent power of the photodiode, CMRR - common mode rejection ratio of the balanced detection scheme. (b) Cylindrical interaction region defined by the overlap of the probe and coupling laser within the vapour cell, ω_{p} - $1/e^2$ beam waist of the probe laser, L - path length of the laser beam through the vapour cell, N_a - number of Rydberg atoms participating in the measurement, τ_{coh} - coherence time of the atomic ensemble. (c) Energy level diagram showing the typical setup for a two-photon Rydberg heterodyne scheme in Cs using a probe laser to couple the ground state ($6s_{1/2}$) to the intermediate state ($6p_{3/2}$). A Rydberg laser is then used to couple the intermediate state to a Rydberg state ($n\ell_j$). The LO is used to drive a transition between the Rydberg states of interest to allow coherent detection of the rf signal of interest and bias the atomic vapour so that the response to the rf signal is maximised.

size–wavelength relationship offered by Rydberg receivers.

7.1.1 Probe Measurement

As we have seen previously, Rydberg EIT-based receivers measure a change in the optical probe power, P_p due to the change in the transmission of the atomic vapour. The measurement of optical power can be related to the local electric field within the region defined by the overlap of the laser beams. To determine a measure of

sensitivity, we equate the resolvable Rabi frequency, $\Delta\Omega_{\mathrm{rf}}$, (and hence electric field) of the microwave field to the effective noise floor of the photodetector signal. The optical power change, ΔP, due to a small variation in the rf Rabi frequency is then, most generally,

$$\Delta P = P_0\left(\frac{\partial \mathrm{T}(\Omega_{\mathrm{p}}, \Omega_{\mathrm{c}}, ...)}{\partial \Omega_{\mathrm{rf}}}\right)\Delta\Omega_{\mathrm{rf}}, \tag{7.1}$$

where P_0 is the *initial* power before propagating through the vapour cell, $(\frac{\partial \mathrm{T}}{\partial \Omega_{\mathrm{rf}}})$ is the 'transmission response', that is, the instantaneous change in transmission that occurs due to the incoming change in the rf signal field. The right-hand side of Eq. (7.1) represents the measured change in optical power caused by a resolvable change in Rabi frequency induced by the signal field. The sensitivity corresponds to the case where ΔP equals the noise floor, allowing us to determine the minimum detectable change in Rabi frequency, $\Delta\Omega_{\mathrm{rf}}$, and thus the smallest resolvable microwave field. For a measurement bandwidth $\Delta\nu$ the rms noise power is expressed as

$$\frac{\Delta P}{\sqrt{\Delta\nu}} = P_{n,\mathrm{PSD}}(\Omega_{\mathrm{p}}, \Omega_{\mathrm{c}}, ...). \tag{7.2}$$

Here, the LHS represents the signal amplitude in a 1 Hz bandwidth, while the right-hand side represents the total equivalent input noise in the same units. This form makes it explicit that the minimum resolvable Rabi frequency occurs when the signal-induced optical power change per $\sqrt{\mathrm{Hz}}$ equals the noise spectral density of the measurement. Determining the sensitivity then becomes an exercise in finding each independently correlated noise sources, $P_{n,\mathrm{PSD}}$, of the signal from the photodetector.

As we have done in previous chapters, the modelling assumes to be sufficiently optically thin so that a number of simplifications can be made greatly speeding up computation time. Optically thick treatments, through forms of the Maxwell-Bloch equations, in Rydberg rf sensing have been explored previously [63] however mostly with focus on a single limiting noise factor (the standard quantum limit). Another simplifying assumption we make is that the electric field is uniform throughout the vapour cell, this assumption is discussed later in the chapter when we introduce resonant structures.

For this chapter we use `rydiqule` [50] to model the atomic vapour's transmission due to its speed. In this chapter many exploratory simulations are done in order to find the parameters which minimise the total noise requiring much faster computations than the homebuilt models we used in chapter 4.

Figure 7.1 outlines the experiment that we model in this chapter. The noise analysis follows the standard approach used in superheterodyne Rydberg experiments, in which an additional microwave field acts as a local oscillator [65]. This field biases the vapour transmission to operate in the regime of maximum sensitivity to changes in the microwave signal. In our modelling, this is captured by choosing the LO field strength that maximises the sensitivity.

7.2 Noise Analysis

To quantify the sensitivity of Rydberg receivers, we use the noise-equivalent field (NEF), which expresses the smallest detectable electric field per unit bandwidth. NEF is conceptually analogous to the noise power spectral density or noise temperature, T_n used in traditional radio systems [213] which we introduce shortly.

Some recent work has attempted to relate the sensitivity metrics of Rydberg sensors to those of traditional antennas by looking at a power-based comparison [64, 214, 215]. These approaches often begin with the argument that the input power collected by an antenna from an incident electric field (peak amplitude), $|\vec{E}|$, is:

$$P = A_{\text{eff}} \frac{|\vec{E}|^2}{2Z_0} = G \frac{\lambda_0^2}{4\pi} \frac{|\vec{E}|^2}{2Z_0}, \tag{7.3}$$

where λ_0 is the free-space wavelength and $A_{\text{eff}} = G\frac{\lambda_0^2}{4\pi}$ is the effective area/aperture of the antenna with gain, G, and $Z_0 = \mu_0 c$ is the impedance of free space. From this, the electric-field sensitivity of a Rydberg sensor can be expressed in terms of an equivalent noise temperature, T, representing the input noise power, $k_B T B$, from a single thermal noise source of bandwidth, B:

$$|\vec{E}| = \sqrt{\frac{8\pi f^2}{\epsilon_0 c^3 G}} \sqrt{k_B T B}. \tag{7.4}$$

Here T denotes the effective noise temperature of a single noise source. While originally defined for thermal noise, the same framework applies to any white noise process [213] which we assume in this work. The natural analogue to the noise temperature T_n, of a conventional receiver is then the noise-equivalent field (NEF), defined as,

$$\mathrm{NEF} = \sqrt{\frac{8\pi f^2}{\epsilon_0 c^3 G}}\sqrt{k_B T_n}. \tag{7.5}$$

The NEF can be interpreted as an electric-field spectral density, conceptually equivalent to the noise power spectral density in traditional systems. In the literature, it is often defined as the minimum electric field that yields a signal-to-noise ratio of unity in a 1 Hz measurement bandwidth. In this chapter, we use NEF to quantify the noise of various sources in superheterodyne receivers, at the end of the chapter we summarise by comparing to a survey of (non-cryogenic) low-noise amplifiers (LNAs). LNAs provide a meaningful benchmark because, in conventional receivers, the LNA is the component that fundamentally determines the noise floor of the entire system and is often the first active stage after the antenna, its gain suppresses the noise contributions of all subsequent components, and its added noise directly limits the achievable sensitivity [213].

The sensing 'volume'* in a Rydberg receiver is defined by the atomic ensemble and excitation lasers. If one wanted to define a noise temperature, a limitation of this mapping is the definition of G, which is architecture dependent. It is typically discussed for electrically small detectors [110], can, in some cases, be measured from the sensing process [74], and has been treated theoretically in several works [214, 64]. In this work, where we state an equivalent T_n, we assume that $G = 3/2$ so that the Rydberg detectors are consistent with electrically small dipoles [213].

As an example, the noise temperature of a NEF $= 1\,\mu\mathrm{Vm}^{-1}\mathrm{Hz}^{-1/2}$ 10 GHz dipole receiver has approximately $T_n \approx 1{\times}10^4\,\mathrm{K}$ (NF† $= 15.5\,\mathrm{dB}$). The best demonstrated

*here referring to a physical volume, often taken to the cylindrical overlap of the excitation lasers, whereby the excited atoms take place in a measurement of electric field - not to be confused or correlated with some antenna's effective aperture

†Noise figure (NF) is an alternative measure of sensitivity with $\mathrm{NF} = 10\log_{10}(1 + \frac{T_n}{290\ \mathrm{K}})$

superheterodyne Rydberg receivers at 10 GHz are roughly around this NEF [32]. Conversely, with an NEF $\approx 1\,\mu\mathrm{Vm}^{-1}\mathrm{Hz}^{-1/2}$ for a 100 GHz dipole, this gives 100 K (NF ≈ 1.3 dB).

The total NEF of a Rydberg receiver can be separated into contributions arising from intrinsic detector noise and external environmental backgrounds [214, 216]. In this work, we define these schematically as

$$\mathrm{NEF} = \sqrt{\mathrm{NEF}_{\mathrm{ext}}^2 + \mathrm{NEF}_{\mathrm{int}}^2}, \tag{7.6}$$

where the intrinsic contribution represents noise internal to the detection process, such as photon shot noise or electronic noise, while the extrinsic contribution is used as a comparative benchmark for external backgrounds that may couple to the receiver, including black-body radiation (BBR), radio interference, or other environmental fields.

It should be noted that, while thermal electromagnetic backgrounds are naturally treated as additive noise sources in conventional antenna theory, their role in coherent Rydberg-EIT sensing is less clear. In practice, BBR primarily acts on the atomic system through incoherent transitions and dephasing processes that modify the susceptibility of the medium, rather than necessarily appearing as an independent additive noise term at the detector output. As such, the decomposition above should be regarded as a useful phenomenological framework for comparison with conventional RF receivers, rather than a complete description of the underlying noise processes in the Rydberg sensor.*

This separation will later prove convenient when considering microwave-confining structures coupled to the detector. Throughout this work, correlations between different noise mechanisms are neglected, providing a simplified and generally conservative estimate of the total sensitivity limit, although some studies have

*Here we group BBR external to the vapour cell together with thermal radiation emitted by the warm cell itself, as both contribute to the surrounding electromagnetic environment. One could alternatively regard thermal emission from the vapour cell as intrinsic to the detector platform; however, throughout this chapter it is treated as part of the external background for consistency with conventional receiver-noise terminology.

considered correlations between atomic and photon shot noise [216]. Throughout this chapter, we report NEF in terms of the *peak* electric-field amplitude unless otherwise specified as Rydberg sensors naturally measure Rabi frequency (proportional to the field amplitude). In rf literature of antenna and power relations, it is more common to use the root-mean-square (rms) value $E_{\text{rms}} = E_{\text{peak}}/\sqrt{2}$ which has also occasionally been adopted in Rydberg sensing studies [65]. This conversion is reflected in equation (7.3), where the input power to an antenna is defined as the time-averaged power corresponding to the rms electric field.

7.2.1 Extrinsic Noise

The only source of extrinsic noise considered here is the thermal electromagnetic background associated with undesired black-body radiation (BBR) incident on the Rydberg receiver. In conventional radio-frequency systems, thermal radiation occupies the same electromagnetic modes as the signal of interest and is therefore naturally associated with a background noise floor.

There is ongoing discussion regarding the precise role thermal fields play in Rydberg sensing architectures. Historically, BBR in Rydberg atoms has been well known to modify transition rates between excited states and induce ac Stark shifts [217, 218, 219]. In modern Rydberg sensing, early experimental work investigated these effects on the EIT lineshape, but did not analyse possible consequences for fluctuations in the detected probe spectrum [220]. Some treatments have drawn analogies between Rydberg receivers and conventional antennas, suggesting that thermal electromagnetic fields may contribute noise through the *variance*[*] of the field, particularly in heterodyne sensing architectures [214, 221]. More recent work has additionally highlighted the role of the spatial coherence properties of the thermal field across the vapour cell [222].

[*]Here variance refers to the statistical variance of the thermal electromagnetic field, i.e. fluctuations arising from $\langle E^2\rangle - \langle E\rangle^2$. Thermal (chaotic) light has photon-number variance $\bar{n}(\bar{n}-1)$ [60].

By contrast, other studies have argued that thermal radiation primarily acts through incoherent pumping and dephasing processes, modifying excited-state populations, linewidths, and coherences without directly generating measurable coherent dynamics in the atomic response [223, 224, 17]. In this description, the dominant effect of BBR is incorporated through effective transition and decoherence rates within the master equation governing the atomic susceptibility.

The relationship between these two viewpoints remains unclear in the context of continuously monitored Rydberg-EIT sensing. While stochastic electromagnetic fields can, in other atomic systems, imprint measurable fluctuations onto transmitted probe light [225, 226, 227], it is not yet established whether thermal background fields contribute to Rydberg receiver noise in the same manner as conventional additive noise sources. In this work, we therefore adopt a conservative phenomenological treatment in which thermal backgrounds are retained primarily as a comparative benchmark against conventional RF receiver theory, while recognising that their dominant physical effect in present Rydberg-EIT sensors is likely through decoherence and population redistribution rather than a directly measurable additive noise process. In traditional radio detection, noise due to the background BBR is described in terms of the antenna temperature [228], which provides a convenient way to separate environmental noise from the Johnson–Nyquist noise generated internally and to quantify the noise contribution from the coupling of the antenna's effective aperture with the background spectral radiance. Both are often grouped under the term 'thermal noise', as they arise from the same underlying physical process.

For traditional systems, an equivalent thermal background contribution can be estimated using the Callen–Welton expression,

$$\mathrm{NEF}_{\mathrm{ext}} = \sqrt{\frac{8\pi f^2}{\epsilon_0 c^3 G}}, \Theta(f,T), \tag{7.7}$$

where

$$\Theta(f,T) = \frac{2hf}{e^{hf/k_B T} - 1} + hf, \tag{7.8}$$

for a heterodyne measurement [214, 229]. The factor of 2 accounts for down-converted thermal noise from the image band.

Within conventional antenna theory, this expression corresponds to the thermal electromagnetic background coupled into the receiver from the surrounding environment. For example, a thermal background of 290 K would correspond to an equivalent input noise temperature of approximately 580 K at microwave frequencies. In the context of Rydberg sensing, Eq. (7.7) should therefore be regarded primarily as a comparative benchmark against traditional radio-frequency receivers, rather than as a rigorously established lower bound on the NEF of coherent Rydberg-EIT sensors.

The precise role of thermal electromagnetic backgrounds in Rydberg sensing remains an open question. In addition to inducing incoherent transitions and decoherence, black-body radiation modifies excited-state populations and probe transmission, effects which have themselves been explored for thermometric applications, for example through BBR-driven Rydberg-state transfer [75, 230, 231], Doppler-broadening measurements [232, 233], and transmission changes associated with BBR-induced decoherence [224].

In this chapter, however, we restrict our perspective to treating the thermal electromagnetic background primarily as a comparative benchmark against conventional radio-frequency receivers. This allows the performance of the Rydberg receiver to be discussed within a familiar RF noise-temperature framework, while recognising that the microscopic interaction between thermal fields and a coherent atomic sensor is more naturally described through modifications to the atomic susceptibility and decoherence rates. Since the precise relationship between these effects and measurement-level noise remains uncertain, Eq. (7.7) is retained as a phenomenological reference point rather than a complete description of the thermal-noise processes in the sensor.

A further consideration for Rydberg sensors is the thermal environment generated by

the vapour cell itself. In warm-vapour systems, the cell must typically be heated to approximately 290,K or above in order to achieve sufficient atomic density, meaning that the surrounding glass and nearby components also contribute to the local thermal electromagnetic environment. Low-emissivity materials or radiative-cooling approaches have been proposed as possible mitigation strategies [234, 235, 214], although experimental demonstrations have not yet reached sensitivities sufficient to clearly verify these effects [215]. To date, direct measurements of thermal background by reaching the associated sensitivity in Rydberg-EIT sensing have not yet been performed, however it been observed in six-wave-mixing experiments [74, 236].

7.2.2 Intrinsic Noise

In this section we will go over the mechanism of the various internal noise sources in a Rydberg receiver. At the end of the section, a discussion of the various noise sources are given. This is to put the experimental parameters in the context of the overall Rydberg receiver architecture.

7.2.2.1 Photon Shot Noise

Photon shot noise originates from the Poissonian counting statistics of photons in the probe field [60]. It sets a fundamental limit to the sensitivity of any optical detection. The corresponding noise-equivalent power (NEP) spectral density is given by:

$$\mathrm{NEP}_{\mathrm{SN}} = \sqrt{P_p h\nu_p}, \tag{7.9}$$

where P_p is the detected (average) probe power, and ν_p is the frequency of the probe laser.

To total detected probe power is directly tied to the transmission of the atomic vapour which encapsulates many (if not all) variables of the sensor. For example, changing the laser powers will change the properties of the vapour and hence the transmission or changing the length and the number of atoms in the cell (through

heating or cooling) will change the transmission. The resulting expression for the NEF due to photon shot noise is [214, 237]

$$\mathrm{NEF}_{\mathrm{psn}} = \frac{\hbar}{\mu}\sqrt{\mathrm{T}\frac{2h\nu_p}{P_0}} \cdot \left(\frac{\mathrm{dT}}{\mathrm{d}\Omega_{\mathrm{rf}}}\right)^{-1}, \tag{7.10}$$

where μ is the dipole moment of the Rydberg transition, and the derivative, $\left(\frac{\mathrm{dT}}{\mathrm{d}\Omega_{\mathrm{rf}}}\right)^{-1}$, tells us about the instantaneous change in transmission due to an incoming change in the microwave field (the signal). This will be referred to as the *transmission response* throughout this chapter. Intuitively, we want the point where the transmission changes the most due to a change in the incoming microwave (signal) field giving the largest change in measured power. This means optimising many parameters such as laser powers, cell length, temperature, microwave LO and so on. Naively, we could increase power forever to decrease the NEF, however, this results in a very large $\left(\frac{\mathrm{dT}}{\mathrm{d}\Omega_{\mathrm{rf}}}\right)^{-1}$ i.e. the vapour transmission does not change much for a change in microwave field when using very large Rabi frequencies. Note that Eq. (7.10) includes an additional factor of two compared to the generic NEP expression above. This factor arises from the conventional use of a one-sided noise spectral density when the optical shot noise is expressed in terms of the photocurrent generated at the detector.

Equation (7.10) assumes that we have a perfect photodiode. Specifically, that there is no noise associated with the photodiode and that the quantum efficiency, η, the percentage that an incoming photon is converted to electrons within the photodetector, is 100%. Typical values for quantum efficiency vary from 40% to 95% and is usually expressed as photodiode *responsivity*. The intrinsic noise on a photodetector is measured in noise equivalent power (NEP), which encapsulates the noise when there is no incident light on the detector. This is the sum of the Johnson-Nyquist noise associated with the resistance in the circuit and the dark current of the detector. Incorporating photon shot noise with a quantum efficiency and photodetector NEP into the photon shot noise we find,

$$\mathrm{NEF}_{\mathrm{psn,\ pd}} = \frac{\hbar}{\mu}\sqrt{T\frac{2h\nu_p}{\eta P_0} + \frac{\mathcal{N}^2}{P_0^2}} \cdot \left(\frac{\mathrm{dT}}{\mathrm{d}\Omega_{\mathrm{rf}}}\right)^{-1}, \tag{7.11}$$

where $\mathcal{N}$ is the NEP of the photodiode. Similarly to probe power, we could naively increase the probe power to improve the NEF, but this would affect the transmission change. For large photodiode NEPs, it may be beneficial to do this, but using typical values (10^{-15} – $10^{-12}\,\mathrm{WHz}^{-1/2}$, smaller is better), our results presented later imply we are not limited by photodiode NEP. Optical homodyne and heterodyne techniques or physically cooling the photodiode could decrease the noise from the NEP of a photodiode in the case where this is limiting [238, 214]. Additionally, use of squeezed light would reduce the shot noise associated with the amplitude measurement light [239, 240].

We consider a general two-photon experiment and minimise the total shot noise by varying the probe and coupling Rabi frequencies for a cell of fixed length and temperature detailed in Fig. 7.2(c), which shows the typical photon shot noise results, for a photodiode with no internal noise, in a Rydberg superheterodyne scheme. The results shown are for the $51s_{1/2} \rightarrow 51p_{3/2}$ microwave transition with parameters detailed in the caption of Fig. 7.2.

The results show that the NEF with minimum photon shot noise occurs around $\Omega_\mathrm{c} \approx 2\pi \times 2\,\mathrm{MHz}$ and $\Omega_\mathrm{p} \approx 2\pi \times 10\,\mathrm{MHz}$ giving NEF $\simeq 0.1\,\mu\mathrm{Vm}^{-1}/\sqrt{\mathrm{Hz}}$. The colour map shows that the sensitivity shows little variation until Ω_c is significantly reduced. Interestingly, the probe power can be increased significantly without affecting the sensitivity. This direction likely reduces the noise power from shot noise but simultaneously degrades the transmission response of the medium. We see another local minimum at higher Ω_c consistent with another analysis [234]. However, our sensitivity results are lower in comparison to [234] which can likely be attributed to the larger number density of Cs at identical temperatures. Further discussion of the variation of temperature and cell length, affecting the total optical depth, are discussed later in this chapter.

Fig. 7.2(a) shows the lineshape with this configuration of Rabi frequencies and Fig. 7.2(b) shows the transmission response as the Ω_LO is varied. We can see that for the best response, Ω_LO is not strong enough to split the lineshape as in other

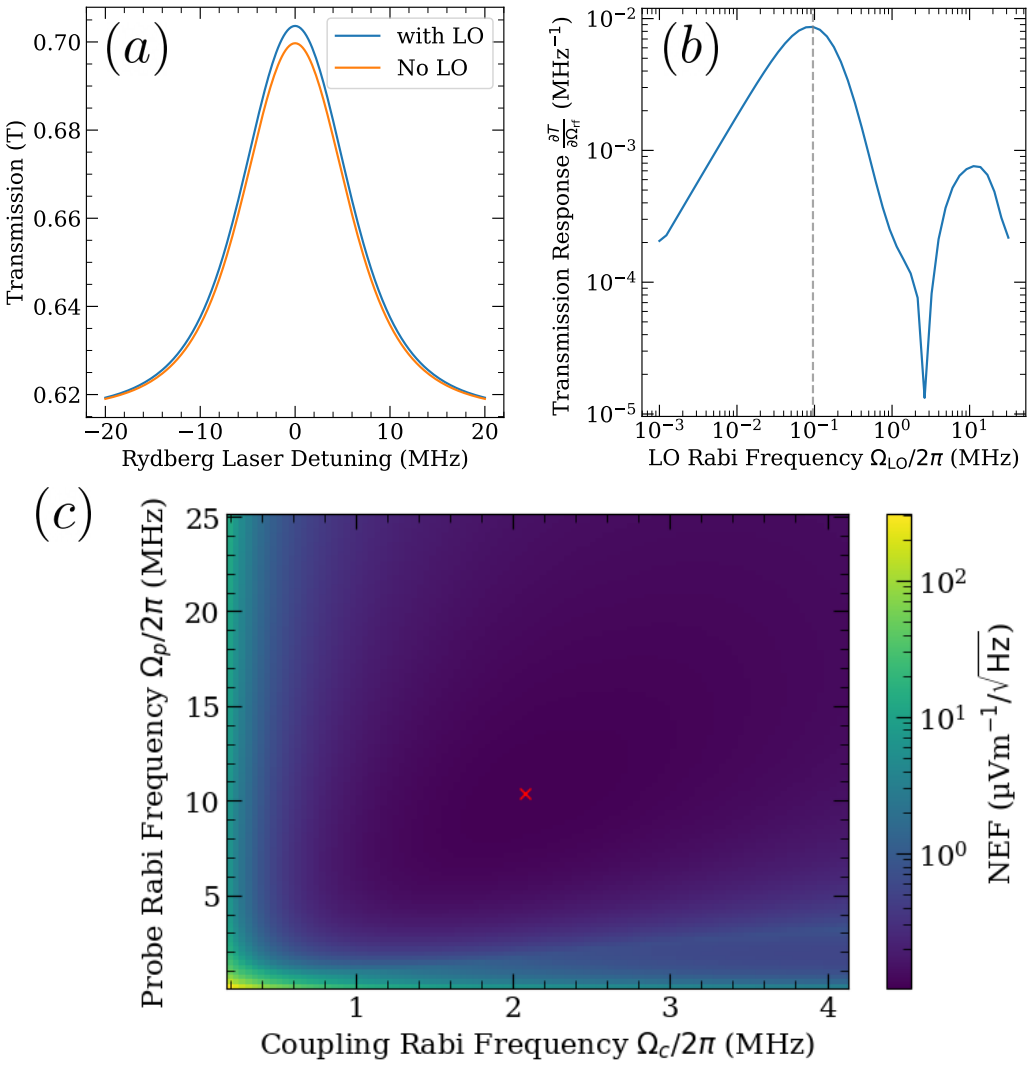

Figure 7.2: Photon shot noise for a perfect photodiode. This simulation was performed on the Cs $51s_{1/2} \rightarrow 51p_{3/2}$ (30.68 GHz) transition with a 5 mm cell at 300 K room temperature and 0.5 mm beam waists, including transit broadening and other dephasing mechanisms. (a) Typical lineshape of the EIT feature as the Rydberg (coupling) laser is scanned across resonance for the Rabi frequencies which minimise photon shot noise. This is additionally shown in the presence of the local oscillator field. (b) A plot showing the transmission response, $\frac{\partial \mathrm{T}}{\partial \Omega_{\mathrm{rf}}}$, for different values of the local oscillator Rabi frequency at the optimal probe and coupling Rabi frequencies. The dashed line shows the value which maximises the transmission response, minimising the shot noise for a particular choice of parameters. (c) A colour map showing the variation of probe and coupling Rabi frequency and the resultant limiting photon shot noise. The Rabi frequencies which maximise the sensitivity (minimise the NEF) is shown in a red cross giving $\Omega_{\mathrm{c}} = 2\pi \times 2.1\,\mathrm{MHz}$ and $\Omega_{\mathrm{p}} = 2\pi \times 10.4\,\mathrm{MHz}$.

typical works [65] but this may change depending on the many factors affecting broadening of the lineshape [210]. The second local maxima at higher Ω_{LO} reflects this choice of splitting the line.

7.2.2.2 Quantum Projection Noise

Quantum projection noise (QPN) or atom shot noise (also more generally referred to as the standard quantum limit, SQL), is the main noise source that separates Rydberg, and most quantum sensors, from their classical counterparts. QPN is an inherently quantum noise source that arises due to the measurement of a quantum state. This is common across all forms of quantum sensors or instruments and, as such, it is often seen as the analogue to Johnson–Nyquist noise in traditional detectors. In all electrical systems, there is some resistance which, at some temperature T, generates a noise power due to the thermal motion of the charge carriers. Similarly, in all quantum sensing systems, a measurement requires the collapse of a quantum state, which generates quantum projection noise [241]. This is common across all forms of quantum sensors, such as magnetometers or atomic clocks [242]. Warm Rydberg sensors represent an interesting case in comparison to most other quantum sensors. In cold systems, the long coherence time (typically ms–s) means that a single measurement can integrate information coherently over the entire interrogation period, so the projection noise scales with the total number of atoms involved in that one coherent evolution.

Warm Rydberg sensors, by contrast, have a much shorter coherence time, τ_{coh} (on the order of µs), due to decoherence from collisions and the finite transit time of atoms through the laser beam. In this regime, the total measurement interval contains many independent coherence windows, and the signal is effectively an *incoherent* sum of N separate measurements over a (much longer) interrogation time, each lasting only τ_{coh}. This fundamental difference means projection noise in warm systems is determined by the atom number within a single coherence time, and not entirely set by the integration period. The large number density afforded

by warm vapours leads to an extremely low quantum projection noise highlighting the potential, in the absence of other noise sources, as quantum sensors. It is given as [243],

$$\mathrm{NEF}_{\mathrm{qpn}} = \frac{h}{\mu}\frac{1}{\sqrt{N\tau_{\mathrm{coh}}}}, \tag{7.12}$$

where N is the number of atoms contributing to the signal (the number of excited Rydberg atoms), μ is the dipole moment of the Rydberg transition and τ_{coh} is the coherence time. This expression is only valid when the measurement time, typically $> 1\,\mathrm{ms}$, is greater than the coherence time ($<< 1\,\mu\mathrm{s}$) which is the case for superheterodyne Rydberg receivers. The coherence time has been taken from the inverse of the EIT linewidth [65] as an approximate measure, it can be more accurately calculated from the sum of the various decay processes of the atom in the required Rydberg state [216]. Namely, transit broadening, state lifetime, Rydberg-ground or Rydberg-Rydberg collisions and that limited by the laser coherence time [243]. The number of atoms participating is often naively taken to be the number density at the temperature of the vapour cell. In this modelling, we take the volume of the Rydberg sensor to be that of the cylinder formed by the two overlapping laser beams each of equal waist, ω_{p} and cell length, L. Often, numerical modelling of the Lindbladian, and subsequently the electric susceptibility, reveal that the absorption of the probe is often lower than expected. Typically, this is due to the population settling in the other hyperfine ground state and the lasers only addressing a smaller fraction of the ensemble due to the Doppler effect. This fraction, ϵ has been reported as being $\approx 1/400$ [243] or, more broadly, anywhere from 0.1%–1% [114]. These considerations give the total measurements N to be,

$$N = \epsilon n_{\mathrm{at}} \pi \omega_p^2 L. \tag{7.13}$$

Whilst the introduction of ϵ is arbitrary and gives a large range of values for N, the temperature of the vapour may be increased to further the number density n_{at}. However for high number densities, there is likely a point where the Rydberg blockade radius prevents further excitation, or causes noise induced from strong dipole-dipole interactions and collisions [210, 216].

For a generic vapour cell Rydberg receiver increasing the number of atoms is the primary method for decreasing the quantum projection noise. This can be done in a number of ways, increasing the beam waist, interaction length or increasing the temperature of the vapour. Increasing the beam waist demands larger Rydberg laser power, and increasing the length may increase the optical depth (this also ultimately depends on the probe and coupling Rabi frequency among other factors) so that little probe signal remains. Additionally, the change in temperature affects the atomic motion leading to an increase in Doppler broadening and decrease in transit times.

The dipole moment increases at higher principal quantum number where Rydberg transitions, generally, occur with lower microwave frequencies. Hence, while the quantum projection noise decreases for lower-frequency transitions, the choice of dipole moment is fixed to the sensing frequency and not under user control. This constraint, unlike adjustable parameters such as laser powers, nonetheless has a significant impact on the use case of Rydberg atom systems for microwave sensing. Similarly, the coherence time is maximal at principal quantum numbers of $n = 40$–50 [243, 114] with $\tau_{\text{coh}} \approx 10\,\mu\text{s}$ but this has little tunability with the exception of the beam waist to influence transit noise and temperature affecting blackbody induced decay rates.

Care should also be taken when mapping the projection noise limit from other quantum sensors to Rydberg sensors. The QPN, as presented by the above equation, corresponds to an idealised case where N Rydberg atoms undergo a Rabi rotation and are then measured. However, this does not accurately describe the operation of hot-vapour sensors, and therefore this QPN estimate may be incorrect in more realistic or future studies. Notably, quantum projection noise appears in hot-vapour magnetometers [244]. However, atomic magnetometers operate by continuous rotation in a magnetic field along with simultaneous measurement. On the other hand, some Rydberg sensors rely on immediate transduction rather than continuous evolution [74].

7.2.2.3 Laser Frequency Noise

Laser frequency noise refers to the resulting noise on the probe power measurement due to the frequency stability of the excitation lasers. Laser frequency must be stabilised so that it sits on resonance with the appropriate atomic energy levels. A measure of the stability of laser frequency is the laser linewidth, γ, which tells us the width of its optical spectrum. Intuitively, a small change in the laser frequency affects the electric susceptibility of the atomic ensemble, which changes the transmission of the vapour. This random instantaneous change in frequency causes a subsequent change on the measurement of the electric field. Secondarily, the laser frequency can also be treated as a decoherence term in the Lindbladian of the system. The latter treatment is included in the photon shot noise model, where changes in transmission response (due to laser linewidth) of the vapour impact the optimum Rabi frequencies and resulting limiting noise. In this section, we only consider the former as it is distinct from the noise that laser frequency noise imparts on the shot noise.

Historically, this has been studied in early atomic vapour experiments to investigate the resulting intensity noise on the probe laser [245] which was used to assess the impact on other technologies such as early Cs frequency references [246], magnetometers [247] and atomic clocks [248]. For Rydberg sensors, this noise has been qualitatively highlighted in seminal work where it was stated as the limiting noise source in their experiment [65] despite the stated single Hz level linewidths for their lasers. However, a subsequent study had shown that other noise sources, such as quantum projection noise or transit noise are likely more limiting [249]. In either case, laser frequency noise remains an important noise source as it informs the laser design architecture and ultimate size, weight and power (SWaP) requirements. To achieve certain state-of-the-art laser linewidths, ultra-stable optical cavities are needed with stringent temperature stability and vacuum requirements.

We only deal with the instantaneous change in laser frequency as oppose to drift

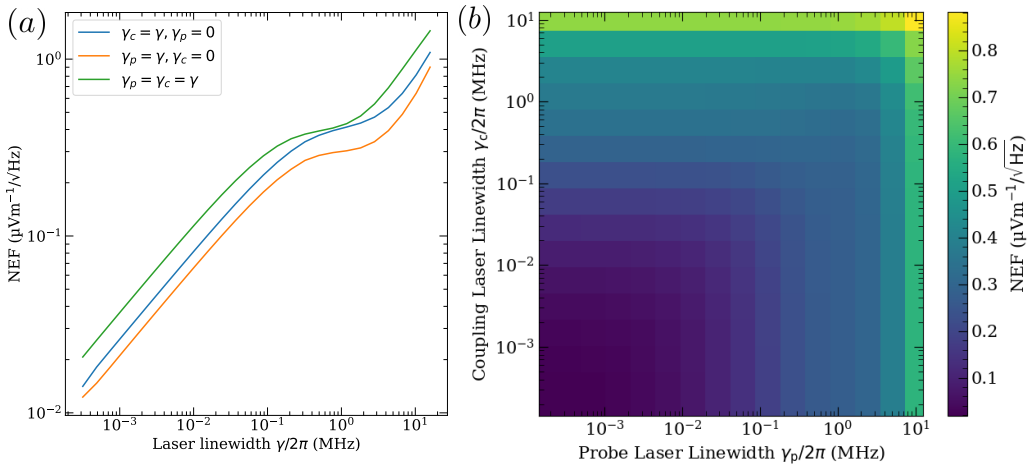

Figure 7.3: Laser Frequency Noise (a) Plot showing the variation in NEF as the laser linewidth is varied for the probe, coupling and both lasers simultaneously for the $51s \rightarrow 51p$ transition (30.68 GHz) with $\Omega_\mathrm{p} = 2\pi \times 10\,\mathrm{MHz}$ and with $\Omega_\mathrm{c} = 2\pi \times 2\,\mathrm{MHz}$. (b) Colour map showing the NEF as the probe and coupling laser linewidth are varied independently with the same parameters.

of the central frequency (i.e. the laser frequency is fixed to some stable atomic reference). In this thesis, we use the treatment given in [250]. The magnitude of noise is principally dependent on the linewidth of the laser(s) in the quantum system but is also a function of the Rabi frequencies, decay rates, and other broadening mechanisms.

The detailed derivation of the effect of laser frequency fluctuations on the measured field is provided in Appendix C, where we extend the weak-probe treatment of [250] to improve accuracy at our larger probe powers. Here, we summarise the treatment relevant to our results.

As detailed in Appendix C, an expression relating the cross-power spectral density matrix to the atomic coherences can be found. This must be evaluated for each velocity group in the atomic vapour, meaning a Doppler average is taken where each detuning, Δ_i, is modified as a result of the atomic motion. An integral similar to (2.40) can be identified, which leads to [250]:

$$\mathrm{NEF}_\mathrm{FN} = \frac{\hbar}{\mu}\left(\frac{\mathrm{d}\rho_{01}}{\mathrm{d}\Omega_\mathrm{LO}}\right)^{-1}\sqrt{4\pi S^D_{\rho_{01}}(0)}, \tag{7.14}$$

where $\left(\frac{\mathrm{d}\rho_{01}}{\mathrm{d}\Omega_\mathrm{LO}}\right)^{-1}$ is a slope factor telling us about the change in atomic coherence

(on the probe transition) due to a change in the microwave (measured) field and $S^D_{\rho_{01}}(0)$ is the Doppler averaged noise PSD at zero frequency of the atomic coherence (ρ_{01}) calculated from a stochastic analysis of the Lindbladian governing the quantum system.

We evaluate equation 7.14 for the same scenario given in Fig. 7.2 using the Rabi frequencies which minimise the photon shot noise. The results are shown in Fig. 7.3 which show the NEF of order $< 0.1\,\mu\text{Vm}^{-1}/\sqrt{\text{Hz}}$ at laser linewidths of 10 kHz which increase slowly until it is $> 1\,\mu\text{Vm}^{-1}/\sqrt{\text{Hz}}$ at MHz level laser linewidths. For the Rabi frequencies chosen here, which minimise the photon shot noise in most cases, the coupling laser linewidth gives rise to marginally more noise than the probe laser with both of similar order. Meaning it is always better to focus improving the linewidth of both lasers rather than focussing on one, as one may intuit the probe laser being more important. The magnitude of these results are consistent with other theoretical treatments [250, 212].

7.2.2.4 Laser Amplitude Noise

Laser amplitude noise refers to fluctuations ("jitter") in the optical power of both the probe and coupling lasers. Such fluctuations on the probe laser are directly measurable in the detected signal and are typically characterised by the relative intensity noise* (RIN) of the laser source. RIN is conventionally expressed as a power spectral density in units of dBc/Hz and is often specified by manufacturers at the peak or shown with the full noise power spectrum [251]. The RIN is stated as some

$$\text{RIN} = \frac{S(f)}{P^2}, \tag{7.15}$$

where $S(f)$ is the power spectral density of the power fluctuations and P is the total power. Following an analogous derivation to that used for photon shot noise, the variance in photocurrent, i, on the photodiode as a result of RIN, which we now

*some sources also group laser shot noise in with RIN

denote $\mathcal{R}$, can be written as

$$\mathrm{Var}(i) = R^2 P_\mathrm{p}^2 \int_B \mathcal{R}(f)\mathrm{d}f \approx R^2 P_\mathrm{p}^2 \mathcal{R} \Delta f, \tag{7.16}$$

where the product RP_p is the average photocurrent for a photodiode of responsivity, R, and incident power P_p. We approximate $\mathcal{R}(f)$ to be spectrally flat within the observation bandwidth leading to the intergral becoming a direct product over Δf. The NEF contribution due to RIN can be found by considering the standard error on the photocurrent, and dividing by the signal, $RP_p(\frac{\mathrm{dT}}{\mathrm{d}\Omega_\mathrm{rf}})^{-1}$, per observation bandwidth Δf;

$$\mathrm{NEF}_\mathrm{RIN} = \frac{\hbar}{\mu}\mathrm{T}\sqrt{\mathcal{R}} \cdot \left(\frac{\mathrm{dT}}{\mathrm{d}\Omega_\mathrm{rf}}\right)^{-1}, \tag{7.17}$$

where $\mathcal{R}$ denotes the RIN of the laser in linear units. Using the same experimental parameters as those minimising photon shot noise (Fig. 7.2), typical values yield $\mathrm{NEF}_\mathrm{RIN} \simeq 1\,\mu\mathrm{Vm}^{-1}/\sqrt{\mathrm{Hz}}$ for a RIN of $-115\,\mathrm{dB}$, decreasing to $\simeq 0.1\,\mu\mathrm{Vm}^{-1}/\sqrt{\mathrm{Hz}}$ for $-140\,\mathrm{dB}$.

High-frequency components of the amplitude noise can be strongly suppressed using balanced photodetection. In this configuration, the probe beam is split into two equal-power arms: one arm propagates through the vapour cell without the coupling beam, while the second arm probes the EIT medium. Subtracting the two photocurrents suppresses noise that is common to both beams. The level of cancellation is quantified by the common-mode rejection ratio (CMRR), and its effect can be included in Eq. (7.17) by replacing $\mathcal{R} \to \mathcal{R}/\mathcal{C}$, where $\mathcal{C}$ is the CMRR in linear units. For a typical CMRR of 30 dB, the resulting NEF is reduced to $\simeq 0.05\,\mu\mathrm{Vm}^{-1}/\sqrt{\mathrm{Hz}}$ when RIN is $-115\,\mathrm{dB}$.

However, balanced detection only suppresses amplitude noise within the frequency range over which the two detection channels are well matched in gain and phase response. While this is highly effective for cancelling fast RIN at kHz–MHz frequencies, it does not suppress slow power drifts occurring on ms–s timescales. These low-frequency components arise from thermal effects, slow current noise in laser drivers or fibre coupling drift. Crucially, such drift directly modulates the

atomic coherence and therefore cannot be distinguished from genuine changes in the RF-induced signal. In this respect, Rydberg-atom sensors share a direct parallel with classical microwave radiometers, where long-term gain fluctuations require careful calibration and periodic referencing to maintain absolute accuracy [228]. While balanced detection is extremely effective for suppressing fast noise, long-term amplitude stability must instead be ensured through active power stabilisation, slow feedback control, or referencing schemes.

Finally, probe laser amplitude noise also contributes indirectly to decoherence of the atomic system, in a manner analogous to laser phase noise. A recent full treatment of this effect is given in [212], where it is shown that for typical experimental parameters this contribution is well below the direct noise imparted by probe laser RIN, and even smaller for the coupling laser.

7.3 Results

Firstly, we will consider a generic experiment where the length and laser beam waists are constant (fixed volume). We will then look at a specific example where we scale the waist of the laser beams and the length of the vapour cell according to some $\simeq \lambda/2$ resonant cavity. This will become relevant later on in chapter 7.4.

Figures 7.4 and 7.5 show the intrinsic noise for experiments of different design. They use transitions of the form $ns_{1/2} \rightarrow np_{3/2}$ with principal quantum number ranging from $n = 30$–80 leading to a frequency range of $\nu = 6$–$250\,\mathrm{GHz}$. To fairly represent the noise sources, we choose values for RIN, NEP, quantum efficiency (η) which represent typical values. The parameters used in this section, unless otherwise stated, are summarised in the caption of Fig. 7.4.

There are other angular momentum transitions that have been explored for use in Rydberg rf sensing. Most notably the $\ell = 3 \rightarrow \ell = 4$ [114, 252, 115, 131, 253] (or larger ℓ [1]) transitions which have lower resonant frequencies at considerably lower principal quantum numbers. However, these configurations require three lasers

to excite to be able to excite to nf_j states, this would likely be performed from the $5d$ or $6d$ states in Cs and has been demonstrated from the $4d$ or $5d$ states in Rubidium [116, 253]. In this work, we stick to two-photon schemes for simplicity and to demonstrate limiting behaviour of the Rydberg sensor, although much of the analysis shown can be extended to a three-photon scheme. Whilst three-photon schemes have some evidence for generally improving sensitivities [237] and novel sensing schemes to negate Doppler broadening [254], they would impart additional amplitude and frequency noise from the addition of another laser (this could be mitigated by using an additional rf field instead [115]). Also worth mentioning is the caesium-specific $nd_j \rightarrow (n+1)p_j$ transitions as these are of particularly low frequency when compared to other two-photon accessible rf transitions. We use these later on in this chapter to demonstrate sensitivities over a larger frequency range allowed by solely using the $ns_{1/2} \rightarrow np_{3/2}$ set of transitions.

Fig. 7.4(a) shows the intrinsic noise and total noise for sensors across transitions of the form $ns_{1/2} \rightarrow np_{3/2}$ with principal quantum number ranging from $n = 30$–80 leading to a frequency range of $\nu = 6$–$250\,\mathrm{GHz}$. For this section, we only use the $|\Delta j| = 1$ as these have the larger dipole moments, and consider π transitions between the $m_j = 1/2$ states for simplicity.

The code first selects the appropriate $\Omega_{\mathrm{p,c}}$ which minimise the total photon shot noise (inclusive of photodetector noise) of the system, rather than select the Rabi frequencies which globally minimise the noise*. This approximation is likely suitable for two main reasons: First, the photon shot noise dominates in most cases and principally informs the laser powers that are required. Secondly, the Rabi frequencies which minimise the photon shot noise, likely also minimise the frequency noise as it is tied to the coherence gradient, which informs the transmission response, and is maximal at the same Rabi frequencies.

*This is due to the extremely long computation time (≈ 60 s per configuration) of laser frequency noise.

7.3.1 Fixed Volume Receiver

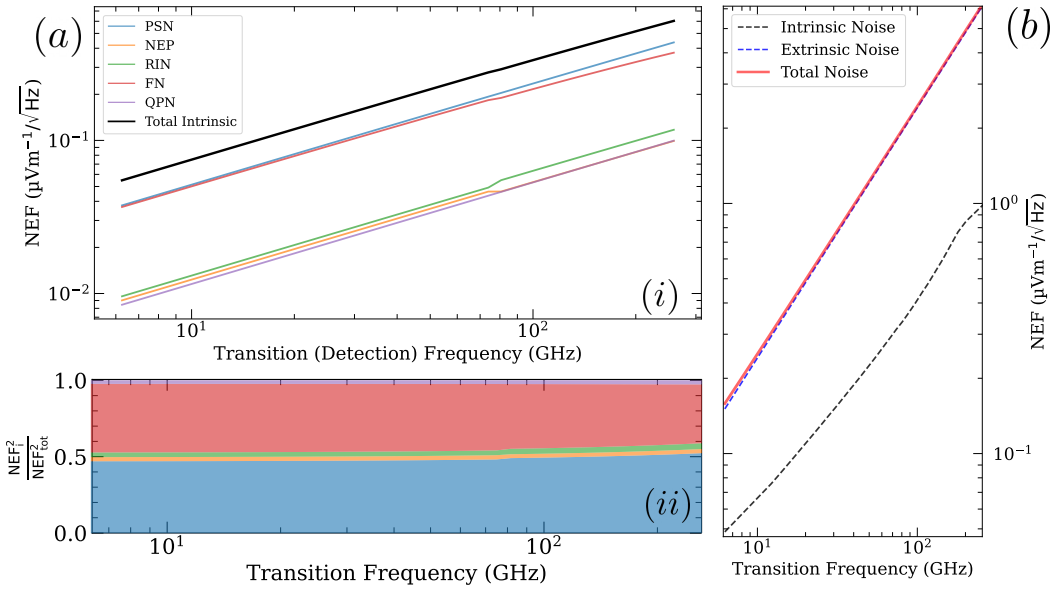

Figure 7.4: Noise Equivalent Field results for a LO-dressed Rydberg (superheterodyne) sensor with length 5 mm, beam radius 0.5 mm and temperature 300 K using $ns_{1/2} \rightarrow np_{3/2}$ transitions in Cs. The laser linewidths are $\gamma_p = \gamma_c = 2\pi \times 10\,\text{kHz}$, $\eta = 90\%$, NEP $= 1\,\text{pW}/\sqrt{\text{Hz}}$, RIN $= -120\,\text{dBc/Hz}$ and CMRR $= 30\,\text{dB}$. (a) (i) Graph showing the noise sources that make up the total intrinsic noise in the sensor. PSN - photon shot noise, NEP - noise equivalent power (of photodetector), RIN - relative intensity noise (of probe laser), FN - (laser) frequency noise, QPN - quantum projection noise (ii) A stack plot showing the squared proportions of each noise source (when added in quadrature) that contribute to the total noise source. (b) A graph showing the total NEF as a result of the extrinsic noise and intrinsic noise added in quadrature.

Fig. 7.4 shows the intrinsic noise and total noise for a Rydberg sensor where the interaction region, defined by the overlap of the two laser beams, is constant for the detection frequency. Specifically, we look at the case where the length of the beam within the vapour cell is 5 mm and the beam waist is 0.5 mm for a vapour temperature of 300 K. Figure 7.4(a) shows the components of the intrinsic noise source, which show that the photon shot noise limits the sensitivity of the Rydberg sensor at all detection frequencies. Laser frequency noise is of similar value, by coincidental choice of $\gamma_{p,c}/2\pi = 10\,\text{kHz}$, and both inversely scale with the dipole moment which decreases at higher n. However, in all cases, the laser linewidth can always be improved to further reduce the total frequency noise, whereas photon shot

noise, fundamentally, cannot be reduced indefinitely as it is tied to the transmission response of the vapour which does not improve indefinitely (without additions to the experiment [255, 211]). Quantum projection noise, NEP of the photodiode, and RIN do not meaningfully contribute with the values chosen, which represent typical values found of equipment. The floors these represent are much lower than photon shot noise but demonstrate the often-lauded extremely low noise limits imparted by QPN.

Fig. 7.4(b) is shown highlighting the difference in magnitude of the Rydberg receiver to the thermal background and the internal noise in a typical case showing that, in a perfect limit, the sensor could be limited by the thermal noise imparted by the hot glass. This of course is also common to traditional systems (where thermal noise is caused by the hot background the antenna is pointing at) but, here, the limiting thermal noise is also from the warm detector itself irrespective of where the detector is pointed at.

7.3.2 Wavelength-Scaled Volume Receiver

For a Rydberg receiver that scales with the wavelength, namely $L = \lambda/4$ and $\omega_p = \mathrm{L}/4$*. The results are shown in Fig. 7.5, where the trend of increasing NEF for increasing frequency can be understood due to a number of mechanisms, tied to the resulting incident power on the photodetector. For low frequency, and correspondingly larger wavelength, the large beam waist and cell length results in a large detected probe power. Hence, rather than photon shot noise, the noise floor is instead set by other noise sources which do not scale with the total detected probe power. Namely, the laser frequency noise. As the frequency noise strongly depends on the probe and coupling *Rabi frequencies* (which stay roughly constant), and not the resulting probe power (affected by the length, waist or number density) it is largely independent from the trend of other noise sources and chiefly set by

*These choices are somewhat arbitrary but serve to demonstrate a detector that scales with the wavelength, e.g. 30 GHz corresponds to $L = 2.5$ mm and $\omega_p = 0.6$ mm.

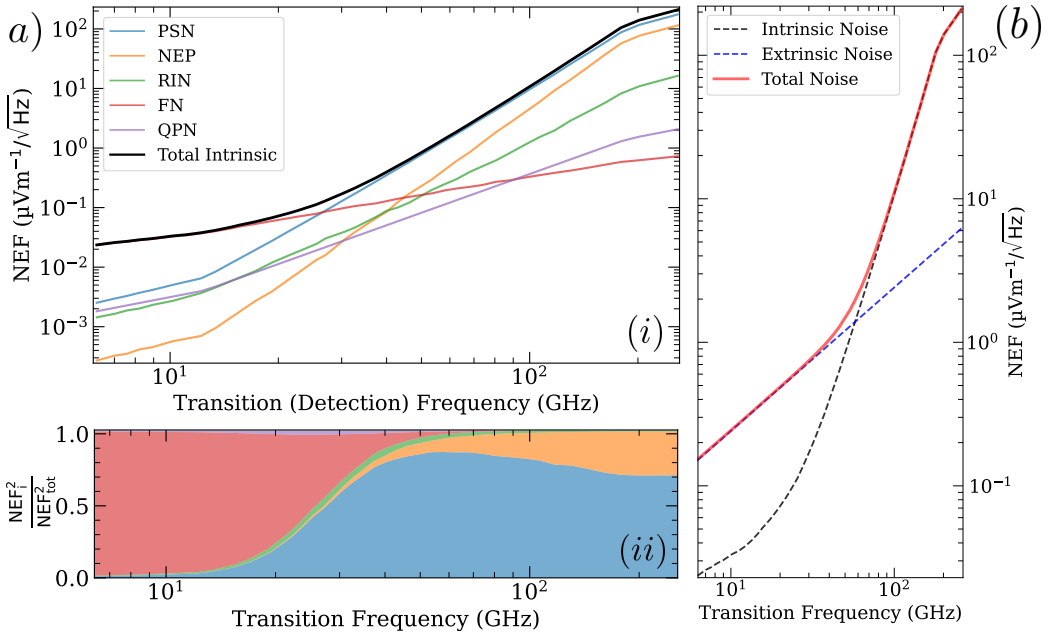

Figure 7.5: Noise Equivalent Field results for a LO-dressed Rydberg (superheterodyne) sensor with length $\lambda/4$, beam radius $\lambda/16\,\text{mm}$ (with a minimum and maximum waist of 0.1 mm and 1.5 mm respectively.) and temperature 300 K using $ns_{1/2} \rightarrow np_{3/2}$ transitions in Cs. (a)(i) Graph showing the noise sources that make up the total intrinsic noise in the sensor. PSN - photon shot noise, NEP - noise equivalent power (of photodetector), RIN - relative intensity noise (of probe laser), FN - (laser) frequency noise, QPN - quantum projection noise (ii) A stack plot showing the squared proportions of each noise source (when added in quadrature) that contribute to the total noise source. (b) A graph showing the total NEF as a result of the extrinsic noise and intrinsic noise added in quadrature.

the constant laser linewidth (and secondarily the dipole moment which decreases steadily with increasing detection frequency).

This results in the laser frequency noise dominating at lower frequencies where it is the most prominent source of source below transition frequencies of $\approx 20\,\text{GHz}$. The detected probe power at low frequencies is extremely large, due to the scaling waist, resulting in very low photon shot noise. Of course, this also sets demanding coupling power to match the large waist of the probe laser. Indeed, for a detection frequency of 9.7 GHz at $n = 73$, the waist is 1.5 mm, requiring 7 W(!) of 509 nm light to maintain the $\Omega_c = 2\pi \times 2\,\text{MHz}$ required to minimise photon shot noise. This requirement is demanding but we note that Fig. 7.2 suggests the sensitivity would not degrade substantially until $\Omega_c \lesssim 2 \times 0.6\,\text{MHz}$ — corresponding to 500 mW.

Similarly to laser frequency noise, laser maturity would remove sensitivity limits imposed by power.

The trend at higher detection frequencies is due to the poor optical depth of the vapour from reducing the excitation region of the laser beams. At 100 GHz, (e.g. the $36s_{1/2} \rightarrow 36p_{3/2}$ at 96.7 GHz) the beam waist is now 0.2 mm and an interaction length of 0.8 mm. This results in a poor optical depth afforded by the short interaction length. To compensate, the probe Rabi frequency is increased, giving a lower transmission response, a higher total transmission of the probe beam, resulting in a larger proportion of RIN. Despite the increase in Rabi frequency, the *change* in probe power detected (for a change in signal field) is very small, meaning that the NEP of the photodiode increasingly becomes a significant proportion of the noise.

Importantly, however, there is a distinction between these intrinsic noise contributions: while the NEP of the photodiode is an instrument limitation that can, in principle, be improved with better detectors, the transmission response of the vapour represents a fundamental constraint of the sensing medium. Increasing the probe power cannot arbitrarily suppress the NEP, because the atomic response itself diminishes, placing a fundamental bound on the achievable signal-to-noise ratio. The reduction in interaction volume from the geometry of the lasers also expectingly increases the noise from QPN. from the lower total number of atoms participating in the measurement. The vapour could be heated to increase the vapour density at higher frequencies allowing a larger optical depth.

As seen in figure 7.5(b), the total noise in the system is still dominated by the thermal noise at lower frequencies, approximately below 30 GHz. For high frequencies, the photon shot noise dominates due to the low optical signal power. The 'kinks' seen in the graph at approximately 10 GHz and 110 GHz are due to the 0.1 mm and 1.5 mm beam waist limit we have imposed.

7.4 Cavity-Enhanced Rydberg Receivers

Several recent studies have explored the use of microwave confinement or enhancement structures to improve the sensitivity of Rydberg atom-based [256, 257, 258, 215]. Among these, the most promising approach is the integration of Rydberg vapour cells into resonant microwave cavities [214, 215] from which this section is based upon. This configuration offers three potential advantages: (i) a reduction in extrinsic thermal noise contributions due to BBR if this were present, (ii) enhancement of the local microwave field and (ii) a well-defined receiver gain pattern. Henceforth, throughout this section, the system noise is expressed in terms of the noise temperature, T_n, rather than the noise-equivalent field (NEF), since the overall system gain is well defined when the receiver is connected to an external antenna of gain G via the cavity. and (iii) a reduction in the total thermal noise from the blackbody background via radiative cooling if present in the system.

7.4.1 Effect on Intrinsic Noise

The influence of a resonant cavity on the intrinsic noise properties of a heterodyne Rydberg receiver can be summarised by two principal effects. First, the cavity geometry constrains the maximum permissible dimensions of the vapour cell, typically on the order of a quarter wavelength ($\lambda/4$) at the operating frequency. In standard Rydberg atom experiments, the microwave field is often assumed to be spatially uniform along the optical axis. In contrast, standing-wave patterns inherent to resonant cavities produce non-uniform field distributions that can alter the observed line shapes and potentially modify the atomic response [118]. At higher frequencies ($> 30\,\mathrm{GHz}$, corresponding to $\lambda/4 < 2.5\,\mathrm{mm}$), this requirement severely restricts the physical cell dimensions and thus the laser beam waists, leading to reduced optical transmission and lower signal power. Conversely, at lower frequencies ($< 5\,\mathrm{GHz}$, $\lambda/4 > 60\,\mathrm{mm}$), the cavity becomes bulky, and the resulting large optical depth can again limit the transmitted signal. In addition, achieving sufficient optical power

and large beam waists ($> 500\,\mathrm{mW}$) at these lower frequencies increases the overall size, weight, and power (SWaP) demands of the receiver. Lastly, the resonant cavity enhances the local electric field amplitude experienced by the atoms, effectively improving the signal-to-noise ratio by the field enhancement factor determined by the cavity quality factor, Q.

7.4.2 Effect on Extrinsic Noise

By appropriate choice of cavity parameters, the introduction of a resonant cavity can also reduce the thermal noise, if this were present, associated with the physical temperature of the vapour-cell–cavity system. As we have seen, a key limitation of Rydberg receivers is that the vapour cell typically operates at room temperatures, where the resulting thermal noise often well exceeds the intrinsic noises. This limitation could, in principle, be mitigated by employing cold atoms or atomic beams. However, such configurations remain subject to ambient blackbody radiation from their surroundings, defined by an effective aperture that is not yet well characterised. Similar challenges have been addressed in other work on millimetre-wave photonic radiometers [234]. The proposed solution, directly applicable to Rydberg receivers, is to over-couple the cavity, thereby enabling radiative cooling of the cavity's thermal mode [259, 235, 234, 214]. By selecting the intrinsic quality factor Q_i and the loaded quality factor Q_c appropriately, the effective thermal noise power can be reduced. The optimal coupling condition depends on the balance between the radiative cooling and the electric field enhancement. In general, over-coupling ($C = Q_i/Q_c > 1$) provides the lowest overall noise temperature when intrinsic sensor noise is small (low $\mathrm{NEF}_{\mathrm{int}}$). This comes at the cost of a reduced field enhancement factor but yields a lower contribution from cavity thermal emission. While this principle has been demonstrated as a method of microwave field enhancement [215], experimental verification of the reduction of thermal noise in Rydberg receivers remains outstanding, and indeed the thermal noise floor in superheterodyne systems has not been observed as of yet. However,

analogous effects have been demonstrated in electro-optic converters employing similar cavity–thermal coupling mechanisms [234]. A key technical limitation observed in [215] is the degradation of the intrinsic cavity Q due to alkali-metal deposition on the vapour cell walls, an effect discussed further in [260].

7.4.3 Cavity-Enhanced Noise Temperature Results

The total noise temperature of a warm Rydberg superheterodyne receiver within a microwave cavity can be expressed following [214, 215] as the sum of three contributions: (i) the intrinsic sensor noise (photon shot noise and related effects) scaled by the cavity field enhancement factor F, (ii) the reduced thermal noise due to radiative cooling of the cavity–vapour cell system if such a noise floor were present, and (iii) the vacuum noise contribution (the quantum limit*). Explicitly,

$$T_n \approx \frac{Gc^2\epsilon_0}{8\pi f^2 k_B}\left(\frac{\mathrm{NEF_{int}}}{F}\right)^2 + \frac{1}{C}(2T_p + \frac{hf}{k_B}) + \frac{hf}{k_B}, \tag{7.18}$$

where T_p is the physical temperature of the cavity, and the enhancement factor F is determined by the cavity parameters, notably the intrinsic quality factor Q_i, the coupling factor $C = Q_i/Q_c$, and the intracavity modal volume ΔV [215]. The coupling coefficient C is optimised to minimise the total noise-equivalent temperature (NET) arising from intrinsic and extrinsic noise sources. As discussed, BBR likely does not manifest as an additional noise process in which case, the total enhancement factor F can be maximised regardless of the effect to potential thermal noise. If present however, optimal performance is achieved under over-coupled conditions ($C > 1$) as the intrinsic noise is low enough such that the thermal noise is often dominating.

Using our previous results of a wavelength-scaled Rydberg receiver and cavity parameters from reference [215], we modelled a Rydberg receiver of intrinsic noise $\mathrm{NEF_{int}}$ embedded in a cavity with $Q_i = 2000$ and an antenna gain $G = 3/2$.

*Distinct from the standard quantum limit, this refers to restrictions imposed on all linear amplifiers [261] (under the assumption that Rydberg receivers behave similarly)

Fig. 7.6 compares the predicted performance of cavity-enhanced Rydberg receivers to commercially available low-noise amplifiers (LNAs) * and those from literature [263]. The solid lines represent the total noise temperature, with dashed and dotted lines showing intrinsic and extrinsic contributions respectively. LNA data points are overlaid, with line segments denoting bandwidths where available.

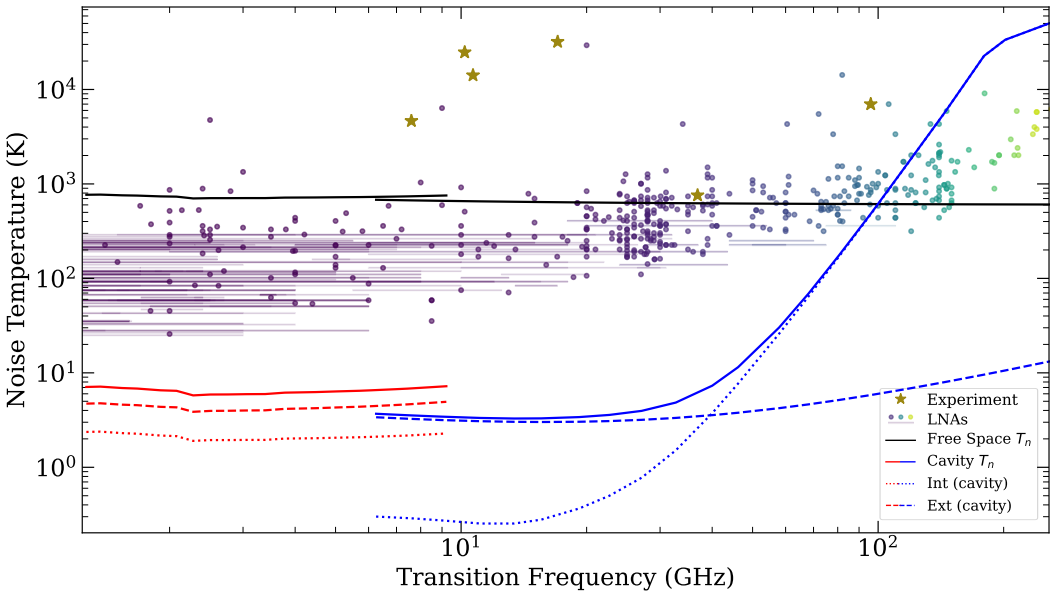

Figure 7.6: Plot of 'free space' (black) and cavity enhanced Rydberg sensitivities with the $ns \rightarrow np$ (blue) and $nd \rightarrow (n+1)p$ (red) Rydberg transitions with experimental parameters as in the previous section. Dotted lines show the intrinsic noise contribution to the noise temperature whereas the dashed line shows the contribution from the extrinsic thermal noise. A survey of low-noise amplifiers (LNAs) is shown with the data. Lines represent the bandwidth of the LNA specified, dots are shown if the bandwidth was not specified. Recent EIT-based experimental sensitivities for Rydberg sensors are shown (gold star) with an assumed gain, G = 3/2. The references for these data points are, sequentially from left to right: [264, 215, 265, 255, 216, 266].

The results indicate that a cavity-enhanced Rydberg receiver can theoretically achieve noise temperatures lower than those of most commercial LNAs across 1–300 GHz. Crucially, this is only allowed via the use of cavities to reduce the potentially large thermal noise imparted by the cell. This is reflected in the free-space results showing a near-constant line at ≃600 K regardless of detection frequency. Inspection of the free space sensitivities without the noise contributed by black-body

*Those available from *Mini-Circuits* [262].

radiation show that they are well below this value and, interestingly, decrease with increasing detection frequency. Again the use of T_n here is approximate at best as we have no way of fixing G. However, recall these intrinsic sensitivities ranging from 10^{-1}–$10^{0}\,\mu\mathrm{Vm}^{-1}/\sqrt{\mathrm{Hz}}$ with the thermal noise being an order of magnitude greater. This configuration interestingly shows promise for higher frequencies ($> 60\,\mathrm{GHz}$) where traditional LNAs have much larger noise temperatures. In this frequency region, the introduction of a cavity only reduces the sensitivity by its imposition of reducing the beam waists and cell length (But would fix the antenna aperture of the detector if needed for application).

Below 60 GHz, the results show that the sensitivities are well below those of LNAs giving noise temperatures of 10–100 K staying roughly constant. The sensitivity does not increase indefinitely with decreasing frequency largely due to the unaffected laser frequency noise which we have kept at a 10 kHz linewidth.

7.5 Discussion

It is important to remind the reader, however, that the Rydberg receiver operates only over discrete frequency bands (typically $\sim 10\,\mathrm{MHz}$ wide), which become more sparsely distributed at higher frequencies. Residual noise mechanisms such as atomic transit noise not treated in this chapter, identified in previous studies [249], may ultimately limit achievable performance but are expected to be further suppressed by cavity confinement.

The integration of a microwave cavity into a Rydberg receiver introduces several technical challenges relevant to atomic spectroscopy. Practical implementations therefore require cavity tunability on the order of hundreds of megahertz to ensure resonance with the desired atomic transition. Although the atomic transition frequency can be known to within a few megahertz, the cavity resonance may shift due to the dielectric loading introduced by the vapour cell. The physical

construction of the cavity must accommodate the vapour cell, typically with wall thicknesses of approximately 1 mm.

7.5.1 Optical Depth and Sensitivity

We have not fully explored each parameter due to brevity but we note that varying temperature (and less similarly cell length) represents an interesting case. In most scenarios, the temperature of the vapour cell can be increased to drastically increase the number density of atoms that take part in the EIT sensing process. This in turn would increase the total optical depth when calculating the transmission of the medium. As seen in another sensitivity analysis [63], this would improve the sensitivity of the detector whilst also increasing the necessary probe and coupling laser powers (by necessitating increased Rabi frequencies). This is due to the increased temperature causing a reduction in the transmission response (from Doppler broadening, transit broadening etc.) of the medium, and the larger transmission causing a reduction in signal power reaching the photodiode (for constant Rabi frequencies). Both effects, therefore, requiring larger probe power to reduce the shot noise.

However, the temperature may be increased so that no transmission remains or that transit noise becomes dominating. Contrastingly, the increase in temperature may compensate for the reduction in cell length and beam waists to get larger optical depths, a larger signal probe power, and, hence, lower shot noise.

Therefore, increasing the temperature represents an interesting case but likely does not overall improve the sensitivity. Experimentally, intrinsic noises are still limiting [32] and varying temperature represents a case to further explore depending on the demonstration's limiting noise sources.

7.6 Conclusion

This chapter modelled various noise sources impacting performance, intrinsic to Rydberg EIT-based detectors (e.g. photon shot noise) to better understand practical limits and factors affecting the sensitivities of Rydberg sensors. Free-space Rydberg receivers, using a glass vapour cell to directly sense the microwave field, show theoretical intrinsic noise temperatures that are competitive with LNAs at millimeter-wave frequencies ($\simeq$100 K at 100 GHz). However, performance can be limited by thermal background radiation from the warm vapour cell (>300 K) and the sensor's non-directive nature.

Cavity-enhanced Rydberg receivers, with the vapour cell enclosed in a resonant structure, offer substantial theoretical advantages. Cavities can enhance the signal field (reducing intrinsic noise impact). These systems theoretically could achieve noise temperatures of 10–1000 K, significantly lower than state-of-the-art LNAs across 1 GHz to 300 GHz.

Despite promising theoretical noise temperatures, achieving these predicted low sensitivities in experiment has not been demonstrated. Current results ($\simeq$800 K for cold atoms [216], $\simeq$4000 K for warm vapour EIT sensors [266]) are well above theoretical projections.

Chapter 8

Conclusion and Outlook

In this thesis, we have explored the physics arising from a novel two-photon coupling scheme that accesses high-angular-momentum Rydberg states in a warm atomic vapour. This approach has been applied in two distinct contexts. First, as a means of enabling Rydberg atoms to function as a broadband microwave sensor, and second, as a spectroscopic tool to study the structure of highly excited states in caesium. Together, these results demonstrate both the applied potential of Rydberg-based quantum sensors and their utility as a probe of fundamental atomic properties. The regular structure of adjacent high-angular-momentum Rydberg manifolds, combined with the ability to couple transitions using comparatively low radio frequencies, produces a system that shares similarities with Jaynes–Cummings and synthetic-dimension style models [267, 268]. While this thesis has focused primarily on spectroscopy and sensing applications, future studies could investigate whether control over these manifolds enables the simulation of engineered Hamiltonians or transport-like dynamics in synthetic state-space lattices.

The method introduced in Chapter 4 provides a new route to coupling successive states with considerably lower radio frequencies, and further work could investigate its sensitivity limits relative to more established Rydberg sensing techniques. A full characterisation of how prior fields influence successive transitions would help quantify the ultimate usefulness of this scheme in more applied contexts. Since the coupling architecture naturally spans many neighbouring Rydberg states, it may also provide a route toward broadband or frequency-agile quantum receivers operating across wider spectral regions than conventional resonant schemes. At the same time, several broader practical questions remain open. In particular, it is not yet clear whether accessing lower-frequency transitions at lower principal quantum numbers ultimately provides a net advantage when additional rf preparation fields are required to reach the high-ℓ states. This consideration becomes especially relevant in applications where Rydberg sensors are attractive because of their intrinsically dielectric and low-profile nature, ideally requiring minimal auxiliary electronics or antenna structures. A possible compromise may involve operating at moderately higher n while retaining some of the reduced-frequency advantages demonstrated here. However, the ability to link widely separated frequency scales may also motivate future studies of multiband sensing architectures based on Rydberg systems and generally in a wider rf sensing context. Ultimately, the value of such trade-offs will likely depend strongly on the intended application.

The spectroscopic methods developed in Chapters 5 and 6 could also be extended through the use of broadband rf or THz sources, or by employing tunable lasers that cover a wider wavelength range to access additional Rydberg states. While the high-ℓ transition measurements presented here already constrain the core polarisability of caesium, future progress will likely come from improved theoretical modelling of the core contribution. The data provided in this thesis will therefore remain valuable as more refined models of the ionic core become available. In addition, the large spatial extent and strong interactions associated with high-ℓ Rydberg states suggest possible future studies of collision processes and state-mixing dynamics in warm

vapours, where comparatively little experimental work has yet been performed [269].

Our noise and sensitivity analysis, presented in Chapter 7, is not exhaustive but offers a framework for understanding the principal mechanisms that limit Rydberg receiver performance. Further work could incorporate additional noise sources. The aim here was to identify which mechanisms are most constraining and to assess how these might guide the future development of Rydberg-based field sensors. Sensitivity, however, represents only one of several important characteristics. Rydberg receivers also offer other advantages, such as their inherently dielectric nature and their potential for absolute self-calibration beyond the reach of traditional electronic sensors. The interplay between bandwidth, sensitivity, and these other advantages ultimately determine the niche in which Rydberg receivers offer over conventional technologies.

Overall, this thesis has shown that Rydberg-based quantum sensors, while not yet matching state-of-the-art sensitivities, possess distinctive capabilities that complement and expand existing technologies rather than replace them. More broadly, the high-ℓ coupling methods explored here provide a flexible experimental *platform* that connects precision spectroscopy, quantum sensing, and driven-state quantum physics. The results presented in this thesis therefore contribute not only to the development of Rydberg electromagnetic sensing, but also to future studies of highly excited atomic systems, synthetic quantum structures, and coherent multilevel dynamics in warm atomic vapours.

Bibliography

[1] Gianluca Allinson, Matthew J Jamieson, Andrew R Mackellar, Lucy Downes, C Stuart Adams, and Kevin J Weatherill. Simultaneous multiband radio-frequency detection using high-orbital-angular-momentum states in a rydberg-atom receiver. *Physical Review Research*, 6(2):023317, 2024. Cited on pages viii, 55, 61, 64, 66, 71, and 127.

[2] Gianluca Allinson, Lucy A Downes, C Stuart Adams, and Kevin J Weatherill. Determination of quantum defects and core polarizability of atomic cesium via terahertz and radio-frequency spectroscopy in thermal vapor. *Physical Review A*, 111(6):062802, 2025. Cited on pages viii, 71, 74, 76, 83, 85, 86, 88, 91, 97, and 102.

[3] Jonathan P Dowling and Gerard J Milburn. Quantum technology: the second quantum revolution. *Philosophical Transactions of the Royal Society of London. Series A: Mathematical, Physical and Engineering Sciences*, 361(1809):1655–1674, 2003. Cited on page 1.

[4] Antonio Acín, Immanuel Bloch, Harry Buhrman, Tommaso Calarco, Christopher Eichler, Jens Eisert, Daniel Esteve, Nicolas Gisin, Steffen J Glaser,

Fedor Jelezko, et al. The quantum technologies roadmap: a european community view. *New Journal of Physics*, 20(8):080201, 2018. Cited on page 1.

[5] Christian L Degen, Friedemann Reinhard, and Paola Cappellaro. Quantum sensing. *Reviews of modern physics*, 89(3):035002, 2017. Cited on pages 1 and 72.

[6] Luca Pezze, Augusto Smerzi, Markus K Oberthaler, Roman Schmied, and Philipp Treutlein. Quantum metrology with nonclassical states of atomic ensembles. *Reviews of Modern Physics*, 90(3):035005, 2018. Cited on page 1.

[7] Zhong-Kun Hu, Bu-Liang Sun, Xiao-Chun Duan, Min-Kang Zhou, Le-Le Chen, Su Zhan, Qiao-Zhen Zhang, and Jun Luo. Demonstration of an ultrahigh-sensitivity atom-interferometry absolute gravimeter. *Physical Review A—Atomic, Molecular, and Optical Physics*, 88(4):043610, 2013. Cited on page 2.

[8] Yannick Bidel, Nassim Zahzam, Alexandre Bresson, Cédric Blanchard, Malo Cadoret, Arne V Olesen, and René Forsberg. Absolute airborne gravimetry with a cold atom sensor. *Journal of Geodesy*, 94(2):20, 2020. Cited on page 2.

[9] Remi Geiger, Arnaud Landragin, Sébastien Merlet, and Franck Pereira Dos Santos. High-accuracy inertial measurements with cold-atom sensors. *AVS Quantum Science*, 2(2), 2020. Cited on page 2.

[10] Hidetoshi Katori. Optical lattice clocks and quantum metrology. *Nature Photonics*, 5(4):203–210, 2011. Cited on page 2.

[11] Alexander Aeppli, Kyungtae Kim, William Warfield, Marianna S Safronova, and Jun Ye. Clock with 8× 10-19 systematic uncertainty. *Physical Review Letters*, 133(2):023401, 2024. Cited on page 2.

[12] Mason C Marshall, Daniel A Rodriguez Castillo, Willa J Arthur-Dworschack, Alexander Aeppli, Kyungtae Kim, Dahyeon Lee, William Warfield, Joost

Hinrichs, Nicholas V Nardelli, Tara M Fortier, et al. High-stability single-ion clock with 5.5× 10-19 systematic uncertainty. *Physical Review Letters*, 135(3):033201, 2025. Cited on page 2.

[13] Andrew D Ludlow, Martin M Boyd, Jun Ye, Ekkehard Peik, and Piet O Schmidt. Optical atomic clocks. *Reviews of Modern Physics*, 87(2):637–701, 2015. Cited on page 2.

[14] Dmitry Budker and Michael Romalis. Optical magnetometry. *Nature physics*, 3(4):227–234, 2007. Cited on page 2.

[15] Anthony P Colombo, Tony R Carter, Amir Borna, Yuan-Yu Jau, Cort N Johnson, Amber L Dagel, and Peter DD Schwindt. Four-channel optically pumped atomic magnetometer for magnetoencephalography. *Optics express*, 24(14):15403–15416, 2016. Cited on page 2.

[16] Rui Zhang, Emmanuel Klinger, Felipe Pedreros Bustos, Alexander Akulshin, Hong Guo, Arne Wickenbrock, and Dmitry Budker. Stand-off magnetometry with directional emission from sodium vapors. *Physical Review Letters*, 127(17):173605, 2021. Cited on page 2.

[17] Thomas F. Gallagher. *Rydberg Atoms*. Cambridge Monographs on Atomic, Molecular and Chemical Physics. Cambridge University Press, 1994. Cited on pages 2, 5, 7, 9, 92, and 114.

[18] Charles S Adams, Jonathan D Pritchard, and James P Shaffer. Rydberg atom quantum technologies. *Journal of Physics B: Atomic, Molecular and Optical Physics*, 53(1):012002, 2019. Cited on pages 2, 7, 57, and 58.

[19] Mark Saffman, Thad G Walker, and Klaus Mølmer. Quantum information with rydberg atoms. *Reviews of modern physics*, 82(3):2313–2363, 2010. Cited on page 2.

[20] TF Gallagher and WE Cooke. The detection of 300° k blackbody radiation with rydberg atoms. *Applied Physics Letters*, 34(6):369–371, 1979. Cited on page 3.

[21] Theodore W Ducas, William P Spencer, A Ganesh Vaidyanathan, William H Hamilton, and Daniel Kleppner. Detection of far-infrared radiation using rydberg atoms. *Applied Physics Letters*, 35(5):382–384, 1979. Cited on page 3.

[22] H___ Figger, G Leuchs, R Straubinger, and H Walther. A photon detector for submillimetre wavelengths using rydberg atoms. *Optics Communications*, 33(1):37–41, 1980. Cited on page 3.

[23] Andreas Osterwalder and Frédéric Merkt. Using high rydberg states as electric field sensors. *Physical review letters*, 82(9):1831, 1999. Cited on page 3.

[24] Marcel Drabbels and LD Noordam. Infrared imaging camera based on a rydberg atom photodetector. *Applied physics letters*, 74(13):1797, 1999. Cited on page 3.

[25] A Gürtler, AS Meijer, and WJ van der Zande. Imaging of terahertz radiation using a rydberg atom photocathode. *Applied physics letters*, 83(2):222–224, 2003. Cited on page 3.

[26] AK Mohapatra, TR Jackson, and C. S. Adams. Coherent optical detection of highly excited rydberg states using electromagnetically induced transparency. *Physical review letters*, 98(11):113003, 2007. Cited on pages 3, 19, 51, 52, and 57.

[27] Ashok K Mohapatra, Mark G Bason, Björn Butscher, Kevin J Weatherill, and Charles S Adams. A giant electro-optic effect using polarizable dark states. *Nature physics*, 4(11):890–894, 2008. Cited on pages 3, 19, and 57.

[28] Mark George Bason, M Tanasittikosol, A Sargsyan, AK Mohapatra, D Sarkisyan, RM Potvliege, and CS Adams. Enhanced electric field sensitivity

of rf-dressed rydberg dark states. *New Journal of Physics*, 12(6):065015, 2010. Cited on page 3.

[29] Jonathon A. Sedlacek, Arne Schwettmann, Harald Kuebler, Robert Loew, Tilman Pfau, and James P. Shaffer. Microwave electrometry with rydberg atoms in a vapour cell using bright atomic resonances. *Nature Physics*, 8(11):819–824, NOV 2012. Cited on pages 3, 21, 57, and 72.

[30] Joshua A Gordon, Christopher L Holloway, Steve Jefferts, and Tom Heavner. Quantum-based si traceable electric-field probe. In *2010 IEEE International Symposium on Electromagnetic Compatibility*, pages 321–324. IEEE, 2010. Cited on page 3.

[31] C. L. Holloway, J. A. Gordon, S. Jefferts, T. Heavner, D. Anderson, A. Schwarzkopf, and G. Raithel. Broadband rydberg atom-based electric-field probe for si-traceable, self-calibrated measurements. *Nature Physics*, 9:435–441, 2013. Cited on page 3.

[32] Noah Schlossberger, Nikunjkumar Prajapati, Samuel Berweger, Andrew P Rotunno, Alexandra B Artusio-Glimpse, Matthew T Simons, Abrar A Sheikh, Eric B Norrgard, Stephen P Eckel, and Christopher L Holloway. Rydberg states of alkali atoms in atomic vapour as si-traceable field probes and communications receivers. *Nature Reviews Physics*, 6(10):606–620, 2024. Cited on pages 4, 57, 70, 112, and 138.

[33] N. Šibalić, J.D. Pritchard, C.S. Adams, and K.J. Weatherill. Arc: An open-source library for calculating properties of alkali rydberg atoms. *Computer Physics Communications*, 220:319–331, 2017. Cited on pages 4, 12, 14, 69, and 72.

[34] C.J. Foot. *Atomic Physics*. Oxford Master Series in Physics. Oxford University Press, 2005. Cited on pages 5, 9, 12, 15, 17, and 22.

[35] David J Griffiths and Darrell F Schroeter. *Introduction to quantum mechanics*. Cambridge university press, 2018. Cited on page 6.

[36] Johann Jakob Balmer. Notiz über die spectrallinien des wasserstoffs. *Annalen der physik*, 261(5):80–87, 1885. Cited on page 6.

[37] Johannes Robert Rydberg. Recherches sur la constitution des spectres d'émission des éléments chimiques. *Kungliga vetenskapsakademiens handlingar*, 23(11), 1890. Cited on page 6.

[38] Johannes Robert Rydberg. Xxxiv. on the structure of the line-spectra of the chemical elements. *The London, Edinburgh, and Dublin philosophical magazine and journal of science*, 29(179):331–337, 1890. Cited on page 6.

[39] Hans A Bethe and Edwin E Salpeter. *Quantum mechanics of one-and two-electron atoms*. Springer Science & Business Media, 2013. Cited on pages 6, 7, 8, 14, and 94.

[40] Richard R. Freeman and Daniel Kleppner. Core polarization and quantum defects in high-angular-momentum states of alkali atoms. *Phys. Rev. A*, 14:1614–1619, Nov 1976. Cited on pages 11, 92, 96, and 103.

[41] M Marinescu, HR Sadeghpour, and A Dalgarno. Dispersion coefficients for alkali-metal dimers. *Physical Review A*, 49(2):982, 1994. Cited on pages 11, 93, and 103.

[42] Chris H Greene and Mireille Aymar. Spin-orbit effects in the heavy alkaline-earth atoms. *Physical Review A*, 44(3):1773, 1991. Cited on page 11.

[43] RM Sternheimer, JE Rodgers, and TP Das. Effect of the atomic core on the fine-structure splitting for excited nd and nf states of the alkali-metal atoms. *Physical Review A*, 17(2):505, 1978. Cited on page 12.

[44] J. T. M. Walraven. Atomic physics: Lecture notes. Online lecture notes (unpublished), 2025. PDF available at `https:`

//staff.fnwi.uva.nl/j.t.m.walraven/walraven/Publications_files/2025-AtomicPhysics-online.pdf, accessed 2025-11-14. Cited on pages 12, 13, and 14.

[45] Jun John Sakurai and Jim Napolitano. *Modern quantum mechanics*. Cambridge University Press, 2020. Cited on pages 14 and 15.

[46] Marcis Auzinsh, Dmitry Budker, and Simon Rochester. *Optically polarized atoms: understanding light-atom interactions*. Oxford University Press, 2010. Cited on page 16.

[47] Daniel A. Steck. Quantum and atom optics. Revision 0.16.6. Cited on pages 16 and 21.

[48] Daniel Manzano. A short introduction to the lindblad master equation. *Aip advances*, 10(2), 2020. Cited on page 16.

[49] Lucy Downes. Simple python tools for modelling few-level atom-light interactions. *Journal of Physics B: Atomic, Molecular and Optical Physics*, 56(22):223001, oct 2023. Cited on pages 17, 62, and 76.

[50] Benjamin N. Miller, David H. Meyer, Teemu Virtanen, Christopher M. O'Brien, and Kevin C. Cox. Rydiqule: A graph-based paradigm for modeling rydberg and atomic sensors. *Computer Physics Communications*, 294:108952, 2024. Cited on pages 17, 77, and 110.

[51] K Wodkiewicz. Stochastic incoherences of optical bloch equations. *Physical Review A*, 19(4):1686, 1979. Cited on page 18.

[52] Ran Finkelstein, Samir Bali, Ofer Firstenberg, and Irina Novikova. A practical guide to electromagnetically induced transparency in atomic vapor. *New Journal of Physics*, 25(3):035001, 2023. Cited on pages 18 and 19.

[53] K-J Boller, A Imamoğlu, and Stephen E Harris. Observation of electromagnetically induced transparency. *Physical Review Letters*, 66(20):2593, 1991. Cited on page 19.

[54] Sarah Mauger, James Millen, and MPA Jones. Spectroscopy of strontium rydberg states using electromagnetically induced transparency. *Journal of Physics B: Atomic, Molecular and Optical Physics*, 40(22):F319, 2007. Cited on page 19.

[55] M Tanasittikosol, J D Pritchard, D Maxwell, A Gauguet, K J Weatherill, R M Potvliege, and C S Adams. Microwave dressing of rydberg dark states. *Journal of Physics B: Atomic, Molecular and Optical Physics*, 44(18):184020, sep 2011. Cited on page 19.

[56] Haoquan Fan, Santosh Kumar, Jonathon Sedlacek, Harald Kübler, Shaya Karimkashi, and James P. Shaffer. Atom based rf electric field sensing. *Journal of Physics B: Atomic, Molecular and Optical Physics*, 48:202001, 2015. Cited on page 19.

[57] Jonathan P Marangos. Electromagnetically induced transparency. *Journal of modern optics*, 45(3):471–503, 1998. Cited on page 19.

[58] Irina Novikova, Ronald L Walsworth, and Yanhong Xiao. Electromagnetically induced transparency-based slow and stored light in warm atoms. *Laser & Photonics Reviews*, 6(3):333–353, 2012. Cited on page 20.

[59] Stanley H Autler and Charles H Townes. Stark effect in rapidly varying fields. *Physical Review*, 100(2):703, 1955. Cited on page 21.

[60] Rodney Loudon. *The quantum theory of light*. OUP Oxford, 2000. Cited on pages 21, 113, and 116.

[61] Julio Gea-Banacloche, Yong-qing Li, Shao-zheng Jin, and Min Xiao. Electromagnetically induced transparency in ladder-type inhomogeneously broadened

media: Theory and experiment. *Phys. Rev. A*, 51:576–584, Jan 1995. Cited on page 22.

[62] Robert W Boyd, Alexander L Gaeta, and Enno Giese. Nonlinear optics. In *Springer Handbook of Atomic, Molecular, and Optical Physics*, pages 1097–1110. Springer, 2008. Cited on pages 22, 32, and 38.

[63] David H Meyer, Christopher O'Brien, Donald P Fahey, Kevin C Cox, and Paul D Kunz. Optimal atomic quantum sensing using electromagnetically-induced-transparency readout. *Physical Review A*, 104(4):043103, 2021. Cited on pages 22, 107, 109, and 138.

[64] Peter B Weichman. Doppler sensitivity and resonant tuning of rydberg atom-based antennas. *Journal of Physics B: Atomic, Molecular and Optical Physics*, 57(16):165501, 2024. Cited on pages 22, 107, 110, and 111.

[65] Mingyong Jing, Ying Hu, Jie Ma, Hao Zhang, Linjie Zhang, Liantuan Xiao, and Suotang Jia. Atomic superheterodyne receiver based on microwave-dressed rydberg spectroscopy. *Nature Physics*, 16(9):911–915, Sep 2020. Cited on pages 24, 72, 110, 113, 120, 121, and 123.

[66] Joshua A. Gordon, Matthew T. Simons, Abdulaziz H. Haddab, and Christopher L. Holloway. Weak electric-field detection with sub-1 Hz resolution at radio frequencies using a Rydberg atom-based mixer. *AIP Advances*, 9(4):045030, 04 2019. Cited on page 24.

[67] Matthew T. Simons, Abdulaziz H. Haddab, Joshua A. Gordon, and Christopher L. Holloway. A Rydberg atom-based mixer: Measuring the phase of a radio frequency wave. *Applied Physics Letters*, 114(11):114101, 03 2019. Cited on page 24.

[68] J. A. Sedlacek, A. Schwettmann, H. Kubler, and J. P. Shaffer. Atom-based vector microwave electrometry using rubidium rydberg atoms in a vapor cell. *Physical Review Letters*, 111(6), AUG 6 2013. Cited on page 24.

[69] Amy K. Robinson, Nikunjkumar Prajapati, Damir Senic, Matthew T. Simons, and Christopher L. Holloway. Determining the angle-of-arrival of a radio-frequency source with a Rydberg atom-based sensor. *Applied Physics Letters*, 118(11):114001, 03 2021. Cited on page 24.

[70] David H Meyer, Joshua C Hill, Paul D Kunz, and Kevin C Cox. Simultaneous multiband demodulation using a rydberg atomic sensor. *Physical Review Applied*, 19(1):014025, 2023. Cited on pages 24 and 59.

[71] Maitreyi Jayaseelan, Andrew P. Rotunno, Nikunjkumar Prajapati, Samuel Berweger, Alexandra B. Artusio-Glimpse, Matthew T. Simons, and Christopher L. Holloway. Electromagnetically-induced-transparency spectra of rydberg atoms dressed with dual-tone radio-frequency fields. *Phys. Rev. A*, 108:033712, Sep 2023. Cited on page 24.

[72] Lucy A. Downes, Andrew R. MacKellar, Daniel J. Whiting, Cyril Bourgenot, Charles S. Adams, and Kevin J. Weatherill. Full-field terahertz imaging at kilohertz frame rates using atomic vapor. *Phys. Rev. X*, 10:011027, Feb 2020. Cited on page 24.

[73] Nikunjkumar Prajapati and et al. Investigation of fluorescence versus transmission readout for three-photon rydberg excitation used in electrometry. *AVS Quantum Science*, 6(3), 2024. Cited on page 24.

[74] Sebastian Borówka, Uliana Pylypenko, Mateusz Mazelanik, and Michał Parniak. Continuous wideband microwave-to-optical converter based on room-temperature rydberg atoms. *Nature Photonics*, 18(1):32–38, 2024. Cited on pages 24, 111, 116, and 122.

[75] Noah Schlossberger, Andrew P Rotunno, Stephen P Eckel, Eric B Norrgard, Dixith Manchaiah, Nikunjkumar Prajapati, Alexandra B Artusio-Glimpse, Samuel Berweger, Matthew T Simons, Dangka Shylla, et al. Primary quantum thermometry of mm-wave blackbody radiation via induced state transfer in

rydberg states of cold atoms. *Physical Review Research*, 7(1):L012020, 2025. Cited on pages 24 and 115.

[76] Peter H Siegel. Terahertz technology. *IEEE Transactions on microwave theory and techniques*, 50(3):910–928, 2002. Cited on page 26.

[77] David H Meyer, Zachary A Castillo, Kevin C Cox, and Paul D Kunz. Assessment of rydberg atoms for wideband electric field sensing. *Journal of Physics B: Atomic, Molecular and Optical Physics*, 53(3):034001, 2020. Cited on pages 26, 56, 57, and 81.

[78] Daniel A. Steck. Cesium d line data. `http://steck.us/alkalidata`, November 2019. Cited on pages 29 and 52.

[79] CHRISTOPHER WADE et al. *Terahertz Wave Detection and Imaging with a Hot Rydberg Vapour*. PhD thesis, Durham University, 2017. Cited on page 32.

[80] LUCY DOWNES et al. *A high-speed THz imaging system based on THz-to-optical conversion in atomic vapour*. PhD thesis, Durham University, 2020. Cited on pages 32, 50, 71, 75, 83, 84, 86, and 179.

[81] MATTHEW JAMIESON et al. *Optimizing a Rydberg atom-based terahertz imaging system*. PhD thesis, Durham University, 2023. Cited on page 32.

[82] Jayampathi CB Kangara, Andrew J Hachtel, Matthew C Gillette, Jason T Barkeloo, Ethan R Clements, Samir Bali, Brett E Unks, Nicholas A Proite, Deniz D Yavuz, Paul J Martin, et al. Design and construction of cost-effective tapered amplifier systems for laser cooling and trapping experiments. *American Journal of Physics*, 82(8):805–817, 2014. Cited on page 33.

[83] CJ Hawthorn, KP Weber, and Robert E Scholten. Littrow configuration tunable external cavity diode laser with fixed direction output beam. *Review of scientific instruments*, 72(12):4477–4479, 2001. Cited on page 34.

[84] GD Boyd and DA Kleinman. Parametric interaction of focused gaussian light beams. *Journal of Applied Physics*, 39(8):3597–3639, 1968. Cited on page 37.

[85] Martin M Fejer, GA Magel, Dieter H Jundt, and Robert L Byer. Quasi-phase-matched second harmonic generation: tuning and tolerances. *IEEE Journal of quantum electronics*, 28(11):2631–2654, 1992. Cited on page 38.

[86] S Manjooran, H Zhao, IT Lima, and A Major. Phase-matching properties of ppktp, mgo: Ppslt and mgo: Ppcln for ultrafast optical parametric oscillation in the visible and near-infrared ranges with green pump. *Laser Physics*, 22(8):1325–1330, 2012. Cited on page 39.

[87] I Dolev, A Ganany-Padowicz, O Gayer, A Arie, J Mangin, and Grégory Gadret. Linear and nonlinear optical properties of mgo: Litao3. *Applied Physics B*, 96(2):423–432, 2009. Cited on page 39.

[88] Remy Legaie, Craig J. Picken, and Jonathan D. Pritchard. Sub-kilohertz excitation lasers for quantum information processing with rydberg atoms. *Journal of the Optical Society of America B*, 35(4):892, April 2018. Cited on page 39.

[89] CP Pearman, CS Adams, SG Cox, PF Griffin, DA Smith, and IG Hughes. Polarization spectroscopy of a closed atomic transition: applications to laser frequency locking. *Journal of Physics B: Atomic, Molecular and Optical Physics*, 35(24):5141, 2002. Cited on page 43.

[90] TW Hansch and B Couillaud. Laser frequency stabilization by polarization spectroscopy of a reflecting reference cavity. *Optics communications*, 35(3):441–444, 1980. Cited on page 44.

[91] Eric D Black. An introduction to pound–drever–hall laser frequency stabilization. *American journal of physics*, 69(1):79–87, 2001. Cited on page 44.

[92] Marcelo Alejandro Luda, Martin Drechsler, Christian Tomás Schmiegelow, and Jorge Codnia. Compact embedded device for lock-in measurements and

experiment active control. *Review of Scientific Instruments*, 90(2):023106, 2019. Cited on page 44.

[93] M Vainio, JE Bernard, and Louis Marmet. Cavity-enhanced optical frequency doubler based on transmission-mode hänsch–couillaud locking. *Applied Physics B*, 104:897–908, 2011. Cited on page 45.

[94] David H Meyer, Paul D Kunz, and Neal Solmeyer. Nonlinear polarization spectroscopy of a rydberg state for laser stabilization. *Applied Optics*, 56(3):B92–B96, 2017. Cited on page 47.

[95] Anusha Krishna, Kanhaiya Pandey, Ajay Wasan, and Vasant Natarajan. High-resolution hyperfine spectroscopy of excited states using electromagnetically induced transparency. *EPL (Europhysics Letters)*, 72(2):221–227, 2005. Cited on page 51.

[96] D Pizzey, JD Briscoe, FD Logue, FS Ponciano-Ojeda, SA Wrathmall, and IG Hughes. Laser spectroscopy of hot atomic vapours: from'scope to theoretical fit. *New Journal of Physics*, 24(12):125001, 2022. Cited on page 52.

[97] Torsten Bronger, Gregor Thalhammer, and Matthieu Dartiailh. `https://github.com/pyvisa/pyvisa`, August 2020. Cited on page 53.

[98] Christian Hahn. windfreak, 2022. Accessed: 2025-10-10. Cited on page 53.

[99] Randall G Hulet and Daniel Kleppner. Rydberg atoms in" circular" states. *Physical review letters*, 51(16):1430, 1983. Cited on pages 56 and 93.

[100] K. A. Safinya, T. F. Gallagher, and W Sandner. Resonance measurements of f-h and f-i intervals in cesium using selective and delayed field ionization. *Physical Review A*, 22(6):2672, 1980. Cited on pages 56, 69, 93, 96, 98, and 99.

[101] S. J. Berl, C. A. Sackett, T. F. Gallagher, and J Nunkaew. Core polarizability of rubidium using spectroscopy of the n g to n h, n i rydberg transitions. *Physical Review A*, 102(6):062818, 2020. Cited on pages 56, 68, and 95.

[102] Yuan-Yu Jau and Tony Carter. Vapor-cell-based atomic electrometry for detection frequencies below 1 khz. *Phys. Rev. Applied*, 13:054034, May 2020. Cited on page 56.

[103] Shuying Chen, Dominic J. Reed, Andrew R. MacKellar, Lucy A. Downes, Nourah F. A. Almuhawish, Matthew J. Jamieson, Charles S. Adams, and Kevin J. Weatherill. Terahertz electrometry via infrared spectroscopy of atomic vapor. *Optica*, 9(5):485–491, May 2022. Cited on pages 56 and 72.

[104] David H Meyer, Paul D Kunz, and Kevin C Cox. Waveguide-coupled rydberg spectrum analyzer from 0 to 20 ghz. *Physical review applied*, 15(1):014053, 2021. Cited on page 57.

[105] Mingyong Jing, Ying Hu, Jie Ma, Hao Zhang, Linjie Zhang, Liantuan Xiao, and Suotang Jia. Atomic superheterodyne receiver based on microwave-dressed rydberg spectroscopy. *Nature Physics*, 16(9):911+, SEP 2020. Cited on page 57.

[106] Merrill Ivan Skolnik et al. *Introduction to radar systems*, volume 3. McGraw-hill New York, 1980. Cited on pages 57 and 69.

[107] James S McLean. A re-examination of the fundamental limits on the radiation q of electrically small antennas. *IEEE Transactions on antennas and propagation*, 44(5):672, 1996. Cited on page 57.

[108] Gary Breed et al. Basic principles of electrically small antennas. *High frequency electronics*, 6(2):50–53, 2007. Cited on page 57.

[109] Kevin C Cox, David H Meyer, Fredrik K Fatemi, and Paul D Kunz. Quantum-limited atomic receiver in the electrically small regime. *Physical Review Letters*, 121(11):110502, 2018. Cited on page 58.

[110] KM Backes, PK Elgee, K-J LeBlanc, CT Fancher, DH Meyer, PD Kunz, N Malvania, KL Nicolich, JC Hill, BL Marlow, et al. Performance of antenna-

based and rydberg quantum rf sensors in the electrically small regime. *Applied Physics Letters*, 125(14), 2024. Cited on pages 58 and 111.

[111] Lan Jen Chu. Physical limitations of omni-directional antennas. *Journal of applied physics*, 19(12):1163–1175, 1948. Cited on page 58.

[112] Ieee standard letter designations for radar-frequency bands. *IEEE Std 521-2019 (Revision of IEEE Std 521-2002)*, pages 1–15, 2020. Cited on page 58.

[113] Christopher Carr, Monsit Tanasittikosol, Armen Sargsyan, David Sarkisyan, Charles S Adams, and Kevin J Weatherill. Three-photon electromagnetically induced transparency using rydberg states. *Optics letters*, 37(18):3858–3860, 2012. Cited on page 59.

[114] Roger C Brown, Baran Kayim, Michael A Viray, Abigail R Perry, Brian C Sawyer, and Robert Wyllie. Very-high-and ultrahigh-frequency electric-field detection using high angular momentum rydberg states. *Physical Review A*, 107(5):052605, 2023. Cited on pages 59, 121, 122, and 127.

[115] Peter K Elgee, Joshua C Hill, Kermit-James E LeBlanc, Gabriel D Ko, Paul D Kunz, David H Meyer, and Kevin C Cox. Satellite radio detection via dual-microwave rydberg spectroscopy. *Applied Physics Letters*, 123(8), 2023. Cited on pages 59, 72, 127, and 128.

[116] Alisher Duspayev, Ryan Cardman, David A. Anderson, and Georg Raithel. High-angular-momentum rydberg states in a room-temperature vapor cell for dc electric-field sensing. *Phys. Rev. Res.*, 6:023138, May 2024. Cited on pages 59, 72, 80, and 128.

[117] D McGloin, DJ Fulton, and MH Dunn. Electromagnetically induced transparency in n-level cascade schemes. *Optics communications*, 190(1-6):221–229, 2001. Cited on page 60.

[118] Andrew P. Rotunno, Christopher L. Holloway, Nikunjkumar Prajapati, Samuel Berweger, Alexandra B. Artusio-Glimpse, Roger Brown, Matthew Simons,

Amy K. Robinson, Baran N. Kayim, Michael A. Viray, Jasmine F. Jones, Brian C. Sawyer, Robert Wyllie, Thad Walker, Richard W. Ziolkowski, Steven R. Jefferts, Steven Geibel, Jonathan Wheeler, and Eric Imhof. Investigating electromagnetically induced transparency spectral lineshape distortion due to non-uniform fields in rydberg-atom electrometry. *Journal of Applied Physics*, 134(8):084401, 08 2023. Cited on pages 63, 88, and 133.

[119] Christopher L. Holloway, Matthew T. Simons, Abdulaziz H. Haddab, Carl J. Williams, and Maxwell W. Holloway. A "real-time" guitar recording using rydberg atoms and electromagnetically induced transparency: Quantum physics meets music. *AIP Advances*, 9(6):065110, 2019. Cited on page 67.

[120] Thomas F Gallagher. Rydberg atoms. In *Springer Handbook of Atomic, Molecular, and Optical Physics*, pages 231–240. Springer, 1994. Cited on pages 67, 93, and 98.

[121] Christopher L Holloway, Matt T Simons, Joshua A Gordon, Andrew Dienstfrey, David A Anderson, and Georg Raithel. Electric field metrology for si traceability: Systematic measurement uncertainties in electromagnetically induced transparency in atomic vapor. *Journal of Applied Physics*, 121(23), 2017. Cited on page 68.

[122] K-H Weber and Craig J Sansonetti. Accurate energies of ns, np, nd, nf, and ng levels of neutral cesium. *Physical Review A*, 35(11):4650, 1987. Cited on pages 68 and 99.

[123] C J Lorenzen and K Niemax. Precise quantum defects of ns, np and nd levels in cs i. *Zeitschrift für Physik A Atoms and Nuclei*, 315:127–133, 1984. Cited on page 68.

[124] S Civiš, M Ferus, P Kubelík, V E Chernov, and E M Zanozina. Fourier transform infrared emission spectra of atomic rubidium: g- and h-states.

Journal of Physics B: Atomic, Molecular and Optical Physics, 45(17):175002, aug 2012. Cited on page 68.

[125] K. Moore, A. Duspayev, R. Cardman, and G. Raithel. Measurement of the rb g-series quantum defect using two-photon microwave spectroscopy. *Phys. Rev. A*, 102:062817, Dec 2020. Cited on page 68.

[126] Simon Haykin. Cognitive radio: brain-empowered wireless communications. *IEEE journal on selected areas in communications*, 23(2):201–220, 2005. Cited on page 69.

[127] M. S. Safronova, D. Budker, D. DeMille, Derek F. Jackson Kimball, A. Derevianko, and Charles W. Clark. Search for new physics with atoms and molecules. *Rev. Mod. Phys.*, 90:025008, Jun 2018. Cited on page 72.

[128] M. G. Kozlov, M. S. Safronova, J. R. Crespo López-Urrutia, and P. O. Schmidt. Highly charged ions: Optical clocks and applications in fundamental physics. *Rev. Mod. Phys.*, 90:045005, Dec 2018. Cited on page 72.

[129] M. Saffman, T. G. Walker, and K. Mølmer. Quantum information with rydberg atoms. *Rev. Mod. Phys.*, 82:2313–2363, Aug 2010. Cited on page 72.

[130] C S Adams, J D Pritchard, and J P Shaffer. Rydberg atom quantum technologies. *Journal of Physics B: Atomic, Molecular and Optical Physics*, 53(1):012002, dec 2019. Cited on page 72.

[131] Jan Nowosielski, Marcin Jastrzębski, Pavel Halavach, Karol Łukanowski, Marcin Jarzyna, Mateusz Mazelanik, Wojciech Wasilewski, and Michał Parniak. Warm rydberg atom-based quadrature amplitude-modulated receiver. *Optics Express*, 32(17):30027–30039, 2024. Cited on pages 72 and 127.

[132] Nikunjkumar Prajapati, Andrew P. Rotunno, Samuel Berweger, Matthew T. Simons, Alexandra B. Artusio-Glimpse, Stephen D. Voran, and Christopher L. Holloway. Tv and video game streaming with a quantum receiver: A study

on a rydberg atom-based receiver's bandwidth and reception clarity. *AVS Quantum Sci.*, 4:035001, 2022. Cited on page 72.

[133] Mingwei Lei and Meng Shi. High sensitivity measurement of ulf, vlf, and lf fields with a rydberg-atom sensor. *Opt. Lett.*, 49(19):5547–5550, Oct 2024. Cited on page 72.

[134] Lucy A. Downes, Andrew R. MacKellar, Daniel J. Whiting, Cyril Bourgenot, Charles S. Adams, and Kevin J. Weatherill. Full-field terahertz imaging at kilohertz frame rates using atomic vapor. *Phys. Rev. X*, 10:011027, Feb 2020. Cited on page 72.

[135] Charles Cheung, Mikhail G Kozlov, Sergey G Porsev, Marianna S Safronova, Ilya I Tupitsyn, and Andrey I Bondarev. pci: A parallel configuration interaction software package for high-precision atomic structure calculations. *Computer Physics Communications*, 308:109463, 2025. Cited on page 72.

[136] K.-H. Weber and Craig J. Sansonetti. Accurate energies of ns, np, nd, nf, and ng levels of neutral cesium. *Phys. Rev. A*, 35:4650–4660, Jun 1987. Cited on pages 72, 73, 84, 85, 87, 97, and 99.

[137] P. Goy, J. M. Raimond, G. Vitrant, and S. Haroche. Millimeter-wave spectroscopy in cesium rydberg states. quantum defects, fine- and hyperfine-structure measurements. *Phys. Rev. A*, 26:2733–2742, Nov 1982. Cited on page 72.

[138] Craig J. Sansonetti and C. J. Lorenzen. Doppler-free resonantly enhanced two-photon spectroscopy of np and nf rydberg states in atomic cesium. *Phys. Rev. A*, 30:1805–1811, Oct 1984. Cited on page 72.

[139] Jingxu Bai, Rong Song, Jiabei Fan, Yuechun Jiao, Jianming Zhao, Suotang Jia, and Georg Raithel. Quantum defects of nF_J levels of cs rydberg atoms. *Phys. Rev. A*, 108:022804, Aug 2023. Cited on pages 72, 84, and 87.

[140] Johannes Deiglmayr, Holger Herburger, Heiner Saßmannshausen, Paul Jansen, Hansjürg Schmutz, and Frédéric Merkt. Precision measurement of the ioniza-

tion energy of cs i. *Phys. Rev. A*, 93:013424, Jan 2016. Cited on pages 72, 85, and 87.

[141] H. Saßmannshausen, F. Merkt, and J. Deiglmayr. High-resolution spectroscopy of rydberg states in an ultracold cesium gas. *Phys. Rev. A*, 87:032519, Mar 2013. Cited on page 72.

[142] C.-J. Lorenzen and K. Niemax. Precise quantum defects of ns, np and nd levels in cs i. *Zeitschrift für Physik A Atoms and Nuclei*, 315(2):127–133, 1984. Cited on pages 73 and 87.

[143] Eite Tiesinga, Peter J Mohr, David B Newell, and Barry N Taylor. Codata recommended values of the fundamental physical constants: 2018. *Journal of physical and chemical reference data*, 50(3), 2021. Cited on page 73.

[144] Randolf Pohl, Aldo Antognini, François Nez, Fernando D Amaro, François Biraben, João MR Cardoso, Daniel S Covita, Andreas Dax, Satish Dhawan, Luis MP Fernandes, et al. The size of the proton. *nature*, 466(7303):213–216, 2010. Cited on page 73.

[145] Jianming Zhao, Xingbo Zhu, Linjie Zhang, Zhigang Feng, Changyong Li, and Suotang Jia. High sensitivity spectroscopy of cesium rydberg atoms using electromagnetically induced transparency. *Optics Express*, 17(18):15821–15826, 2009. Cited on page 74.

[146] Markus Mack, Florian Karlewski, Helge Hattermann, Simone Höckh, Florian Jessen, Daniel Cano, and József Fortágh. Measurement of absolute transition frequencies of rb 87 to ns and nd rydberg states by means of electromagnetically induced transparency. *Physical Review A—Atomic, Molecular, and Optical Physics*, 83(5):052515, 2011. Cited on page 74.

[147] Matt T Simons, Joshua A Gordon, Christopher L Holloway, David A Anderson, Stephanie A Miller, and Georg Raithel. Using frequency detuning to improve the sensitivity of electric field measurements via electromagnetically induced

transparency and autler-townes splitting in rydberg atoms. *Applied Physics Letters*, 108(17), 2016. Cited on page 74.

[148] Myron L Zimmerman, Michael G Littman, Michael M Kash, and Daniel Kleppner. Stark structure of the rydberg states of alkali-metal atoms. *Physical Review A*, 20(6):2251, 1979. Cited on pages 80 and 93.

[149] Nikola Šibalić, Jonathan D Pritchard, Charles S Adams, and Kevin J Weatherill. Arc: An open-source library for calculating properties of alkali rydberg atoms. *Computer Physics Communications*, 220:319–331, 2017. Cited on pages 80 and 102.

[150] WC Martin. Series formulas for the spectrum of atomic sodium (na i). *JOSA*, 70(7):784–788, 1980. Cited on page 81.

[151] Ifan G. Hughes and Thomas P. A. Hase. *Measurements and their Uncertainties*. Oxford University Press, 2010. Cited on pages 85, 99, 103, and 183.

[152] Pinrui Shen, Donald Booth, Chang Liu, Scott Beattie, Claude Marceau, James P Shaffer, Mariusz Pawlak, and HR Sadeghpour. Ultraprecise determination of cs (n s 1/2) and cs (n dj) quantum defects for sensing and computing: Evaluation of core contributions. *Physical Review Letters*, 133(23):233005, 2024. Cited on pages 87, 88, and 93.

[153] Pinrui Shen, Mariusz Pawlak, Donald Booth, Kent Nickerson, Haddad Miladi, HR Sadeghpour, and James Shaffer. Precision measurement of cs (n fj) quantum defects and calculations of scalar and tensor polarizabilities of the n s 1/2, n pj, n dj, and n fj series. *Physical Review A*, 112(2):022814, 2025. Cited on page 87.

[154] Craig J. Sansonetti, Kenneth L. Andrew, and J. Verges. Polarization, penetration, and exchange effects in the hydrogenlike nf and ng terms of cesium. *J. Opt. Soc. Am.*, 71(4):423–433, Apr 1981. Cited on pages 92, 94, 95, 97, 99, and 103.

[155] Stephen R Lundeen. Fine structure in high-l rydberg states: A path to properties of positive ions. *Advances in atomic, molecular, and optical physics*, 52:161–208, 2005. Cited on page 92.

[156] W. E. Cooke, T. F. Gallagher, R. M. Hill, and S. A. Edelstein. Resonance measurements of $d - f$ and $d - g$ intervals in lithium rydberg states. *Phys. Rev. A*, 16:1141–1145, Sep 1977. Cited on page 92.

[157] L. G. Gray, X. Sun, and K. B. MacAdam. Resonance measurements of d-f-g-h intervals in rydberg states of sodium and a redetermination of the core polarizabilities. *Phys. Rev. A*, 38:4985–4993, Nov 1988. Cited on pages 92 and 103.

[158] Michael Peper, Felix Helmrich, Jonas Butscher, Josef Anton Agner, Hansjürg Schmutz, Frédéric Merkt, and Johannes Deiglmayr. Precision measurement of the ionization energy and quantum defects of ^{39}K i. *Phys. Rev. A*, 100:012501, Jul 2019. Cited on pages 92, 95, 99, 100, 101, and 103.

[159] R A Komara, M A Gearba, C W Fehrenbach, and S R Lundeen. Ion properties from high-l rydberg fine structure: dipole polarizability of si2+. *Journal of Physics B: Atomic, Molecular and Optical Physics*, 38(2):S87, jan 2005. Cited on page 92.

[160] E. L. Snow, M. A. Gearba, R. A. Komara, S. R. Lundeen, and W. G. Sturrus. Determination of dipole and quadrupole polarizabilities of ba$^+$ by measurement of the fine structure of high-l $n = 9$ and 10 rydberg states of barium. *Phys. Rev. A*, 71:022510, Feb 2005. Cited on page 92.

[161] P. L. Jacobson, R. D. Labelle, W. G. Sturrus, R. F. Ward, and S. R. Lundeen. Optical spectroscopy of high-l n=10 rydberg states of nitrogen. *Phys. Rev. A*, 54:314–322, Jul 1996. Cited on page 92.

[162] F. J. Deck, E. A. Hessels, and S. R. Lundeen. Population of high-l sulfur rydberg levels by ion–rydberg-atom charge exchange. *Phys. Rev. A*, 48:4400–4404, Dec 1993. Cited on page 92.

[163] Richard J. Drachman. Rydberg states of helium: An optical-potential analysis. *Phys. Rev. A*, 26:1228–1238, Sep 1982. Cited on page 92.

[164] P. L. Jacobson, D. S. Fisher, C. W. Fehrenbach, W. G. Sturrus, and S. R. Lundeen. Determination of the dipole polarizabilities of $h_2^+(0,0)$ and $d_2^+(0,0)$ by microwave spectroscopy of high-l rydberg states of h_2 and d_2. *Phys. Rev. A*, 56:R4361–R4364, Dec 1997. Cited on page 92.

[165] J Mitroy, M S Safronova, and Charles W Clark. Theory and applications of atomic and ionic polarizabilities. *Journal of Physics B: Atomic, Molecular and Optical Physics*, 43(20):202001, oct 2010. Cited on pages 92, 95, 96, and 100.

[166] Michael Schlagmüller, Tara Cubel Liebisch, Felix Engel, Kathrin S. Kleinbach, Fabian Böttcher, Udo Hermann, Karl M. Westphal, Anita Gaj, Robert Löw, Sebastian Hofferberth, Tilman Pfau, Jesús Pérez-Ríos, and Chris H. Greene. Ultracold chemical reactions of a single rydberg atom in a dense gas. *Phys. Rev. X*, 6:031020, Aug 2016. Cited on page 92.

[167] Pitt Allmendinger, Johannes Deiglmayr, Katharina Höveler, Otto Schullian, and Frédéric Merkt. Observation of enhanced rate coefficients in the H 2 + + H 2 → H 3 + + H reaction at low collision energies. *The Journal of Chemical Physics*, 145(24):244316, 12 2016. Cited on page 92.

[168] M. Marinescu, H. R. Sadeghpour, and A. Dalgarno. Dispersion coefficients for alkali-metal dimers. *Phys. Rev. A*, 49:982–988, Feb 1994. Cited on page 92.

[169] P. G. Westergaard, J. Lodewyck, L. Lorini, A. Lecallier, E. A. Burt, M. Zawada, J. Millo, and P. Lemonde. Lattice-induced frequency shifts in sr optical lattice clocks at the 10^{-17} level. *Phys. Rev. Lett.*, 106:210801, May 2011. Cited on page 92.

[170] Marianna S. Safronova, Mikhail G. Kozlov, and Charles W. Clark. Blackbody radiation shifts in optical atomic clocks. *IEEE Transactions on Ultrasonics, Ferroelectrics, and Frequency Control*, 59(3):439–447, 2012. Cited on page 92.

[171] Sam R. Cohen and Jeff D. Thompson. Quantum computing with circular rydberg atoms. *PRX Quantum*, 2:030322, Aug 2021. Cited on page 92.

[172] J. Hare, A. Nussenzweig, C. Gabbanini, M. Weidemuller, P. Goy, M. Gross, and S. Haroche. Toward a rydberg constant measurement on circular atoms. *IEEE Transactions on Instrumentation and Measurement*, 42(2):331–334, 1993. Cited on page 92.

[173] Ulrich D Jentschura, Peter J Mohr, and Joseph N Tan. Fundamental constants and tests of theory in rydberg states of one-electron ions. *Journal of Physics B: Atomic, Molecular and Optical Physics*, 43(7):074002, 2010. Cited on page 92.

[174] Andira Ramos, Kaitlin Moore, and Georg Raithel. Measuring the rydberg constant using circular rydberg atoms in an intensity-modulated optical lattice. *Phys. Rev. A*, 96:032513, Sep 2017. Cited on page 92.

[175] M. S. Safronova, W. R. Johnson, and A. Derevianko. Relativistic many-body calculations of energy levels, hyperfine constants, electric-dipole matrix elements, and static polarizabilities for alkali-metal atoms. *Phys. Rev. A*, 60:4476–4487, Dec 1999. Cited on page 92.

[176] William F. Holmgren, Raisa Trubko, Ivan Hromada, and Alexander D. Cronin. Measurement of a wavelength of light for which the energy shift for an atom vanishes. *Phys. Rev. Lett.*, 109:243004, Dec 2012. Cited on page 92.

[177] Apichayaporn Ratkata, Philip D. Gregory, Andrew D. Innes, Alex J. Matthies, Lewis A. McArd, Jonathan M. Mortlock, M. S. Safronova, Sarah L. Bromley, and Simon L. Cornish. Measurement of the tune-out wavelength for ^{133}Cs at 880 nm. *Phys. Rev. A*, 104:052813, Nov 2021. Cited on page 93.

[178] VA Yerokhin, SY Buhmann, S Fritzsche, and A Surzhykov. Electric dipole polarizabilities of rydberg states of alkali-metal atoms. *Physical Review A*, 94(3):032503, 2016. Cited on page 93.

[179] MS Safronova, WR Johnson, and A Derevianko. Relativistic many-body calculations of energy levels, hyperfine constants, electric-dipole matrix elements, and static polarizabilities for alkali-metal atoms. *Physical Review A*, 60(6):4476, 1999. Cited on page 93.

[180] Jason M Amini and Harvey Gould. High precision measurement of the static dipole polarizability of cesium. *Physical review letters*, 91(15):153001, 2003. Cited on page 93.

[181] S. J. Berl, C. A. Sackett, T. F. Gallagher, and J. Nunkaew. Core polarizability of rubidium using spectroscopy of the ng to nh, ni rydberg transitions. *Phys. Rev. A*, 102:062818, Dec 2020. Cited on pages 93, 98, and 99.

[182] P Camus and S Cohen. Effective core polarizabilities in ba high-l nsnl double rydberg atoms. *Physical Review A*, 51(3):1985, 1995. Cited on page 93.

[183] R. A. Komara, M. A. Gearba, S. R. Lundeen, and C. W. Fehrenbach. Determination of the polarizability of na-like silicon by study of the fine structure of high-l rydberg states of si^{2+}. *Phys. Rev. A*, 67:062502, Jun 2003. Cited on page 93.

[184] James Mitroy and MS Safronova. Polarizabilities of the mg+ and si 3+ ions. *Physical Review A—Atomic, Molecular, and Optical Physics*, 79(1):012513, 2009. Cited on pages 93 and 101.

[185] S H Patil. Accurate values of polarizabilities from high-angular-momentum rydberg states. *Journal of Physics B: Atomic, Molecular and Optical Physics*, 27(3):601, feb 1994. Cited on page 95.

[186] Richard J Drachman. Rydberg states of helium: An optical-potential analysis. *Physical Review A*, 26(3):1228, 1982. Cited on pages 95 and 101.

[187] Thomas F. Gallagher. *Rydberg Atoms*. Cambridge Monographs on Atomic, Molecular and Chemical Physics. Cambridge University Press, 1994. Cited on pages 95, 98, 99, and 103.

[188] Kjell Bockasten. Mean values of powers of the radius for hydrogenic electron orbits. *Phys. Rev. A*, 9:1087–1089, Mar 1974. Cited on page 96.

[189] Joseph E. Mayer and Maria Goeppert Mayer. The polarizabilities of ions from spectra. *Phys. Rev.*, 43:605–611, Apr 1933. Cited on page 96.

[190] EL Snow and SR Lundeen. Fine-structure measurements in high-l n= 17 and 20 rydberg states of barium. *Physical Review A—Atomic, Molecular, and Optical Physics*, 76(5):052505, 2007. Cited on page 96.

[191] L. J. Curtis and P. S. Ramanujam. Semiclassical parameterization of the l $\geq$ 3 energy levels in cs i. *J. Opt. Soc. Am.*, 71(11):1315–1317, Nov 1981. Cited on page 99.

[192] H. L. Zhou and D. W. Norcross. Improved calculation of the quadratic stark effect in the $6P_{3/2}$ state of cs. *Phys. Rev. A*, 40:5048–5051, Nov 1989. Cited on pages 99 and 103.

[193] K B S Eriksson and I Wenåker. New wavelength measurements in cs i. *Physica Scripta*, 1(1):21, jan 1970. Cited on page 99.

[194] K. Fredriksson, H. Lundberg, and S. Svanberg. Fine- and hyperfine-structure investigation in the $5^2d - n^2f$ series of cesium. *Phys. Rev. A*, 21:241–247, Jan 1980. Cited on page 99.

[195] Chemia J. Kleinman, Yukap Hahn, and Larry Spruch. Dominant nonadiabatic contribution to the long-range electron-atom interaction. *Phys. Rev.*, 165:53–62, Jan 1968. Cited on pages 99 and 100.

[196] H Eissa and U Öpik. The polarization of a closed-shell core of an atomic system by an outer electron i. a correction to the adiabatic approximation.

Proceedings of the Physical Society, 92(3):556, nov 1967. Cited on pages 100 and 101.

[197] S. H. Patil. Atomic potentials, polarizabilities, and nonadiabatic corrections in high-angular-momentum rydberg states. *Phys. Rev. A*, 33:90–95, Jan 1986. Cited on page 100.

[198] S Krishnagopal, Shobhana Narasimhan, and SH Patil. Multipolar polarizabilities and rydberg states. *Journal of Chemical Physics*, 83(11):5772–5777, 1985. Cited on page 100.

[199] G. W. F. Drake and R. A. Swainson. Quantum defects and the 1/n dependence of rydberg energies: Second-order polarization effects. *Phys. Rev. A*, 44:5448–5459, Nov 1991. Cited on pages 100 and 101.

[200] A Dalgarno and AE Kingston. The refractive indices and verdet constants of the inert gases. *Proceedings of the Royal Society of London. Series A. Mathematical and Physical Sciences*, 259(1298):424–431, 1960. Cited on page 100.

[201] Craig J Sansonetti and Kenneth L Andrew. Spectrum and energy levels of singly ionized cesium: I. revision and extension of the cs ii energy levels. *Journal of the Optical Society of America B*, 3(3):386–397, 1986. Cited on page 100.

[202] W.R. Johnson, Dietmar Kolb, and K.-N. Huang. Electric-dipole, quadrupole, and magnetic-dipole susceptibilities and shielding factors for closed-shell ions of the he, ne, ar, ni (cu+), kr, pb, and xe isoelectronic sequences. *Atomic Data and Nuclear Data Tables*, 28(2):333–340, 1983. Cited on pages 101 and 103.

[203] Ivan S Lim, Jon K Laerdahl, and Peter Schwerdtfeger. Fully relativistic coupled-cluster static dipole polarizabilities of the positively charged alkali ions from li+ to 119+. *The Journal of chemical physics*, 116(1):172–178, 2002. Cited on pages 101 and 103.

[204] M. S. Safronova, U. I. Safronova, and Charles W. Clark. Magic wavelengths, matrix elements, polarizabilities, and lifetimes of cs. *Phys. Rev. A*, 94:012505, Jul 2016. Cited on pages 101 and 103.

[205] RM Sternheimer. Quadrupole polarizabilities of various ions and the alkali atoms. *Physical Review A*, 1(2):321, 1970. Cited on page 103.

[206] GD Mahan. Modified sternheimer equation for polarizability. *Physical Review A*, 22(5):1780, 1980. Cited on page 103.

[207] Sebastian Weber, Christoph Tresp, Henri Menke, Alban Urvoy, Ofer Firstenberg, Hans Peter Büchler, and Sebastian Hofferberth. Calculation of rydberg interaction potentials. *Journal of Physics B: Atomic, Molecular and Optical Physics*, 50(13):133001, jun 2017. Cited on page 103.

[208] Chris H. Greene, A. S. Dickinson, and H. R. Sadeghpour. Creation of polar and nonpolar ultra-long-range rydberg molecules. *Phys. Rev. Lett.*, 85:2458–2461, Sep 2000. Cited on page 103.

[209] Matthew T Eiles. Trilobites, butterflies, and other exotic specimens of long-range rydberg molecules. *Journal of Physics B: Atomic, Molecular and Optical Physics*, 52(11):113001, may 2019. Cited on page 103.

[210] Matthias Schmidt, Stephanie Bohaichuk, Vijin Venu, Florian Christaller, Chang Liu, Fabian Ripka, Harald Kübler, and James P Shaffer. Rydberg-atom-based radio-frequency sensors: amplitude-regime sensing. *Optics Express*, 32(16):27768–27791, 2024. Cited on pages 107, 120, and 121.

[211] Peter B Weichman. Resonant optical bistability in support of enhanced rydberg-atom sensors. *Physical Review A*, 112(4):042805, 2025. Cited on pages 107 and 130.

[212] Yu Tang, Hanbin Zhou, Chuang Yang, Shuang Ren, Siyuan Wang, and Chenxi Lu. Noise performance of a rydberg atomic receiver. *Physical Review A*, 112(4):043106, 2025. Cited on pages 107, 125, and 127.

[213] David M Pozar. *Microwave engineering: theory and techniques*. John wiley & sons, 2021. Cited on pages 110 and 111.

[214] Gabriel Santamaria-Botello et al. Comparison of noise temperature of rydberg-atom and electronic microwave receivers. arXiv:2209.00908, 2022. Cited on pages 110, 111, 112, 113, 115, 116, 117, 118, 133, 134, and 135.

[215] Georgia Sandidge and et al. Resonant structures for sensitivity enhancement of rydberg-atom microwave receivers. *IEEE Transactions on Microwave Theory and Techniques*, 72(4):2057–2066, 2024. Cited on pages 110, 116, 133, 134, 135, and 136.

[216] Hai-Tao Tu, Kai-Yu Liao, Hong-Lei Wang, Yi-Fei Zhu, Si-Yuan Qiu, Hao Jiang, Wei Huang, Wu Bian, Hui Yan, and Shi-Liang Zhu. Approaching the standard quantum limit of a rydberg-atom microwave electrometer. *Science Advances*, 10(51):eads0683, 2024. Cited on pages 112, 113, 121, 136, and 139.

[217] TF Gallagher and WE Cooke. Interactions of blackbody radiation with atoms. *Physical Review Letters*, 42(13):835, 1979. Cited on page 113.

[218] WE Cooke and TF Gallagher. Effects of blackbody radiation on highly excited atoms. *Physical Review A*, 21(2):588, 1980. Cited on page 113.

[219] L Hollberg and JL Hall. Measurement of the shift of rydberg energy levels induced by blackbody radiation. *Physical review letters*, 53(3):230, 1984. Cited on page 113.

[220] Matthew T Simons, Marcus D Kautz, Christopher L Holloway, David A Anderson, Georg Raithel, Daniel Stack, Marc C St John, and Wansheng Su. Electromagnetically induced transparency (eit) and autler-townes (at) splitting in the presence of band-limited white gaussian noise. *Journal of Applied Physics*, 123(20), 2018. Cited on page 113.

[221] Yin Zhang, Jiayi Zhang, Bokai Xu, Yuanbin Chen, Zhilong Liu, Jiakang Zheng, Enyu Shi, Ziheng Liu, Tierui Gong, Wei EI Sha, et al. Rydberg atomic

receivers for wireless communications: Fundamentals, potential, applications, and challenges. *arXiv preprint arXiv:2507.22909*, 2025. Cited on page 113.

[222] Jieao Zhu and Linglong Dai. General signal model and capacity limit for rydberg quantum information system. *arXiv preprint arXiv:2506.23455*, 2025. Cited on page 113.

[223] Leonardo A Pachón and Paul Brumer. Incoherent excitation of thermally equilibrated open quantum systems. *Physical Review A—Atomic, Molecular, and Optical Physics*, 87(2):022106, 2013. Cited on page 114.

[224] Channprit Kaur, Pinrui Shen, Donald Booth, Andrew Todd, and James P Shaffer. The impact of thermal fields on rydberg atom radio frequency sensors. *arXiv preprint arXiv:2508.17506*, 2025. Cited on pages 114 and 115.

[225] P Zoller, G Alber, and R Salvador. ac stark splitting in intense stochastic driving fields with gaussian statistics and non-lorentzian line shape. *Physical Review A*, 24(1):398, 1981. Cited on page 114.

[226] Th Haslwanter, H Ritsch, J Cooper, and P Zoller. Laser-noise-induced population fluctuations in two-and three-level systems. *Physical Review A*, 38(11):5652, 1988. Cited on page 114.

[227] R Walser and P Zoller. Laser-noise-induced polarization fluctuations as a spectroscopic tool. *Physical Review A*, 49(6):5067, 1994. Cited on page 114.

[228] Thomas L Wilson, Susanne Hüttemeister, Kristen Rohlfs, Kristen Rohlfs, et al. *Tools of radio astronomy*. Springer, 2013. Cited on pages 114 and 127.

[229] Anthony R Kerr and James Randa. Thermal noise and noise measurements—a 2010 update. *IEEE Microwave Magazine*, 11(6):40–52, 2010. Cited on page 115.

[230] Eric B Norrgard, Stephen P Eckel, Christopher L Holloway, and Eric L Shirley. Quantum blackbody thermometry. *New Journal of Physics*, 23(3):033037, 2021. Cited on page 115.

[231] David S La Mantia, Mingxin Lei, Nikunjkumar Prajapati, Noah Schlossberger, Matthew T Simons, Christopher L Holloway, Julia Scherschligt, Stephen P Eckel, and Eric B Norrgard. Compact blackbody-radiation atomic sensor: Measuring temperature using optically excited atoms in vapor cells. *Physical Review Applied*, 23(4):044037, 2025. Cited on page 115.

[232] Gar-Wing Truong, Eric F May, Thomas M Stace, and André N Luiten. Quantitative atomic spectroscopy for primary thermometry. *Physical Review A—Atomic, Molecular, and Optical Physics*, 83(3):033805, 2011. Cited on page 115.

[233] Nicola Agnew, Graham Machin, Erling Riis, and Aidan S Arnold. Practical doppler broadening thermometry. In *AIP Conference Proceedings*, volume 3230, page 110002. AIP Publishing LLC, 2024. Cited on page 115.

[234] Gabriel Santamaría Botello, Florian Sedlmeir, Alfredo Rueda, Kerlos Atia Abdalmalak, Elliott R Brown, Gerd Leuchs, Sascha Preu, Daniel Segovia-Vargas, Dmitry V Strekalov, Luis Enrique García Muñoz, et al. Sensitivity limits of millimeter-wave photonic radiometers based on efficient electro-optic upconverters. *Optica*, 5(10):1210–1219, 2018. Cited on pages 116, 118, 134, and 135.

[235] Mingrui Xu, Xu Han, Chang-Ling Zou, Wei Fu, Yuntao Xu, Changchun Zhong, Liang Jiang, and Hong X Tang. Radiative cooling of a superconducting resonator. *Physical Review Letters*, 124(3):033602, 2020. Cited on pages 116 and 134.

[236] Wiktor Krokosz, Jan Nowosielski, Bartosz Kasza, Sebastian Borówka, Mateusz Mazelanik, Wojciech Wasilewski, and Michał Parniak. Electric-field metrology

of a terahertz frequency comb using rydberg atoms. *Optica*, 12(11):1854–1864, 2025. Cited on page 116.

[237] Nikunjkumar Prajapati, Narayan Bhusal, Andrew P Rotunno, Samuel Berweger, Matthew T Simons, Alexandra B Artusio-Glimpse, Ying Ju Wang, Eric Bottomley, Haoquan Fan, and Christopher L Holloway. Sensitivity comparison of two-photon vs three-photon rydberg electrometry. *Journal of Applied Physics*, 134(2), 2023. Cited on pages 117 and 128.

[238] HR Carleton and WT Maloney. A balanced optical heterodyne detector. *Applied optics*, 7(6):1241–1243, 1968. Cited on page 118.

[239] Shuhe Wu, Dong Zhang, Zhengchun Li, Minwei Shi, Peiyu Yang, Jinxian Guo, Wei Du, Guzhi Bao, and Weiping Zhang. Quantum-enhanced electrometer based on microwave-dressed rydberg atoms. *Physical Review Applied*, 20(6):064028, 2023. Cited on page 118.

[240] Nikunjkumar Prajapati, Ziqi Niu, and Irina Novikova. Quantum-enhanced two-photon spectroscopy using two-mode squeezed light. *Optics Letters*, 46(8):1800–1803, 2021. Cited on page 118.

[241] Wayne M Itano, James C Bergquist, John J Bollinger, JM Gilligan, DJ Heinzen, FL Moore, MG Raizen, and David J Wineland. Quantum projection noise: Population fluctuations in two-level systems. *Physical Review A*, 47(5):3554, 1993. Cited on page 120.

[242] John Kitching, Svenja Knappe, and Elizabeth A Donley. Atomic sensors–a review. *IEEE Sensors Journal*, 11(9):1749–1758, 2011. Cited on page 120.

[243] Haoquan Fan, Santosh Kumar, Jonathon Sedlacek, Harald Kübler, Shaya Karimkashi, and James P Shaffer. Atom based rf electric field sensing. *Journal of Physics B: Atomic, Molecular and Optical Physics*, 48(20):202001, 2015. Cited on pages 121 and 122.

[244] Anne Fabricant, Irina Novikova, and Georg Bison. How to build a magnetometer with thermal atomic vapor: a tutorial. *New Journal of Physics*, 25(2):025001, 2023. Cited on page 122.

[245] James C Camparo and John G Coffer. Conversion of laser phase noise to amplitude noise in a resonant atomic vapor: The role of laser linewidth. *Physical Review A*, 59(1):728, 1999. Cited on page 123.

[246] John Kitching, Svenja Knappe, M Vukicevic, Leo Hollberg, Robert Wynands, and W Weidmann. A microwave frequency reference based on vcsel-driven dark line resonances in cs vapor. *IEEE Transactions on Instrumentation and Measurement*, 49(6):1313–1317, 2000. Cited on page 123.

[247] Ricardo Jiménez-Martínez, W Clark Griffith, Ying-Ju Wang, Svenja Knappe, John Kitching, Ken Smith, and Mark D Prouty. Sensitivity comparison of mx and frequency-modulated bell–bloom cs magnetometers in a microfabricated cell. *IEEE Transactions on Instrumentation and Measurement*, 59(2):372–378, 2009. Cited on page 123.

[248] Vishal Shah and John Kitching. Advances in coherent population trapping for atomic clocks. In *Advances in atomic, molecular, and optical physics*, volume 59, pages 21–74. Elsevier, 2010. Cited on page 123.

[249] Zheng Wang, Junliang Gao, Xinqi Song, Suotang Jia, and Shaohao Yang. Noise analysis of the atomic superheterodyne receiver based on flat-top laser beams. *Optics Express*, 31(12):19909–19917, 2023. Cited on pages 123 and 137.

[250] Bowen Yang, Yuhan Yan, Xuejie Li, Haojie Zhao, Ling Xiao, Xiaolin Li, Jianliao Deng, and Huadong Cheng. Sensitivity of rydberg microwave electrometry limited by laser frequency noise. *Physical Review A*, 109(3):032609, 2024. Cited on pages 124, 125, 185, and 187.

[251] Rüdiger Paschotta. Noise in laser technology: Part 1: Intensity and phase noise. *Optik & photonik*, 4(2):48–50, 2009. Cited on page 125.

[252] Nikunjkumar Prajapati, Jakob W Kunzler, Alexandra B Artusio-Glimpse, Andrew P Rotunno, Samuel Berweger, Matthew T Simons, Christopher L Holloway, Chad M Gardner, Michael S Mcbeth, and Robert A Younts. High angular momentum coupling for enhanced rydberg-atom sensing in the very-high frequency band. *Journal of Applied Physics*, 135(7), 2024. Cited on page 127.

[253] Matt J Jamieson, C Stuart Adams, Kevin J Weatherill, Ryan K Hanley, Natalia Alves, and James Keaveney. Continuous-time ultrahigh-frequency sensing using cold rydberg atoms. *Physical Review Applied*, 24(3):034022, 2025. Cited on pages 127 and 128.

[254] Stephanie M Bohaichuk, Fabian Ripka, Vijin Venu, Florian Christaller, Chang Liu, Matthias Schmidt, Harald Kübler, and James P Shaffer. Three-photon rydberg-atom-based radio-frequency sensing scheme with narrow linewidth. *Physical Review Applied*, 20(6):L061004, 2023. Cited on page 128.

[255] Nikunjkumar Prajapati, Amy K. Robinson, Samuel Berweger, et al. Enhancement of electromagnetically induced transparency based rydberg-atom electrometry through population repumping. *Applied Physics Letters*, 119(21):214001, 2021. Cited on pages 130 and 136.

[256] David A Anderson, Eric G Paradis, and Georg Raithel. A vapor-cell atomic sensor for radio-frequency field detection using a polarization-selective field enhancement resonator. *Applied Physics Letters*, 113(7), 2018. Cited on page 133.

[257] Christopher L Holloway, Nikunjkumar Prajapati, Alexandra B Artusio-Glimpse, Samuel Berweger, Matthew T Simons, Yoshiaki Kasahara, Andrea Alu, and Richard W Ziolkowski. Rydberg atom-based field sensing enhancement using a split-ring resonator. *Applied Physics Letters*, 120(20), 2022. Cited on page 133.

[258] Kai Yang, Yi Lin, Zhenke Ding, Qiang An, Zhanshan Sun, and Yunqi Fu. Local oscillator port-integrated resonators for sensitivity enhancement of vhf band rydberg atomic heterodyne receivers. *IEEE Transactions on Microwave Theory and Techniques*, 2025. Cited on page 133.

[259] AB Matsko, DV Strekalov, and N Yu. Sensitivity of terahertz photonic receivers. *Physical Review A—Atomic, Molecular, and Optical Physics*, 77(4):043812, 2008. Cited on page 134.

[260] Georgia Sandidge and Zoya Popovic. Impact of rb condensation on resonant structures for microwave rydberg-atom electrometers. In *2025 IEEE Radio and Wireless Symposium (RWS)*, pages 45–47. IEEE, 2025. Cited on page 135.

[261] Carlton M Caves. Quantum limits on noise in linear amplifiers. *Physical Review D*, 26(8):1817, 1982. Cited on page 135.

[262] Mini-Circuits. Amplifiers – webstore. https://www.minicircuits.com/WebStore/Amplifiers.html, 2025. Accessed: 2025-11-14. Cited on page 136.

[263] Hua Wang, Argyro Kamperi, Boce Lin, and Basem Abdelaziz Abdelmagid Ali. Low noise amplifier noise figure survey 2018–present. https://ideas.ethz.ch/Surveys/lna-survey.html, 2018. [Online; accessed October 2025]. Cited on page 136.

[264] Minghao Cai, Shuhang You, Shanshan Zhang, Zishan Xu, and Hongping Liu. Sensitivity extension of atom-based amplitude-modulation microwave electrometry via high rydberg states. *Applied Physics Letters*, 122(16), 2023. Cited on page 136.

[265] Minghao Cai, Zishan Xu, Shuhang You, and Hongping Liu. Sensitivity improvement and determination of rydberg atom-based microwave sensor. *Photonics*, 9(4):250, April 2022. Cited on page 136.

[266] Rémy Legaie, Georg Raithel, and David A. Anderson. A millimeter-wave atomic receiver. *AVS Quantum Science*, 6(2):025701, 2024. Cited on pages 136 and 139.

[267] Jongmin Lee, Michael J Martin, Yuan-Yu Jau, Tyler Keating, Ivan H Deutsch, and Grant W Biedermann. Demonstration of the jaynes-cummings ladder with rydberg-dressed atoms. *Physical Review A*, 95(4):041801, 2017. Cited on page 140.

[268] SK Kanungo, JD Whalen, Y Lu, M Yuan, S Dasgupta, FB Dunning, KRA Hazzard, and TC Killian. Realizing topological edge states with rydberg-atom synthetic dimensions. *Nature communications*, 13(1):972, 2022. Cited on page 140.

[269] SK Dutta, D Feldbaum, A Walz-Flannigan, JR Guest, and G Raithel. High-angular-momentum states in cold rydberg gases. *Physical Review Letters*, 86(18):3993, 2001. Cited on page 142.

[270] Chris Chatfield and Haipeng Xing. *The analysis of time series: an introduction with R*. Chapman and hall/CRC, 2019. Cited on page 186.

[271] Gene H Golub and Charles F Van Loan. *Matrix computations*. JHU press, 2013. Cited on page 186.

Appendix A

Tables of Transition Frequencies

The 0.5 MHz uncertainty in Table A.1 reflects the fit uncertainty from the intersection of two lines from the three-photon experiment. Table A.1 and Table A.2 includes results from the two-photon scheme, which use different scan ranges and differing number of data points, leading to differing uncertainties.

$np \to n's$ Measurements		$np \to n'd$ Measurements		$nd \to n'f$ Measurements	
Transition	Frequency ν (GHz)	Transition	Frequency ν (GHz)	Transition	Frequency ν (GHz)
$20p_{1/2} \to 20s_{1/2}$	-710.9264	$14p_{1/2} \to 13d_{3/2}$	685.8714	$18d_{3/2} \to 15f_{5/2}$	-1034.94423(7)
$20p_{1/2} \to 21s_{1/2}$	770.1388	$15p_{3/2} \to 14d_{5/2}$	548.6153	$18d_{3/2} \to 16f_{5/2}$	746.66404(9)
$20p_{3/2} \to 21s_{1/2}$	721.8937	$15p_{1/2} \to 14d_{3/2}$	519.0775	$18d_{5/2} \to 15f_{5/2}$	-1050.97405(8)
				$18d_{5/2} \to 15f_{7/2}$	-1051.24888(9)
$21p_{1/2} \to 21s_{1/2}$	-593.8743	$22p_{3/2} \to 20d_{5/2}$	-1025.9229(2)	$18d_{5/2} \to 16f_{5/2}$	730.63472(8)
$21p_{1/2} \to 22s_{1/2}$	646.5781			$18d_{5/2} \to 16f_{7/2}$	730.40683(6)
$21p_{3/2} \to 22s_{1/2}$	606.1677	$24p_{1/2} \to 22d_{3/2}$	-730.6733		
$21p_{3/2} \to 21s_{1/2}$	-634.2831	$24p_{3/2} \to 22d_{5/2}$	-747.7028	$19d_{3/2} \to 17f_{5/2}$	620.57851(8)
				$19d_{5/2} \to 17f_{5/2}$	607.2809(1)
$22p_{1/2} \to 22s_{1/2}$	-501.1722	$25p_{1/2} \to 23d_{3/2}$	-631.0236	$19d_{5/2} \to 17f_{7/2}$	607.09149(5)
$22p_{1/2} \to 23s_{1/2}$	548.1043	$25p_{1/2} \to 25d_{3/2}$	694.2632		
$22p_{3/2} \to 23s_{1/2}$	513.9218	$25p_{3/2} \to 23d_{5/2}$	-645.8232	$20d_{3/2} \to 17f_{5/2}$	-715.18566(9)
$22p_{3/2} \to 22s_{1/2}$	-535.3544	$25p_{3/2} \to 25d_{5/2}$	677.7750	$20d_{3/2} \to 18f_{5/2}$	521.36182(9)
				$20d_{5/2} \to 17f_{5/2}$	-726.3370(1)
$23p_{3/2} \to 23s_{1/2}$	-455.9748	$26p_{1/2} \to 24d_{3/2}$	-548.7019	$20d_{5/2} \to 17f_{7/2}$	-726.52729(8)
		$26p_{1/2} \to 26d_{3/2}$	607.3581	$20d_{5/2} \to 18f_{5/2}$	510.2102(1)
$27p_{1/2} \to 29s_{1/2}$	719.4515	$26p_{3/2} \to 24d_{5/2}$	-561.6441	$20d_{5/2} \to 18f_{7/2}$	510.0500(1)
$27p_{3/2} \to 29s_{1/2}$	702.8132	$26p_{3/2} \to 26d_{5/2}$	593.0072		
				$21d_{3/2} \to 18f_{5/2}$	-603.9741(1)
$28p_{1/2} \to 30s_{1/2}$	636.9761	$27p_{1/2} \to 25d_{3/2}$	-480.0988	$21d_{5/2} \to 18f_{7/2}$	-613.5782(1)
$28p_{1/2} \to 27s_{1/2}$	-723.7312	$27p_{1/2} \to 27d_{3/2}$	534.3773		
$28p_{3/2} \to 30s_{1/2}$	622.2992	$27p_{3/2} \to 25d_{5/2}$	-491.4822	$22d_{3/2} \to 19f_{5/2}$	-514.6726(1)
$28p_{3/2} \to 27s_{1/2}$	-738.4080	$27p_{3/2} \to 27d_{5/2}$	521.8114	$22d_{5/2} \to 19f_{7/2}$	-522.87675(9)
$29p_{1/2} \to 31s_{1/2}$	566.6445	$30p_{1/2} \to 31d_{3/2}$	674.1317		
$29p_{1/2} \to 28s_{1/2}$	-639.1752	$30p_{3/2} \to 31d_{5/2}$	665.1313		
$29p_{3/2} \to 31s_{1/2}$	553.6318				
$29p_{3/2} \to 28s_{1/2}$	-652.1882	$31p_{3/2} \to 32d_{5/2}$	597.3845		
$30p_{1/2} \to 29s_{1/2}$	-567.2976	$32p_{1/2} \to 33d_{3/2}$	545.7370		
$30p_{3/2} \to 32s_{1/2}$	494.7101	$32p_{3/2} \to 33d_{5/2}$	538.5382		
$30p_{3/2} \to 29s_{1/2}$	-578.8893				
$30p_{3/2} \to 30s_{1/2}$	-516.1775	$33p_{1/2} \to 34d_{3/2}$	493.6529		
$34p_{1/2} \to 32s_{1/2}$	-653.2059	$33p_{1/2} \to 35d_{3/2}$	694.0853		
		$33p_{3/2} \to 34d_{5/2}$	487.1777		
$35p_{1/2} \to 33s_{1/2}$	-590.2641	$33p_{3/2} \to 35d_{5/2}$	687.4378		
$35p_{3/2} \to 33s_{1/2}$	-597.1567				
		$34p_{1/2} \to 36d_{3/2}$	630.7592		
$36p_{3/2} \to 34s_{1/2}$	-541.4330	$34p_{3/2} \to 36d_{5/2}$	624.7619		
		$35p_{1/2} \to 37d_{3/2}$	574.9137		
		$35p_{3/2} \to 37d_{5/2}$	569.4835		
		$36p_{3/2} \to 38d_{5/2}$	520.5438		

Table A.1: Tabulated values of the $p \to s$, $p \to d$ and $d \to f$ transition frequencies measured using the two- and three-photon method. The $p \to s$ and $p \to d$ measurements have errors of 0.5 MHz unless otherwise specified. The $d \to f$ measurements have separate errors given for each measurement. A negative sign indicates that the final state lies lower in energy than the initial state. The $np \to n's$ and $np \to n'd$ measurements (bar one) are from [80].

$nf \rightarrow n'g$ ($\ell = 4$)		$ng \rightarrow n'h$		$nh \rightarrow n'i$		$ni \rightarrow n'k$		$nk \rightarrow$ n$'l$	
Transition	ν / GHz	Transition	ν / MHz	Transition	ν / MHz	Transition	ν / MHz	Transition	ν / MHz
$15f_{5/2} \rightarrow 15g_{7/2}$	50.3241(2)	$15g_{9/2} \rightarrow 15h$	8700.8(4)	$15h \rightarrow 15i$	2675.1(5)	$15i \rightarrow 15k$	1016(1)	$15k \rightarrow 15l$	439(1)
$15f_{7/2} \rightarrow 15g_{9/2}$	50.6009(1)								
$16f_{5/2} \rightarrow 16g_{7/2}$	41.5844(2)	$16g_{9/2} \rightarrow 16h$	7190.5(5)	$16h \rightarrow 16i$	2206.9(5)	$16i \rightarrow 16k$	840(1)	$16k \rightarrow 16l$	365(1)
$16f_{7/2} \rightarrow 16g_{9/2}$	41.8139(1)								
$17f_{5/2} \rightarrow 17g_{7/2}$	34.7509(1)	$17g_{9/2} \rightarrow 17h$	6007.2(5)	$17h \rightarrow 17i$	1851.3(4)	$17i \rightarrow 17k$	705(1)	$17k \rightarrow 17l$	306(1)
$17f_{7/2} \rightarrow 17g_{9/2}$	34.9430(1)								
$18f_{5/2} \rightarrow 18g_{7/2}$	29.3321(1)	$18g_{9/2} \rightarrow 18h$	5071.8(5)	$18h \rightarrow 18i$	1563.4(5)	$18i \rightarrow 18k$	594(1)		
$18f_{7/2} \rightarrow 18g_{9/2}$	29.4946(1)								
$18f_{7/2} \rightarrow 19g_{9/2}$	1071.33778(7)	$18g_{9/2} \rightarrow 19h$	1046163.2(3)	$18h \rightarrow 19i$	1042424.5(4)				
$19f_{5/2} \rightarrow 19g_{7/2}$	24.981(1)	$19g_{9/2} \rightarrow 19h$	4320.6(5)						
$19f_{7/2} \rightarrow 19g_{9/2}$	25.1200(8)								
$19f_{7/2} \rightarrow 18g_{9/2}$	-1016.7236(1)								

Table A.2: Tabulated values of the $f \rightarrow g$, $g \rightarrow h$, $h \rightarrow i$, $i \rightarrow k$ and $k \rightarrow l$ transition frequencies measured using an EIT ladder scheme. The fine structure beyond f is not resolved but we label the g states for completeness and for the dipole allowed transitions. Beyond g we omit the fine structure but assume that the $j = \ell + \frac{1}{2}$ is coupled. A negative sign indicates that the final state lies lower in energy than the initial state.

Appendix B

Error from Detuning of Previous Transition(s)

In this appendix, we look at the effect outlined in section 5.2.3 that gives rise to measurement error in our methods described in section 5.2 to measure the various high ℓ intervals. This is used to justify the errors we see in table 5.2. As mentioned previously, the errors arising from the detuning of earlier transitions, i.e. transitions preceding the measurement within the ladder of applied fields, were minimised by first determining the resonance frequency of all earlier transitions. Here, we quantify the residual error that remains in this procedure.

We estimate this uncertainty by assuming that any statistical uncertainty in a preceding transition corresponds to an equivalent small detuning from resonance. Such a detuning produces an asymmetry in the observed lineshape, which in turn shifts the rf frequency at which the two peak amplitudes (or the distances about the central peak) appear equal. To determine the size of this effect, we measured

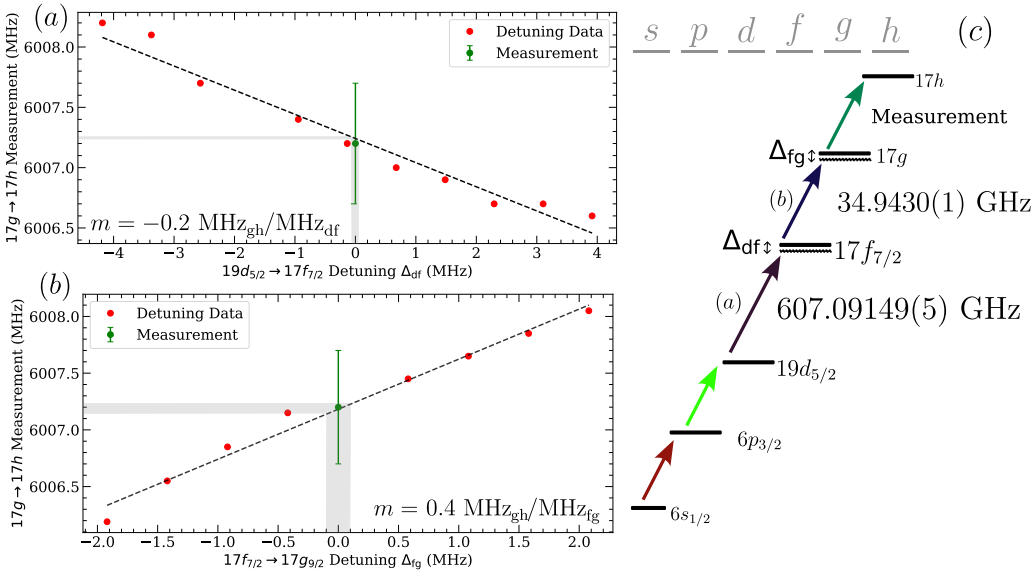

Figure B.1: Diagram showing the effect of detuning previous resonant rf fields on an example measurement. Here, the $17g \rightarrow 17h$ transition by detuning the previous $19d_{5/2} \rightarrow 17f_{7/2}$ and $17f_{7/2} \rightarrow 17g$ transitions. The red data points are 'measurements' of the transition when the previous fields are detuned, shown along with the true measurement (green) with only its error from the statistics of the fit described in section 5.2. (**a**): Plot showing how the detuning of the $19d_{5/2} \rightarrow 17f_{7/2}$ resonant field affects the resulting measurement of the $17g \rightarrow 17h$ transition. The gradient, m, represents the change in the measured frequency, MHz$_{gh}$, per detuning of the $19d_{5/2} \rightarrow 17f_{7/2}$ field, MHz$_{df}$. The grey bands highlight the uncertainty in the measured $19d_{5/2} \rightarrow 17f_{7/2}$ (0.05 MHz) and the resulting uncertainty that propagates as a result. (**b**): Plot showing how the detuning of the $17f_{7/2} \rightarrow 17g$ resonant field affects the resulting measurement of the $17g \rightarrow 17h$ transition. The grey region highlights the uncertainty in the measured $17f_{7/2} \rightarrow 17g$ (0.1 MHz) and the resulting uncertainty that propagates as a result. (**c**) Energy level diagram to clarify the scenario of resonant and detuning fields that affect the resultant measurement.

the resonant frequency of the $17g \rightarrow 17h$ transition while independently detuning the two immediately preceding fields from resonance. These results are shown in Fig. B.1.

By plotting the measured frequency shift against the magnitude of the applied detuning, we extract a gradient, m, representing the induced measurement error per MHz of detuning. For example, for the $19d_{5/2} \rightarrow 17f_{7/2}$, transition we obtain $m = -0.2\,\text{MHz}_{gh}/\text{MHz}_{df}$. This means that (over the tested detuning range) the measurement of the $17g \rightarrow 17h$ interval shifts by -0.2 MHz for every 1 MHz by which

that earlier field is detuned. Since the statistical uncertainty of the $19d_{5/2} \rightarrow 17f_{7/2}$ transition is 0.05 MHz, this corresponds, at the 1σ level, to an effective detuning of 0.05 MHz, yielding a detuning-induced error $\sigma_d = 0.01$ MHz (10 kHz). For the $17f_{7/2} \rightarrow 17g_{9/2}$ transition we find a similar contribution of 0.04 MHz.

We then assume that the detuning errors from all earlier transitions are uncorrelated, so that their contributions can be added in quadrature (appropriate when the underlying error sources are independent [151]). This assumption gives a worst-case estimate, because the sign of the detuning matters. Blue- and red-detuned fields can produce asymmetries in opposing directions, potentially reducing the net effect. We also assume that the strength of this effect, represented by the gradient m, is comparable for the other similar measurements in the excitation chain. Finally, we note that the statistical uncertainties typically increase for our higher-ℓ states, which lead to correspondingly larger detuning errors at later stages.

As an illustrative example, consider the $17k \rightarrow 17l$ measurement. The uncertainty is

$$\sigma_{d_{l\rightarrow m}} \approx \sqrt{\sum_{\ell\rightarrow\ell'} \left(m_{\ell\rightarrow\ell'}\sigma_{s_{\ell\rightarrow\ell'}}\right)^2} \tag{B.1}$$

$$= m\sqrt{(0.05^2 + 0.1^2 + 0.5^2 + 0.4^2 + 1^2)} \tag{B.2}$$

$$= 0.2 \text{ MHz} \tag{B.3}$$

where σ_s denotes the statistical uncertainty in the fitted resonance frequency and here we take each $m_{\ell\rightarrow\ell'}$ to be a constant $m = 0.2$ MHz/MHz. This contribution is smaller than the statistical uncertainty of the transition itself ($\sigma_s = 1$ MHz). When combined in quadrature with the statistical errors, the total uncertainty is unchanged to one significant figure. It is therefore reasonable to neglect detuning-induced errors in the results presented throughout this thesis. Table B.1 is shown for the $n = 17$ high ℓ transitions to illustrate this. The uncertainties only become large in response to large uncertainties associated with statistical uncertainties, which (we argue in section 5.4) can be improved with amplitude stabilisation techniques.

Transition ($n = 17$)	$f_{7/2} \rightarrow g$	$g \rightarrow h$	$h \rightarrow i$	$i \rightarrow k$	$k \rightarrow l$
σ_d (MHz)	0.01	0.022	0.10	0.13	0.24
σ_s (MHz)	0.1	0.5	0.4	1	1

Table B.1: Comparison of statistical uncertainties, σ_s, and those associated with the detuning of previous fields, σ_d, for the $n = 17$ set of high ℓ measurements.

Appendix C

Laser Frequency Noise Method

In this appendix, we provide a detailed derivation of the treatment of laser frequency noise used in the main text (Section 7.2.2.3). While the main discussion focuses on the conceptual dependence of noise on the laser linewidth and related broadening mechanisms, the full stochastic derivation is presented here for completeness. This analysis extends the weak-probe treatment of [250] to arbitrary probe powers, where the weak-probe approximation may no longer hold.

This was studied in the weak probe approximation for theoretical simplicity. However, our results from photon shot noise imply that large probe Rabi frequencies are required to obtain good sensitivities. In these regimes, the weak probe approximation may no longer hold. To improve accuracy, we extend the results of [250] for arbitrary probe powers. The laser frequency is modelled as a stochastic (Wiener) process with the laser linewidth, $\gamma_{\mathrm{p,c}}$, dictating the amplitude of the frequency fluctuations. In order to derive the effect that a laser frequency fluctuation has on a measurement of the electric field, the evolution of the density matrix is derived in the

case of a *stochastic average*. Recall that the master equation for a quantum system can be reduced to a series of linear coupled equations as in section 2.3.5. Taking the stochastic average involves transforming the Hamiltonian, $\mathcal{H}$, by adding laser decoherence to the relaxation rates of atomic coherence. The resulting expression, in the steady-state,

$$\frac{\mathrm{d}\langle \boldsymbol{\varrho} \rangle}{\mathrm{d}t} = \mathcal{H}'\langle \boldsymbol{\varrho} \rangle + \boldsymbol{C} = 0 \tag{C.1}$$

where $\langle \boldsymbol{\varrho} \rangle$ represents the stochastic average state vector of atomic coherences of the quantum system defined by, $\mathcal{H}'$, the modified Hamiltonian of the system after incorporating the frequency fluctuations of the probe and coupling laser. Specifically $\mathcal{H}'$ takes the form

$$\boldsymbol{\mathcal{H}'} = \boldsymbol{\mathcal{H}} + \frac{\gamma_\mathrm{p}}{2}\boldsymbol{B}_\mathrm{p} + \frac{\gamma_\mathrm{c}}{2}\boldsymbol{B}_\mathrm{c} \tag{C.2}$$

where $\boldsymbol{B_i}$ are matrices which modify the respective laser detuning components, Δ_i, of $\boldsymbol{\mathcal{H}}$. The matrices $\boldsymbol{B_i}$ only consist of -1 or 1 and can be determined by allowing $\Delta_i \to \Delta_i + \delta\omega_i$ in the Hamiltonian, and identifying them by inspection of equation (C.1). Following this treatment, one can derive the autocorrelation function of the process and, by the Wiener-Khinchin theorem [270], it can be shown that the PSD matrix for the process is given by,

$$\boldsymbol{S}(\omega) = \frac{1}{2\pi}[\boldsymbol{P}(\infty)(-\boldsymbol{\mathcal{H}'} - i\omega\boldsymbol{I})^{-T} + (\boldsymbol{P}(\infty)(-\boldsymbol{\mathcal{H}'} + i\omega\boldsymbol{I})^{-1}\boldsymbol{P}(\infty)] \tag{C.3}$$

where $\boldsymbol{S}(\omega)$ represents the cross-power spectral density matrix of all the atomic coherences in the system, the diagonal components of which are the PSDs of each atomic coherence, ρ_{ij}. The quantity $\boldsymbol{P}(\infty)$ denotes the covariance in the steady-state, $\boldsymbol{I}$ is the identity matrix and $\boldsymbol{A}^{-T}$ denotes the inverse transpose of the matrix $\boldsymbol{A}$. We consider only the component corresponding to $\mathrm{Im}(\rho_{01})$ as this determines the transmission of the probe laser and any resulting noise. Finally, $\boldsymbol{P}(\infty)$ obeys the equation

$$\boldsymbol{\mathcal{H}'}\boldsymbol{P}(\infty) + \boldsymbol{P}(\infty)\boldsymbol{\mathcal{H}'} + \sum_i \gamma_i \boldsymbol{B_i}(\boldsymbol{P}(\infty) + \boldsymbol{\varrho}\boldsymbol{\varrho}^T)\boldsymbol{B_i}^T = 0. \tag{C.4}$$

The equation for $\boldsymbol{P}(\infty)$ is a non-standard matrix equation that does not fall into common solvable forms such as Sylvester or Lyapunov equations [271]. As such,

there is no closed-form analytical solution in general. In this work, $\boldsymbol{P}(\infty)$ is determined numerically by minimising the Frobenius norm of the residual,

$$\min_{\boldsymbol{P}(\infty)} \|\boldsymbol{\mathcal{H}}'\boldsymbol{P}(\boldsymbol{\infty}) + \boldsymbol{P}(\boldsymbol{\infty})\boldsymbol{\mathcal{H}}'^{\mathrm{T}} + \gamma_{\mathrm{p}}\boldsymbol{B}_{\mathrm{p}}\left(\boldsymbol{P}(\boldsymbol{\infty}) + \boldsymbol{\varrho}\boldsymbol{\varrho}^{\mathrm{T}}\right)\boldsymbol{B}_{\mathrm{p}}^{\mathrm{T}}\|_{\mathrm{F}}^{2} \tag{C.5}$$

using an optimisation routine from the the python package `scipy` and its function *minimize*. This approach is computationally expensive due to the large number of free parameters in $\boldsymbol{P}(\infty)$ and the need for repeated evaluations. Moreover, the optimisation procedure does not, in general, find an exact solution (residual exactly zero), but rather yields an approximate $\boldsymbol{P}(\infty)$ that minimises the residual to within a small tolerance. In the context of the present work, this approximate solution is sufficient, and may only cause slight inaccuracies in the evaluation of the laser frequency noise. Reference [250] does not provide details on the method used to solve this equation. However, given the complexity of the matrix, even in the weak probe regime, it is unlikely that an exact solution exists, and a numerical approximation similar to the one employed here is presumably used.

Equation (C.3) must be evaluated for each velocity group in the atomic vapour, meaning a Doppler average is taken where each detuning, Δ_i, is modified as a result of the atomic motion. An integral similar to (x) can be identified, which leads to [250]

$$\mathrm{NEF}_{\mathrm{FN}} = \frac{\hbar}{\mu}\left(\frac{\mathrm{d}\rho_{01}}{\mathrm{d}\Omega_{\mathrm{LO}}}\right)^{-1}\sqrt{4\pi S_{\rho_{01}}^{D}(0)} \tag{C.6}$$

where $\left(\frac{\mathrm{d}\rho_{01}}{\mathrm{d}\Omega_{\mathrm{LO}}}\right)^{-1}$ is a slope factor telling us about the change in atomic coherence (on the probe transition) due to a change in the microwave (measured) field and $S_{\rho_{01}}^{D}(0)$ is the Doppler averaged noise PSD at zero frequency of the atomic coherence (ρ_{01}) calculated from a stochastic analysis of the Lindbladian governing the quantum system.

The resulting expressions connect the stochastic model of laser frequency fluctuations with the noise-equivalent field sensitivity discussed in Section 7.2.2.3, and form the quantitative basis for the simplified expressions presented there.